A measurement of the quark spin distributions of the nucleon at HERMES.

Thesis submitted in accordance with the requirements of the University of Liverpool for the degree of Doctor of Philosophy

by

Hugh Arthur McLaren Tallini

January 1998

Oliver Lodge Laboratory
University of Liverpool

A measurement of the quark spin distributions of the nucleon at HERMES.

Hugh Arthur McLaren Tallini

Abstract

The HERMES experiment investigates the spin structure of the nucleon by studying the deep inelastic scattering process of the longitudinally polarised positron storage beam at HERA off polarised gas targets. The semi-inclusive hadron and identified pion spin asymmetries have been extracted from data for a ^{3}He target and a proton target. The data cover a kinematic range of $0.023 < x < 0.6$ and $1 < Q^2 < 15$ GeV^2. These results have been combined with the inclusive positron spin asymmetries for both targets in order to extract the polarised u, d and $\overline{q}$ quark distributions. In this extraction, a Monte Carlo was used to unfold the fragmentation process. The fragmentation model of this Monte Carlo was first optimised to simulate HERMES data.

This first analysis gives results that are consistent with existing world data which were taken using a different experimental technique and over a higher energy kinematic region. With only the first two years of HERMES data analysed, the uncertainties in the Δu measurement are comparable to that of the world data.

For my father.

Contents

1 Introduction **8**

2 Theory **11**

2.1 Unpolarised Deep Inelastic Scattering 11

2.2 Polarised DIS – Inclusive measurements 13

2.2.1 Sum Rules 14

2.2.2 Overview of Results 15

2.3 Polarised DIS – The Semi-Inclusive Channel 16

2.3.1 Fragmentation Functions 17

2.3.2 Spin Asymmetries 19

2.3.3 Methods of Extracting the Polarised Quark Distributions . 19

2.3.4 Other Experimental Results 20

2.3.5 Polarised Parton Distribution Parameterisations 20

3 The HERMES Experiment **23**

3.1 The HERA accelerator 24

3.1.1 The Beam Polarimeter 25

3.2 The Targets 25

3.2.1 The Target Cells 25

3.2.2 The Polarised Sources and Polarimeters 30

3.3 The Spectrometer 34

3.3.1 The Spectrometer Magnet 34

3.3.2 The Tracking Chambers 35

3.3.3 The Particle Identification Detectors 38

3.3.4 The Luminosity Monitor 41

3.3.5 The Gain Monitoring System (GMS) 41

3.4 The Data Acquisition 42

3.4.1 The Trigger 42

3.4.2 The Data Acquisition System (DAQ) 42

3.4.3 The Reconstruction Program 43

4 Monte Carlo Simulation Studies **44**

4.1 The Simulation Program 44

4.1.1 The Monte Carlo Event Generator 44

4.1.2 Configuration of Event Generator 46

4.2 Simulation of the Fragmentation Process 47

4.2.1 The String Fragmentation Model 47

4.2.2 Fitting the Fragmentation Parameters 49

4.3 Simulation of Asymmetries 53

4.3.1 Results of Asymmetry Simulations 56

4.3.2 Conclusions from simulation studies 63

5 Event Selection **64**

5.1 Data quality burst level selection 64

5.2 Charge multiplicity study 67

5.3 Particle Identification 69

5.4 Track selection 70

5.5 Differences for 1996 data 73

5.5.1 Data Quality 73

5.5.2 Particle Identification 74

5.5.3 Track Selection 75

5.6 Background Corrections 75

6 Extraction of the Spin Asymmetries **77**

6.1 Calculation of the Asymmetries 77

6.2 Particle Yields 78

6.2.1 1995 (^{3}He target) data 78

6.2.2 1996 (p target) data 78

6.3 Asymmetry results 79

6.3.1 1995 (^{3}He target) data 79

6.3.2 1996 (p target) data 83

7 Systematic Uncertainties on the Extraction of the Asymmetries **87**

7.1 Comparison of the Inclusive and Semi-Inclusive Asymmetries . . . 87

7.2 Hadron kinematic cuts . . . 87

7.3 Summing versus Averaging . . . 88

7.4 Stability over time . . . 91

7.5 False Asymmetries . . . 92

8 Extraction of the Polarised Quark Distributions **94**

8.1 The Charge Difference Pion Extraction . . . 94

8.1.1 Description of the Method . . . 94

8.1.2 Results . . . 95

8.1.3 Conclusions . . . 97

8.2 The Monte Carlo Fit Method of Extraction . . . 97

8.2.1 Description of the Method . . . 97

8.2.2 Configuration of the MC . . . 98

8.2.3 Fit Results . . . 100

8.2.4 Statistical Error Evaluation . . . 100

8.3 Comparison of Extraction Methods . . . 103

8.4 Systematic Error Evaluation . . . 105

8.4.1 Uncertainty in the Measurement of the Asymmetries . . . 105

8.4.2 Uncertainty in the MC Fitting Procedure . . . 107

8.4.3 The Final Result . . . 110

9 Conclusions **115**

A Error Analysis for the Asymmetries **117**

A.1 Charge Difference Asymmetry 117

A.2 Single Particle Asymmetries 118

B χ^2 ellipsoid fitting **119**

Acknowledgments

I am grateful to the University of Liverpool for providing me with the funding to carry out this PhD, and particularly Prof. Erwin Gabathuler for organising this funding. I would like to thank my supervisor, Dr. Geoff Court, for his continuous enthusiasm and for guiding me through what has been an interesting and varied PhD. Thanks also to Jim Stewart for his constant support since I began this project.

This thesis owes a great debt to Holger Ihssen with whom I have worked on this analysis. I am grateful for him taking time out to explain things to me and for (usually!) being patient with my stupid questions!

High Energy Physics is very much a team effort, and I thank all the HERMES collaborators, too many to mention individually, for their part in this thesis and for the friendly atmosphere which exists within the collaboration. I would like to thank especially those in the semi-inclusive analysis group, in particular Philipp Geiger, Michael Ruh and Eppo Bruins for useful discussions.

Thanks to the Liverpool Physics Dept. drawing office for the nice pictures of the target in chapter 3.

Thanks to all the people who made my two years in Hamburg fun, particularly the UK contingent, Paul Sutton, Stuart Cocks, Kirstee Hewitt, Jane Bromley, Ben Waugh, Dave Milstead, Lee and Rachel West, Eram Rizvi and Andy Mehta, to name a few. A big thankyou to Susan Ketels who went well beyond her call of duty to help me with the (many) problems I encountered during my stay – no thanks to Herr und Frau 'honest' Offen and Dr. 'meat-cleaver' Klöse for creating most of them!

I would like to thank Mark Smith, Chris Cormack, and Theo Holtom for all the irreverant and distracting office conversations during the dark days of writing up in Liverpool. Thanks also to fellow HERMES-Liverpool student/slave, Mike McAndrew, for the much needed company and sanity in the tin can container 9 at DESY. Thanks to Angela Benelli for her friendship.

A big thankyou to the members of Liverpool Victoria Rowing Club for being so welcoming to me and for helping a stressed out physicist to unwind. Thanks to Dave Muskett who helped me throughout my stay in Liverpool, from showing me the ropes during my first few months in the department to saving me from my various car disasters in the recent past.

Thanks to Molly Anderson for her friendship and love which have been an important part of getting me through this whole experience.

I thank my family for their love and support, particularly my mother for putting up with me. Thanks to my uncle, Armando Reale, for pursuading me at the last minute to switch to a physics course at University – something I have regretted only occasionally!

This thesis is dedicated to my father. Though he died before he got a chance to teach me any phyiscs, I was fascinated as a child by the relics of the weird and wonderful life he had led as a particle physicist – bubble chamber pictures, FORTRAN punch cards and endless airline tickets – and this led me to a curiosity about particle physics itself, which is, I suppose, why this thesis has come about.

Chapter 1

Introduction

The Quark Parton Model (QPM) was devised after the first deep inelastic scattering (DIS) experiments showed the existence of pointlike particles within the nucleon. The QPM associated these pointlike particles with spin-$\frac{1}{2}$ quarks and showed that interactions involving hadrons could be understood as interactions involving the underlying quark substructure. The simple QPM was successful in describing the early DIS data, however as higher and higher energy experiments were able to study the partonic interactions at smaller scales, the QPM had to be modified by perturbative QCD in order to describe the data properly.

The first measurements of the spin structure of the nucleon, carried out at relatively low energy, agreed with the QPM predictions. However the higher energy EMC experiment, which was able to access a more interesting kinematical zone, produced results which contradicted the simple QPM predictions [1]. Their measurements indicated that the proportion of the total spin of the nucleon carried by the quarks is only about a third and the strange sea is significantly negatively polarised. In contrast, the QPM predicted that the valence quarks would carry all of the nucleon spin. Though some of the discrepancies in the understanding of the nucleon spin structure were later resolved with the help of perturbative QCD, many open questions remain. This thesis addresses one of these questions, namely how much of the nucleon spin is carried by each flavour of quark.

Historically, inclusive measurements in polarised deep inelastic scattering have been the dominant source of information on the spin structure of the nucleon. In this process, the leptonic probe scatters off a quark of any flavour in the target nucleon, and the result is sensitive to the contribution to the net spin of the nucleon from all the quark constituents together. In contrast, the approach presented here uses the semi-inclusive channel in polarised DIS. Here a final state hadron in coincidence with the scattered lepton is used to tag the flavour of the struck quark. Using this extra information, it is possible to measure the separate contributions to the nucleon's spin from each quark flavour.

Up to now, the semi-inclusive channel in spin physics has not been well investigated due to the technical challenges of constructing polarised experiments. However, the HERMES experiment, which uses the polarised 27.5 GeV positron beam of the HERA collider at DESY, has been specifically designed to study this channel. As will be described in chapter 3, the high purity gas jet target technology and the excellent particle identification capability enables HERMES to make high precision measurements in both the semi-inclusive and inclusive channels.

The analysis presented here is of semi-inclusive data taken from the first two years of HERMES running, where both proton and neutron targets were used, each target providing complementary information on the nucleon spin structure. The data selection is described in chapter 5, with the resulting asymmetries shown in chapter 6. Systematic studies on the extraction of these asymmetries are presented in chapter 7.

In order to understand the correlation between the final state hadrons and the struck quark flavour, which is vital in order to extract partonic level quantities such as the polarised quark distributions from hadronic level quantities such as final state hadron spin asymmetries, the soft QCD process of fragmentation must be understood. The approach of this analysis is to use phenomelogical models within a Monte Carlo (MC) to unfold the fragmentation process and then to extract the polarised quark distributions from the measured semi-inclusive spin asymmetries. The MC and the adjusting of the fragmentation parameters to suit the HERMES kinematical domain is described in chapter 4.

The author was mainly responsible for the extraction of the hadron asymmetries for a ^{3}He target and carrying out systematic studies on these asymmetries. These results have been combined with the results for a proton target and with inclusive results from both targets in order to provide enough information to make a reasonable measurement of the final quark spin distributions. All the asymmetry results presented in this thesis are consistent with HERMES preliminary results [2]. The author additionally worked on the Monte Carlo used to simulate the semi-inclusive asymmetries, particularly on the fitting of the fragmentation parameters described in chapter 4. The collaboration has not yet finalised the extraction of the polarised quark spin distributions. The preliminary analysis presented here for the extraction of the polarised u,d and $\overline{q}$ quark spin distributions is described in chapter 8 and was carried out by the author.

Additionally the author was involved in the design and construction of the wake field suppressors for the target chamber, described in chapter 3, the testing of the Hydrogen target's superconducting magnet and investigating the target cell's cooling characteristics.

Chapter 2

Theory

2.1 Unpolarised Deep Inelastic Scattering

Lepton nucleon scattering has been the main method of investigating the structure of the nucleon. At very high energies the scattering takes place off the quark constituents of the nucleon in a process called deep inelastic scattering. This process is shown schematically in figure 2.1. Here an electron with four momentum

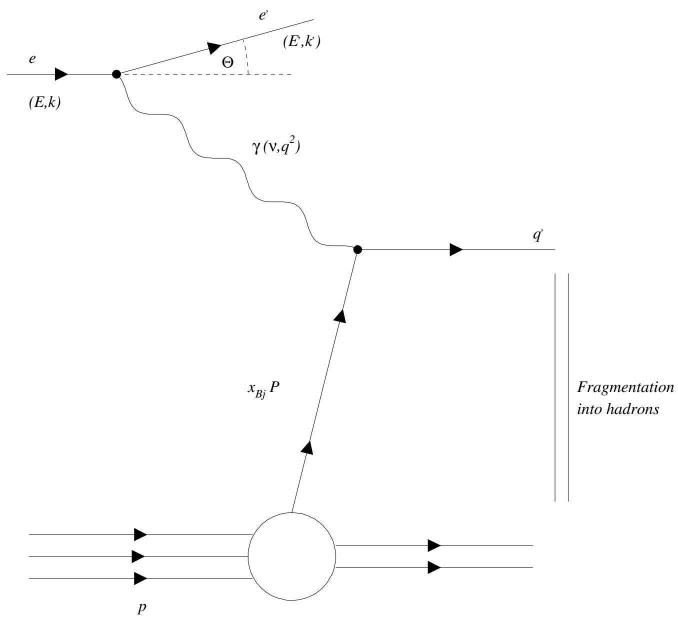

Figure 2.1: Schematic diagram of a deep inelastic scattering event.

k scatters off a target nucleon of momentum P to emerge deflected by an angle θ and with momentum k'. The probe in the interaction is effectively the exchanged virtual photon with momentum q. The standard DIS variables are then defined as

$$Q^2 = -q^2 = (k - k')^2 \tag{2.1}$$
$$x = \frac{Q^2}{2P \cdot q} \tag{2.2}$$
$$y = \frac{P \cdot q}{P \cdot k} \tag{2.3}$$
$$W^2 = (q + p)^2. \tag{2.4}$$

In the laboratory frame, these variables can be written as

$$Q^2 = 4EE' sin^2(\theta/2) \tag{2.5}$$
$$x = Q^2/2M(E - E') = Q^2/2M\nu \tag{2.6}$$
$$y = \nu/E \tag{2.7}$$
$$W^2 = M^2 + 2M\nu - Q^2 \tag{2.8}$$

with M the mass of the nucleon, E the energy of the incident electron and E' the energy of the scattered electron. The resolving power of the virtual photon probe is a function of its wavelength, $\hbar/\sqrt{(Q^2 + \nu^2)}$, and thus the degree of structure which can be resolved increases with increasing Q^2.

The spin averaged cross section for charged lepton scattering can be written in terms of structure functions $F_i(x, Q^2)$ which parameterise the structure of the target as seen by the virtual photon,

$$\frac{d^2\sigma}{dxdy} = \frac{8\pi\alpha^2 ME}{Q^4}\left[\left(\frac{1 + (1-y)^2}{2}\right) 2xF_1 + (1-y)(F_2 - 2xF_1) - (M/2E)xyF_2\right]. \tag{2.9}$$

In the limit of $Q^2, \nu \to \infty$ at fixed x, known as the Bjorken limit, these structure functions were observed to depend only on the variable x, which is dimensionless. The fact that they do not depend on any variable with a length scale (i.e. that they are 'scale invariant'), was the first direct evidence of pointlike particles within the proton [3].

In the Quark Parton Model (QPM) [4], again at the Bjorken limit, x can be associated with the fraction of the proton's momentum carried by the struck quark, and the proton structure function has a simple interpretation as

$$F_2(x) = 2xF_1(x) = \sum_{i=u,d...} e_i^2 q_i(x) \tag{2.10}$$

where for a quark of flavour i, e_i are the quark charges and $q_i(x)$ the quark probability distributions. Quark and gluon interactions amongst themselves cause a Q^2 dependence of the structure functions which is described by perturbative QCD.

2.2 Polarised DIS – Inclusive measurements

In a polarised DIS experiment, both the target and beam are polarised. The spin dependent part of the total DIS cross section is small and to study it the relative direction of the beam and target polarisation is flipped and the relative cross section for each orientation measured. For a longitudinally polarised target and beam, for the inclusive channel, the virtual photon-nucleon asymmetry A_1 is measured,

$$A_1 = \frac{d^2\sigma^-_{\gamma N} - d^2\sigma^+_{\gamma N}}{d^2\sigma^-_{\gamma N} + d^2\sigma^+_{\gamma N}}, \tag{2.11}$$

where the differential cross sections $d^2\sigma^+$ and $d^2\sigma^-$ correspond to the target and beam spins polarised parallel and antiparallel to each other. The denominator is simply twice the spin averaged cross section (equation 2.9). However for the numerator, in a similar method to the treatment of the unpolarised case, two new structure functions are introduced, this time called the spin structure functions g_1 and g_2. These parameterise the spin structure of the target nucleon and can be written

$$\frac{d^2\sigma^-}{dxdy} - \frac{d^2\sigma^+}{dxdy} = \frac{8\pi\alpha^2 ME}{Q^4}\left[\left(2y - y^2 - \frac{Mxy^2}{E}\right)2xg_1(x,Q^2) - \frac{4M}{E}x^2yg_2(x,Q^2)\right]. \tag{2.12}$$

In the kinematic region of current experiments, the contribution from g_2 can be neglected and the structure function g_1 can be derived to be [5]

$$A_1 \approx \frac{g_1}{F_1}, \tag{2.13}$$

and thus can be determined from a measurement of A_1 and F_1, the latter being obtained from unpolarised experiments.

Just like F_1, g_1 has a simple interpretation in the simple Quark Parton Model,

$$g_1(x) = \frac{1}{2}\sum_{i=u,d...} e_i^2(\Delta q_i(x) + \Delta\overline{q}_i(x)), \tag{2.14}$$

with

$$\Delta q_i(x) = q_i^+(x) - q_i^-(x) \tag{2.15}$$

where the polarised quark distributions, $q_i^{+(-)}(x)$, represent the probability of finding a quark of flavour i parallel (antiparallel) to the nucleon's spin. The quark and gluon interactions amongst themselves give g_1 Q^2 dependent terms which are predicted by perturbative QCD [5],

$$g_1(x) = \frac{1}{2}\sum_{i=u,d...} e_i^2(\Delta q_i(x) + \Delta\overline{q}_i(x))(1 - O(\alpha_s)). \tag{2.16}$$

2.2.1 Sum Rules

Sum rules are integrals over x for combinations of parton distributions. They are useful because theoretical models can make predictions for what their values should be. A trivial example is that the sum over all contributing quarks of the proton should give the proton's quantum numbers,

$$\int_0^1 u_v(x)dx = 2\ , \int_0^1 d_v(x)dx = 1. \tag{2.17}$$

Another example is the momentum sum rule for quarks which was important in establishing the evidence for partons other than quarks in the nucleon : it was found experimentally that

$$\int_0^1 x[q(x) + \overline{q}(x)]dx \approx 0.5 \tag{2.18}$$

This shows that quarks carry only half of the proton's momentum, the rest being carried by gluons.

Two important sum rules have been derived for polarised DIS.

The Bjorken Sum Rule

The Bjorken sum rule can be derived assuming only current algebra and SU(2) isospin symmetry [6]. It connects the first moment of g_1, $\Gamma_1 = \int_0^1 g_1(x)dx$, for proton and neutron targets with the weak vector and axial coupling constants g_A and g_V,

$$\Gamma_1^p - \Gamma_1^n = \int_0^1 (g_1^p - g_1^n)dx = \frac{1}{6}\left|\frac{g_A}{g_V}\right|. \tag{2.19}$$

It is a rigorous prediction of QCD at infinite momentum transfer and is subject to QCD radiative corrections at finite values of Q^2 [7, 8].

The Ellis-Jaffe Sum Rule

A sum rule has been derived for a proton or neutron target separately. Making the assumption that the strange quark sea is unpolarised and that SU(3) flavour symmetry holds, the Ellis-Jaffe (E-J) sum rule [9] can be derived for the proton,

$$\Gamma_1^p = \int_0^1 g_1^p dx = \frac{1}{12}\left|\frac{g_A}{g_V}\right|\left[1 + \frac{5}{3}\frac{3F-D}{F+D}\right], \tag{2.20}$$

where F and D are the symmetric and asymmetric weak SU(3) flavour couplings of the baryon octet, measured, for example, from the decays the decays $n \to p$ or $\Sigma^- \to n$.

2.2.2 Overview of Results

The first spin experiments, conducted at SLAC by the E-80 [10] and E-130 [11] collaborations using proton targets confirmed the E-J sum rule for the proton and the naive QPM view that the spin of the nucleon is carried by the valence quarks. However their measurements were confined to relatively high x values ($\gtrsim$0.1), and low Q^2 values. It was not until the EMC experiment, which probed the sea quarks in the low x region for the first time, that this naive view was contradicted.

EMC [1] discovered that the E-J sum rule is not valid. These findings were confirmed by the later experimental programs at SLAC [13, 14] and CERN [12]. These experiments also found that the Bjorken sum rule is valid. The most plausible explanation for this is that the main assumption made in the E-J sum rule, that the strange sea quarks are unpolarised, is wrong. In fact, by taking the first moments of g_1 from the data on proton and neutron targets, combining it with neutron-β decay results and applying perturbative QCD corrections, it has been found that for the proton [15]

$$\Delta u = +0.83 \pm 0.03\,,\ \Delta d = -0.43 \pm 0.03\,,\ \Delta s = -0.10 \pm 0.03, \tag{2.21}$$

at a renormalisation scale of Q^2=10 GeV^2. This means that the total spin of the proton carried by the quarks, $\Delta\Sigma$, is only 0.31 ± 0.07. This can be compared with the QPM expectation of [16]

$$\Delta u = \frac{4}{3}\,,\ \Delta d = -\frac{1}{3}\,,\ \Delta s = 0\,,\ \Delta\Sigma = 1. \tag{2.22}$$

It should be noted that alternative scenarios for making up the difference between the predicted and measured values of the E-J sum rule have been put forward. For example that the SU(3) flavour symmetry is broken and $\Delta s = 0$ [17, 18] or that Δs is zero and the gluons make up the deficit in the sum rule [19].

To summarise, from conservation of angular momentum, all the possible contributions to the nucleon's spin are

$$\frac{1}{2} = \frac{1}{2}(\Delta u + \Delta\overline{u} + \Delta d + \Delta\overline{d} + \Delta s + \Delta\overline{s}) + \Delta g + < L_z >, \tag{2.23}$$

where $< L_z >$ is the orbital angular momentum of the nucleon and Δg is the contribution to the spin from the gluons. The inclusive measurement of g_1 is only sensitive to the charge weighted sum of all quark flavours and not to the individual quark distributions. The evaluation of equation 2.21 relies heavily on the theoretical assumption of an SU(3) flavour symmetric sea and of SU(3) flavour symmetry for the weak decays of the baryon octet. In general, inclusive measurements for proton and neutron targets are only able to constrain the polarised valence quark distributions (see section 2.3.5). The sea quark and gluon distributions are largely unbounded. The semi-inclusive channel, however, can measure Δu, Δd and $\Delta\overline{q}$ in a more direct manner, without the necessity for the same theoretical assumptions as used for analysis of the inclusive channel.

2.3 Polarised DIS – The Semi-Inclusive Channel

Figure 2.2 shows the schematic diagram for the semi-inclusive production of hadron h in the process

$$l + N \rightarrow l' + h + X,$$

where N is the target nucleon, l the leptonic probe and X any remaining undetected states. A quark is knocked out of the target nucleon and then both target and struck quark fragment. The leading hadrons (also called current region fragments) are most likely to be correlated with the struck quark, whereas the target fragmentation region contains the fragments from the target which are not correlated with the struck quark.

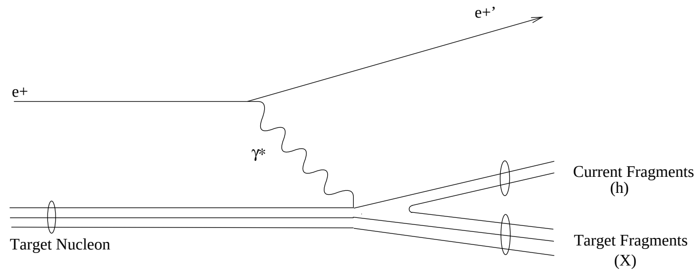

Figure 2.2: Schematic diagram of a semi-inclusive DIS event. The struck quark fragments to the 'current region', while the target remnants fragment to the 'target region'.

2.3.1 Fragmentation Functions

The assumption is made that the quark scattering process is independent of the fragmentation process. There is much experimental evidence to support this hypothesis, for example the equivalence of the hadron production cross sections in e^+e^- annihilation [20] and μp scattering [21].

In much the same way that the quark distributions in the nucleon are parameterised by the probability distribution functions, $q_i(x)$, the fragmentation process is parameterised by fragmentation functions, $D_i^h(z)$, which represent the probability of a struck quark of flavour i forming a hadron of type h. In both cases, these parameterisations are necessary because the behaviour of partons at large distances cannot be calculated using perturbative QCD. These parameterisations can be compared to experimental data.

The fragmentation functions are functions of $z = E_h/\nu$, where E_h is the hadron energy and satisfy

$$\sum_h \int_0^1 z D_i^h(z) dz = 1 \tag{2.24}$$

due to momentum conservation and are normalised by

$$\sum_i \int_0^1 D_i^h(z) dz = n_h \tag{2.25}$$

where n_h is the hadron multiplicity.

As i runs over all quark flavours, and h over each hadron type, there are a large number of possible fragmentation functions. However, assuming charge and isospin conservation, it is possible to reduce the number of fragmentation functions to three : a favoured fragmentation function, where the hadron contains the same flavour as the struck quark,

$$D^+(z) = D_u^{\pi^+}(z) = D_d^{\pi^-}(z) = D_{\bar{d}}^{\pi^+}(z) = D_{\bar{u}}^{\pi^-}(z), \quad (2.26)$$

an unfavoured fragmentation function, where the hadron does not contain the same flavour as the struck quark,

$$D^-(z) = D_d^{\pi^+}(z) = D_u^{\pi^-}(z) = D_{\bar{u}}^{\pi^+}(z) = D_{\bar{d}}^{\pi^-}(z), \quad (2.27)$$

and a strange fragmentation function,

$$D^s(z) = D_s^{\pi^+}(z) = D_s^{\pi^-}(z) = D_{\bar{s}}^{\pi^+}(z) = D_{\bar{s}}^{\pi^-}(z). \quad (2.28)$$

The favoured and unfavoured fragmentation functions were first measured by EMC[22] and their results are shown in figure 2.3. They found that they could parameterise the ratio of the favoured to unfavoured fragmentation factors, η, with $\eta = (1+z)/(1-z)$. As can be seen, at low z the favoured and unfavoured functions become indistinguishable, corresponding to the fact that at low z the current region fragments are contaminated with target region fragments which are not correlated with the flavour of the struck quark.

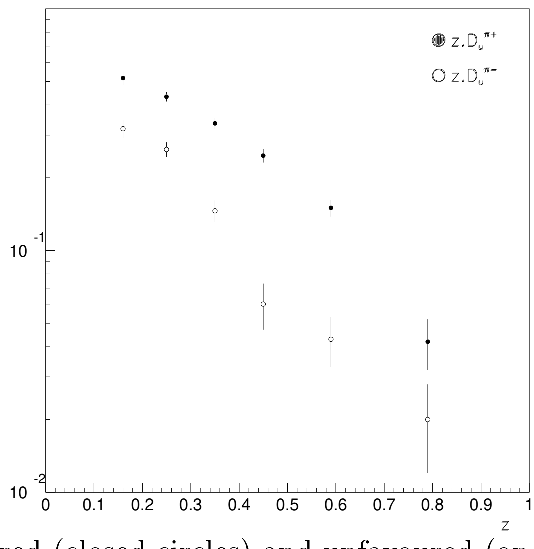

Figure 2.3: The favoured (closed circles) and unfavoured (open circles) fragmentation functions measured by EMC.

2.3.2 Spin Asymmetries

The raw semi-inclusive spin asymmetry for a hadron h and target N is defined to be

$$A_N^h \equiv \frac{\Delta\sigma_N^h}{\sigma_N^h} \tag{2.29}$$

where $\Delta\sigma_N^h = \sigma_{N-}^h - \sigma_{N+}^h$ and $\sigma_N^h = \sigma_{N-}^h + \sigma_{N+}^h$, with $+(-)$ representing the target spin aligned parallel (antiparallel) to the beam.

The cross section for the production of a particular hadron h can be written

$$\frac{d\sigma^h(z)}{dz} = \frac{\sum_i e_i^2 q_i(x) D_i^h(z)}{\sum_i e^2 q_i(x)} \sigma^T(x), \tag{2.30}$$

where σ^T is the total inclusive cross section.

Using this, the asymmetry for a hadron h can be written as

$$A_N^h = \frac{\sum e_i^2 \Delta q_i(x) D_i^h(z)}{\sum e_i^2 q_i(x) D_i^h(z)}. \tag{2.31}$$

2.3.3 Methods of Extracting the Polarised Quark Distributions

By taking the special case of the charge difference pion asymmetry ($h = \pi^+ - \pi^-$), assuming isospin conservation and that the fragmentation functions can be written in terms of favoured and unfavoured functions (equations 2.26 - 2.28), in the asymmetry the contribution from the sea cancels as do the fragmentation functions, and a simple expression remains [23],

$$A_p^{\pi^+-\pi^-}(x) = \frac{4\Delta u_v(x) - \Delta d_v(x)}{4u_v(x) - d_v(x)}, \tag{2.32}$$

where $u_v(x)$ and $d_v(x)$ are the unpolarised valence quark distributions which have been measured in unpolarised experiments. A similar expression can be written down for a neutron target, and using data from two targets the equations can be solved to give the two unknowns, the polarised valence quark distributions.

As will be shown in chapter 4, a correction is required to account for the fragmentation process, particularly the contamination from the target fragmentation region. This correction can only be done using Monte Carlo. In addition, the disadvantage of this method is that the difference of two count rates is required, which amplifies the statistical uncertainty of the final result compared to using single hadron asymmetries. The method also has no sensitivity to the sea quark polarisation.

An alternative method is presented in chapter 8 which uses the single hadron asymmetries in conjunction with the inclusive positron asymmetries to extract the polarised quark distributions, including the sea quark distribution. This method relies on a Monte Carlo for the extraction, particularly for the simulation of the fragmentation process.

Both extraction methods are described in more detail in chapter 8.

2.3.4 Other Experimental Results

EMC was the first experiment to measure hadron spin asymmetries, however their yields were not high enough to extract any useful information on the polarised quark distributions [1]. SMC had better yields and have published the first polarised quark distributions measured from their charged hadron asymmetries [24]. As SMC and EMC operated in the same kinematic region, SMC were able to make use of the EMC fragmentation function measurements in their analysis. In addition, they used their inclusive measurements as well as their charged hadron asymmetries for proton and deuterium targets to extract the polarised u and d valence and non-strange sea quark distributions. Their results, which are extracted from the entire SMC data set, are shown in figure 2.4.

In addition they calculated the integrals of the distributions to be $\Delta u = 0.77 \pm 0.10 \pm 0.08$, $\Delta d = -0.52 \pm 0.14 \pm 0.09$ and $\Delta \overline{q} = 0.01 \pm 0.04 \pm 0.03$, which are consistent with results from the inclusive measurements mentioned above.

2.3.5 Polarised Parton Distribution Parameterisations

Several parameterisations of the polarised parton distributions exist. The parameterisations are important to compare the data with and also are necessary as inputs for the Monte Carlo to run simulations of the asymmetries.

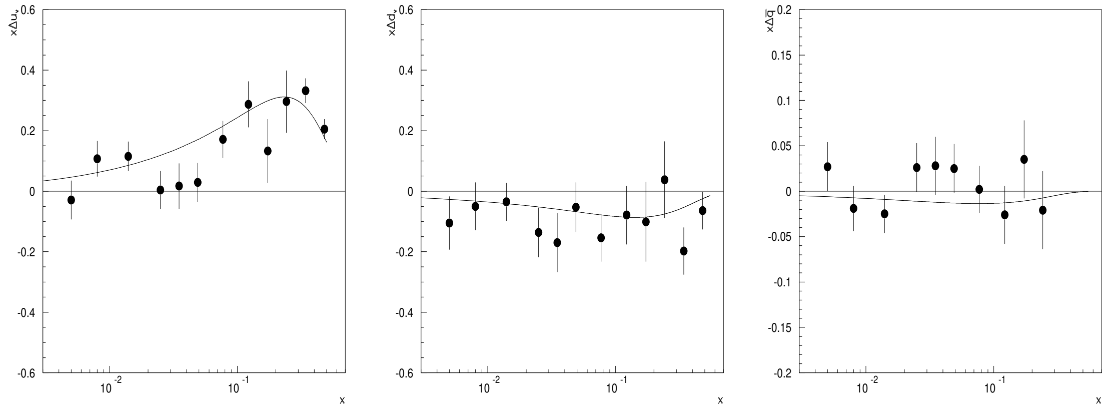

(a) **(b)** **(c)**

Figure 2.4: The (a) Δu_v , (b) Δd_v and (c) $\Delta\overline{q}$ distributions measured by SMC. The line drawn corresponds to the Glück, Reya and Vogelsang parameterisation, described in section 2.3.5, evaluated at a Q^2 of 10 GeV^2.

The Glück, Reya, Vogelsang Parameterisation

This parameterisation was chosen because it uses the most up to date set of world data. In addition it is calculated at leading order in QCD, which matches the leading order Monte Carlo which is used in the analysis (see chapter 4).

As already mentioned, the inclusive measurement of g_1 is only sensitive to the weighted charge squared of the individual quark distributions. However phenomological fits to the data have been made to extract the separate polarised quark distributions. In the parameterisation of Glück, Reya and Vogelsang [18] [1], the separate u and d valence, the light and strange sea quark and gluon polarised distributions have been determined by making a leading order QCD fit to all the published world data on A_1^N. They constrain their fit with the positivity limit

$$|\Delta f(x, Q^2)| \leq f(x, Q^2) \tag{2.33}$$

and the sum rules (described in section 2.2.1),

$$\Delta u + \Delta\overline{u} - \Delta d - \Delta\overline{d} = g_A = F + D \tag{2.34}$$

$$\Delta u + \Delta\overline{u} + \Delta d + \Delta\overline{d} - 2(\Delta s + \Delta\overline{s}) = 3F - D. \tag{2.35}$$

[1] This parameterisation is referred to in the rest of this thesis as 'GRVOG', to distinguish it from the well known unpolarised parameterisation of Glück, Reya and Vögt which is commonly referred to as 'GRV'.

The main assumptions are that SU(3) flavour symmetry holds between hyperon decay and the matrix elements of the flavour changing charged weak axial currents and the neutral ones relevant for the polarised parton distributions (the so called 'standard' scenario) and thus $\Delta\overline{u} = \Delta\overline{d} = \Delta\overline{s} = \Delta s \equiv \overline{q}$.

While the valence quark distributions are well constrained, the sea quark and gluon distributions are not. These distributions are shown in figure 2.4.

Chapter 3

The HERMES Experiment

HERMES is designed to make precise polarised measurements of both the inclusive and semi-inclusive channels in DIS. To enable the semi-inclusive channel to be measured, a wide angled spectrometer is used. In addition, particle identification detectors provide separation of the DIS positrons from the hadron background and include a threshold Čerenkov detector to provide hadron identification.

The measured spin asymmetry for a particular particle can be expressed as,

$$A_1 = \frac{N_- - N_+}{N_- + N_+} \frac{1}{P_B P_T f D}, \tag{3.1}$$

and, provided the asymmetry is small, it follows that the statistical uncertainty is given by

$$\delta A_1 = \frac{1}{(N_- + N_+)^{\frac{1}{2}}} \frac{1}{P_B P_T f D}. \tag{3.2}$$

Here N_+ and N_- are the count rates for the particle in each spin state, P_B is the beam polarisation, P_T the target polarisation, f the fraction of events originating from polarisable nucleons in the target and D is the photon depolarisation factor (discussed in section 4.3). It can be seen therefore that in order to minimise the statistical uncertainty, high particle yields and high target and beam polarisations are required. To achieve this, HERMES uses the high intensity, polarised HERA storage ring in conjunction with high purity ($f = 1$), polarised gas targets.

3.1 The HERA accelerator

The 27.5 GeV electron storage ring and 820 GeV proton storage ring of the HERA accelerator is used simultaneously by four experiments. H1 and Zeus operate as collider experiments in the North and South Halls, while HERA-B and HERMES operate as fixed target experiments, HERA-B using the proton beam in the West Hall and HERMES using the electron beam in the East Hall (see figure 3.1). Either electrons or positrons can be accelerated with no effect on the HERMES physics program. Since data taking began, a positron beam has been used. 210 bunches each containing about 4×10^{10} particles are accelerated with spacings of 96 ns between bunches.

The positron beam is transversely polarised by the Sokolov-Ternov effect [25] and using spin rotators, this transverse polarisation is changed to longitudinal polarisation in front of the HERMES experiment and changed back again after it. HERA is one of the highest energy storage machines to achieve polarised positron beams [26].

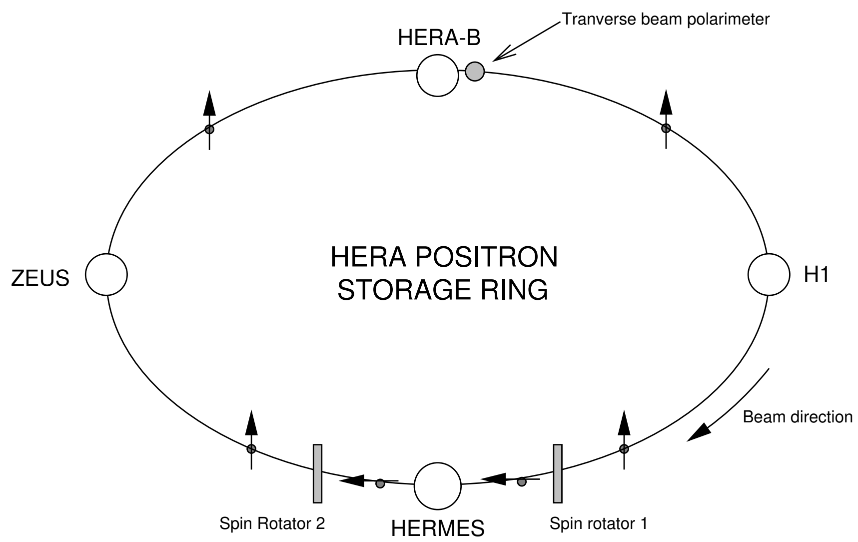

Figure 3.1: The layout of the HERA accelerator, showing the polarisation of the positrons.

3.1.1 The Beam Polarimeter

The transverse polarisation of the beam is measured in the West Hall. The spin dependence of the Compton scattering cross section is made use of to determine the beam polarisation by scattering left and right circularly polarised laser light off the positron beam. By measuring the up-down asymmetries of the backscattered photons in a position sensitive calorimeter, the beam's transverse polarisation can be ascertained [27, 28]. The average beam polarisation for the 1995 data set was 55% and for 1996 52%.

3.2 The Targets

A polarised gas storage cell target inside the positron storage ring is used. The advantage of using a gas target is that it is clean. The pure gas species can be polarised to a relatively high degree and is free from dilutions due to extraneous material in the target. In addition fast polarisation state changes can be achieved, reducing the systematic uncertainty of the asymmetry measurements. Two different targets have been used so far, a ^{3}He target was used in 1995 and an atomic hydrogen target in 1996/7. Each target uses different sources and polarimetry, though the storage cells are similar for both. As well as injecting polarised gas into the target cell, both targets are additionally able to run with unpolarised gases, for unpolarised physics studies.

3.2.1 The Target Cells

Given that the current polarised gas sources available produce a relatively low flux of polarised atoms, a storage cell technique is used to increase the target density. The target gas from the polarised source is injected through a side tube into an open ended storage cell, elliptically shaped in cross section, through which the beam passes. The storage cell confines the target atoms near to the beam axis, thus increasing the target density. After diffusing through the 400 mm long cell, the atoms are pumped away by a powerful differential vacuum pump system, in order to maintain the ultra high vacuum conditions in the beam pipe which is critical for attaining a good positron beam life time.

The target density is inversely proportional to the square root of the temperature, and thus by cooling the cell additional gains are made in target density. Both the ^{3}He and hydrogen target cells are made of thin-walled, high purity aluminium, in order to minimise multiple scattering of particles from it, and supported by cooling rails through which cold helium gas flows to cool the cell to its operating temperature. Using this storage cell technique increases the target density by two orders of magnitude compared to using a free gas jet [29].

The target chamber, within which the storage cell and support rails are mounted (see figure 3.2), is inserted into the beam line. The target cell and detectors are protected from synchrotron radiation by a system of two collimators, C2 mounted at the upstream end of the target chamber and C1 2 m upstream. At the downstream end, a 0.3 mm stainless steel window encloses the target chamber. The downstream beam pipe is connected to the centre of this target window. Figure 3.3 shows the position of these components and of the vacuum pump system.

A quantisation axis for the nuclear polarisation is provided by a static magnetic field. This field is longitudinal to the beam axis and so does not interfere with the beam itself.

Wake field suppressors

In the design of the target cells, care was taken to have no abrupt changes in the cross section of the beam enclosure which might induce "wake fields" [30]. These are electromagnetic fields which are excited in any cavity like structure by the passing beam which, due to its bunch structure, generates electromagnetic rf fields. Within the target chamber, there are two gaps which need to be bridged to short circuit the rf cavities which would otherwise exist. These gaps are between the upstream end of the cell and the collimator C2, and the downstream end of the cell and the downstream beam pipe (see figure 3.2).

Wake fields in the target chamber would result in beam energy loss which could cause beam instabilities or even beam loss. Additionally they would generate heat within the target chamber which is particularly undesirable as the cell is required to be at a uniform low temperature. The requirement for the two "wake field suppressors" which bridge these two gaps is for a connection that would

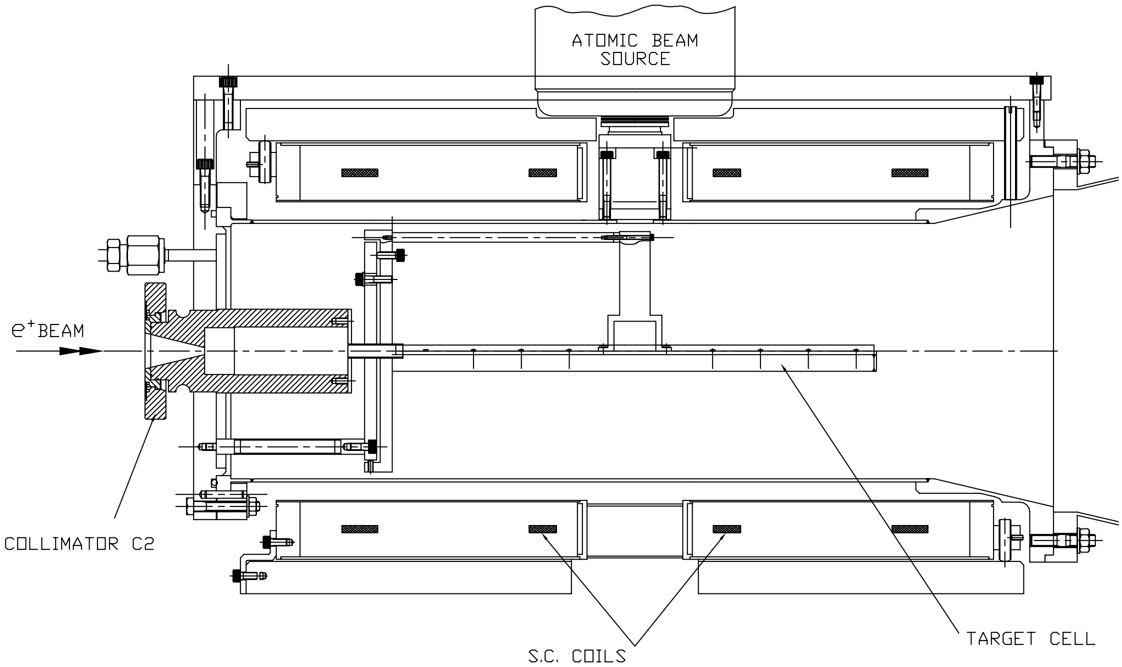

Figure 3.2: Side view of the Hydrogen target chamber. The target cell support rails can be seen mounted onto a support flange which also holds the C2 collimator. The superconducting coils of the holding magnet are enclosed by the target chamber.

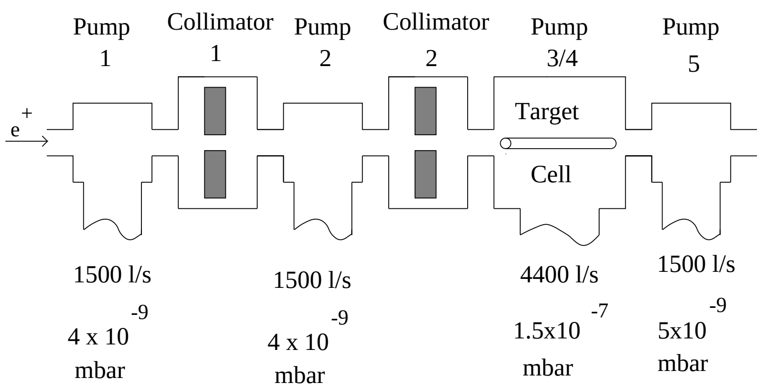

Figure 3.3: Schematic diagram of the beam line in the target area. For each vacuum pump, the pumping speed and operating vacuum pressure is shown.

give good electrical contact, but low effective thermal contact between the cell ends and the collimator or beam pipe. The bad thermal contact is particularly important for the upstream wake field suppressor where the gap is only 35 mm, and the temperature difference between the cell and the collimator can be as much as 300 K.

The solution found was to use eight $0.25 \times 2.5 \times 40$ mm^3 phosphor bronze fingers which make contact with the cell just as pressed contacts. Compared to having a fixture with soldered joints, this reduced their heat leak by a factor of three to 0.8 W, which is negligible when compared to the cell's heat input due to radiation of about 10 W. The fingers additionally accommodate the movement of the cell during cooling due to contraction. The downstream wake field suppressor is made of 100 micron thick titanium foil, with slots cut in it so that the gas atoms can diffuse through them. It provides a smooth transition from the elliptical cell to the circular downstream beam pipe. The downstream wake field suppressor is shown in figure 3.4. Both the upstream and downstream suppressors can be seen in position in figure 3.5.

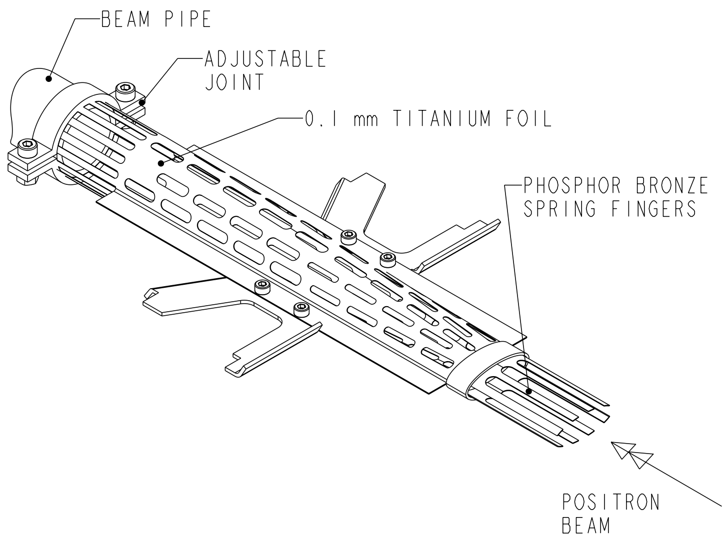

Figure 3.4: The downstream wake field suppressor. The phosphor bronze spring fingers grip the end of the cell. The upstream suppressor consists of the same design for the spring fingers, but without the titanium extension which the downstream suppressor requires.

The Hydrogen storage cell

The hydrogen target cell is shown in figure 3.5. The target cell is cooled to 100 K, the lowest operating temperature possible before recombination of the H atoms takes place at the cell walls. The target density at this temperature is about 7×10^{13} atoms/cm^2. The inside of the cell is coated with Drifilm in order to reduce the amount of atom recombination to form molecules [31].

In bench tests of the cell and target chamber, the temperature difference across the support rails was found to be less than 2 K, with the cell being about 5 K warmer than the cooling rails. In addition it was found that the cell moved 0.2 mm vertically and 0.5 mm horizontally after being cooled down from room temperature to its operating temperature.

Hydrogen atoms are sensitive to beam depolarisation effects. The circulating positron bunches generate transient transverse magnetic fields and thus the magnetic holding field strength must be larger than these generated fields. A superconducting magnet, designed to operate at up to 0.4 T and with a uniformity of 1.5 % provides this field. In choosing the precise field strength to use, care was taken to avoid values that would cause resonant depolarisation [32]. This is when harmonic resonances for a particular transition between spin states are excited by the beam generated rf field. The value of the holding field defines the energy eigenvalues of the spin states and thus defines whether or not the beam will excite a resonance. At the field setting chosen, no depolarising effects have been observed [33].

The ^{3}He storage cell

The geometry of the ^{3}He target cell support structure is slightly different from the hydrogen target cell, as can be seen in figure 3.6. ^{3}He is free from the problems of recombination that atomic hydrogen suffers, and so can be cooled to the lower temperature of 15 K to maximise the target density. The operating target density at this temperature was about 1×10^{15} nucleons/cm^2 [34].

The effect of beam depolarisation is small for ^{3}He, as it has only a nuclear magnetic moment. Only a low holding field of about 10 Gauss is therefore required to define the polarisation quantisation axis. This is provided by conventional

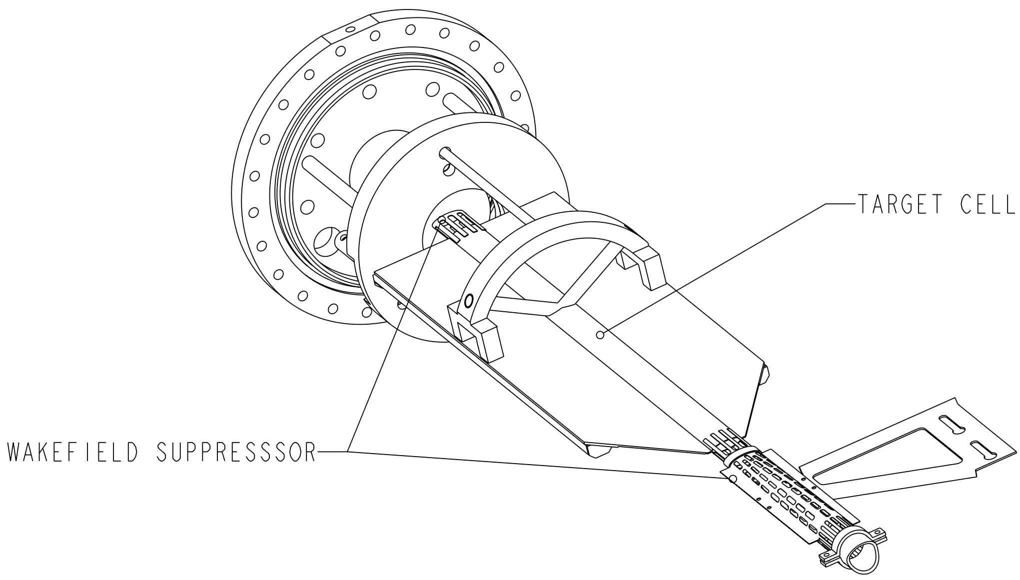

Figure 3.5: The Hydrogen target cell with the wake field suppressors shown in position. The target cell and mounting flange pictured here are inserted into the target chamber enclosure. The cell cooling rails and the inlet and outlet tubes for the ABS/BRP can also be seen.

copper Helmholtz coils. Additional coils around the target chamber are used to correct for the stray fields which originate from the spectrometer magnet.

3.2.2 The Polarised Sources and Polarimeters

The ^{3}He source

The first stage in the polarisation process is to excite a small number of ^{3}He atoms from the ground state $^1S_0$ to the metastable $^3S_1$ state using a weak rf discharge. Transitions are then excited from the $^3S_1$ state to the $^3P_0$ state. This is done within a quartz pumping cell using circularly polarised pumping light from an infrared laser with a weak magnetic field providing the quantisation axis. Angular momentum is transferred from the pumping light to the metastable atoms, whose nuclear spins become polarised. Metastability exchange collisions transfers this nuclear polarisation to the ground state atoms [34, 35]. A schematic diagram of the apparatus is shown in figure 3.6.

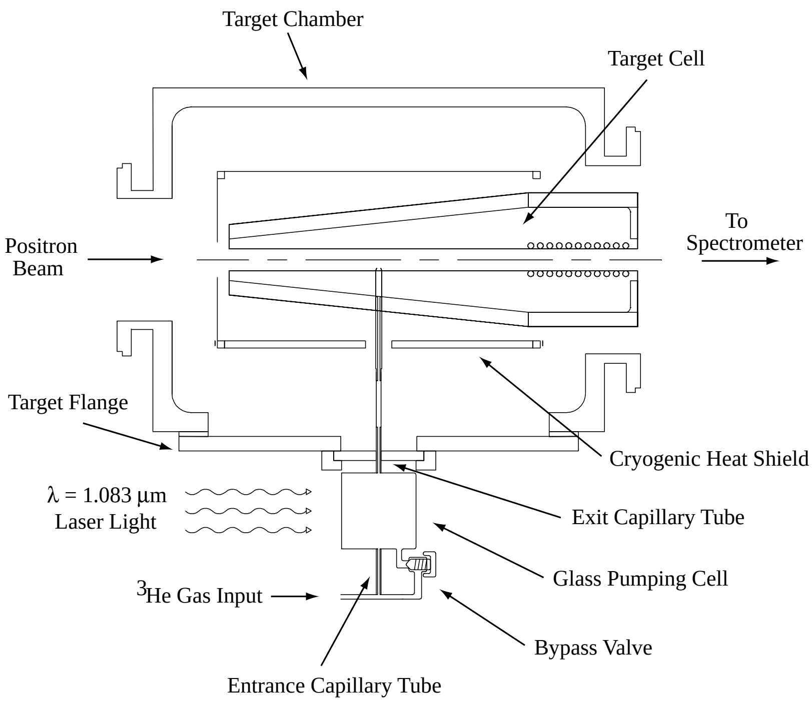

Figure 3.6: Schematic diagram of the ^{3}He target apparatus.

For the 1995 data set, the average polarisation was 46%. The spin state of the target is flipped by reversing the sense of the circularly polarised pumping light. This was done every 10 minutes during the 1995 running.

The ^{3}He Pumping Cell Polarimeter (PCP)

The polarisation of the atoms is measured in the pumping cell by measuring the degree of circular polarisation of the 667 nm transition. This transition occurs as the electronic states of the ^{3}He atoms de-excite, having been excited by the rf discharge. The relation between the degree of circularly polarised light and the nuclear polarisation has been calibrated previously [34, 35].

The Target Optical Monitor (TOM)

The polarisation of the ^{3}He atoms within the target cell itself is additionally monitored. Within the target cell, the ^{3}He atoms are excited by the passing beam and emit light at characteristic wavelengths as they de-excite. Similar to the PCP, the TOM measures the degree of circular polarisation of light from a particular transition in order to extract a value for the nuclear polarisation. The light is reflected away from the beam and into a polarimeter by a mirror system situated 30 cm upstream of the target.

As well as providing a backup system for measuring the target polarisation, the TOM was able to compare the polarisation of the atoms in the target cell with that measured by the PCP in the pumping cell. No significant differences were seen indicating that there were no significant beam induced depolarisation processes taking place [34].

The Atomic Beam Source (ABS)

Atomic hydrogen is produced by rf dissociation of H_2. This then flows through a nozzle and into a high vacuum. The atoms are electron polarised by a Stern-Gerlach separation of states using a sextupole magnet. Rf fields induce transitions which interchange the populations of the hyperfine states such that the states with the required nuclear polarisation are populated. The atoms are then injected into the target cell. The target spin can be flipped by changing the rf field frequency so that hyperfine states with the opposite nuclear polarisation are populated. The limiting time factor in spin flipping is the time taken for the target atoms of the last spin state to diffuse out of the target cell [36, 37].

During the 1996 running, the spin was flipped every 40–70 (s). To reduce any systematic biasing of the data, the sequence of each pair of spin flips was decided randomly. The ABS produces a flux of about $6 \times 10^{16} H_1/s$ with a polarisation of greater than 90%.

The Breit-Rabi Polarimeter (BRP)

The BRP samples the atoms in the target cell and measures their polarisation. The sampling tube for the polarimeter is mounted off axis from the ABS input tube so that no gas atoms can pass directly from the ABS to the polarimeter without at least one wall collision. Using a sextupole magnet, rf transitions and an atomic beam detector, the relative occupancy of the hyperfine states of the H atoms is measured. From this, both the electron and nuclear polarisation can be measured [39, 38].

The Target Gas Analyser (TGA)

The TGA is mounted next to the BRP and shares the same sample tube as the BRP. This measures the relative amounts of mass 1 and mass 2 atoms and molecules using a mass spectrometer. This determines the amount of recombination of the H atoms that has taken place in the target cell and inlet/outlet tubes. This recombination process is dependent on many parameters, including the coating of the cell and the cell temperature. The average atomic fraction for the 1996 running was found to be 0.88 $\pm$0.03. Thus while the BRP measured an average polarisation of H atoms of 92% for the 1996 running period, this does not take into account the molecules present in the target due to recombination, whose polarisation is unknown. Additionally both the TGA and BRP take samples at the center of the cell and give no information as to whether there is any gradient in the target polarisation along the length of the cell. Studies are ongoing to clarify the situation [31].

The Hydrogen Target Polarisation

The most general expression for the target polarisation can be written,

$$P_T = \alpha_0(\alpha_r C_\alpha + (1 - \alpha_r C_\alpha \beta)) \cdot P_{BRP} C_{BRP}, \tag{3.3}$$

where

P_{BRP} is the polarisation measured by the BRP,

C_{BRP} is the sampling correction for the BRP,

$(1 - \alpha_0)$ is the fraction of molecules produced after the dissociation process (and thus known to be unpolarised), measured to be 0.03,

$(1 - \alpha_r)$ is the fraction of molecules produced by recombination,

C_α is the sampling correction for the molecular fractions and

β is the polarisation of the molecules which are formed after recombination.

The corrections C_{BRP} and C_α are present because the atoms and molecules are sampled at one point in the cell (the middle) and have travelled down sample tubes before they are analysed. Thus they may not be representative of all the atoms and molecules within the cell. Neither these corrections nor the polarisation of the molecules, β, have been determined yet.

While this uncertainty over the target polarisation exists, the inclusive spin asymmetry, A_1^p, measured by HERMES can be compared with world data and thus the target polarisation checked. It has been found that using the expression

$$P_T = P_{BRP} * \alpha_0 * (\alpha_r + (1 - \alpha_r) * 0.5) \tag{3.4}$$

for the target polarisation gives good agreement between the world data on A_1^p and the HERMES result [40].

3.3 The Spectrometer

In order to measure the semi-inclusive channel, a wide angled spectrometer is used. The lower angle of the acceptance is limited by an iron septum plate which is mounted in the middle of the spectrometer magnet to shield the beam lines from the field. The acceptance covers the range of scattering angles of 40–220 mrad. The kinematic plane for a 27.5 GeV positron beam is shown in figure 3.7. Within the DIS cuts used (described in chapter 5), the acceptance covers most of the kinematic region for a range in x of 0.02–0.6.

The layout of the detectors is shown in figure 3.8. As can be seen, it is symmetric about the x-z plane, with each individual detector made up of an identical upper and lower half, with the proton and positron beam pipes passing through the central plane.

A detailed description of the spectrometer and each of its components can be found in [41, 42].

3.3.1 The Spectrometer Magnet

A dipole magnet produces an integrated field of 1.3 Tm to deflect the particles in the acceptance according to their momenta. The variation of the field is less

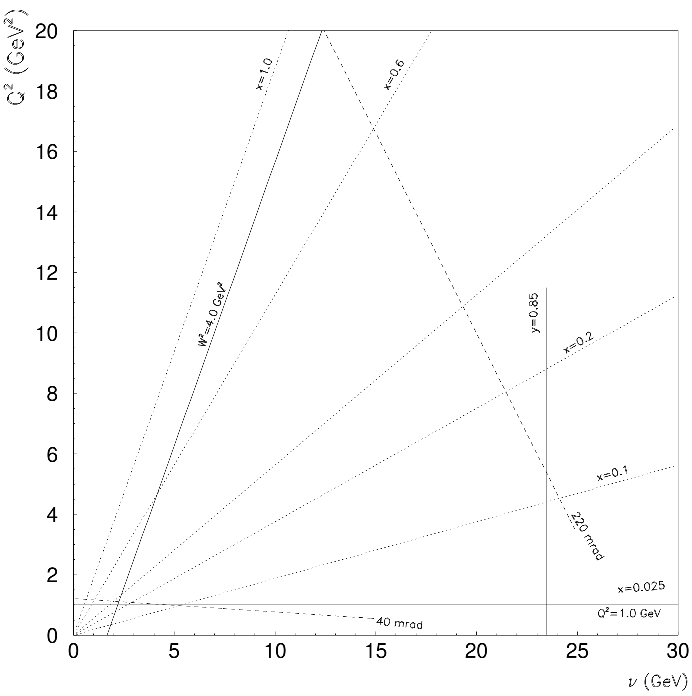

Figure 3.7: The kinematic plane accessible with the HERMES spectrometer and a 27.5 GeV beam. The dashed lines show the limits of the acceptance. The solid lines show the applied DIS cuts (described in chapter 5). The dotted lines show the contours of x.

than 10% over the acceptance. Field clamps are mounted in front of and behind the magnet such that the fields in the nearest front and back chambers are less than 0.1 T.

3.3.2 The Tracking Chambers

The tracking system consists of drift chambers and gas microstrip detectors in front of the spectrometer magnet (the front region), drift chambers behind the magnet (the back region) and proportional chambers within the magnet itself.

As well as vertical wires (X planes), two additional planes tilted at 30° to the vertical were used (U and V planes). The U and V plane configuration was used because in the back region the detectors are too wide to allow horizontal wires to be used for measurement of the y position. The same configuration was used for each tracking chamber module for ease in the reconstruction of tracks.

With all tracking chambers functional, the momentum resolution is limited by

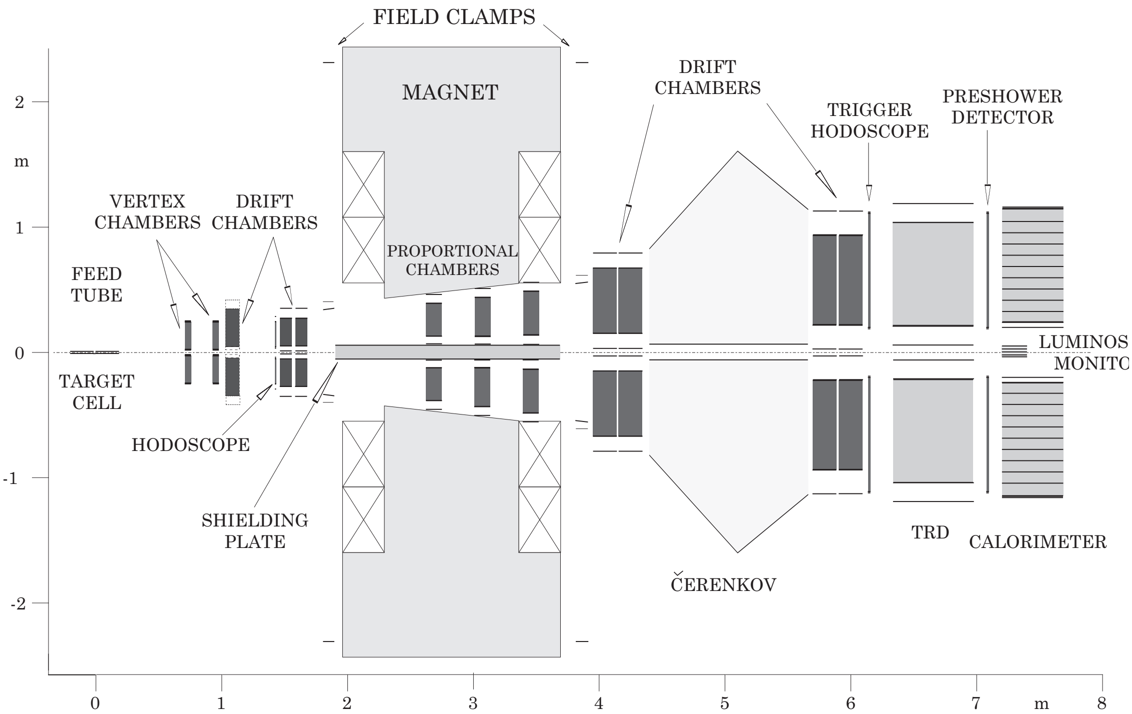

Figure 3.8: The layout of the HERMES spectrometer. This is an elevation. The horizontal axis in the figure defines the z-axis of the experiment, the vertical axis the y-axis ; the x-axis comes out of the page.

bremsstrahlung in the target cell walls, target chamber window and first tracking detectors. The resolution of the scattering angle is limited by multiple scattering in the same material.

The Vertex Chambers (VC)

These make an accurate determination of the vertex position of the interaction. Operating only 5 mm from the beam pipe, gas microstrip detector technology was chosen over conventional drift chambers in order to cope with the large backgrounds present. The chambers are made of a low Z material to minimise multiple scattering, such that for positrons with momentum less than 7 GeV the angular resolution is limited by multiple scattering in the target chamber window rather than in the VC's.

The Drift Chambers

The drift chambers are constructed of alternating planes of sensing anode wires at ground potential between cathode foils set at high negative potential. Modules of drift chambers are used each with six layers containing UU',VV' and XX' planes, where the U'V'X' are staggered with respect to their UVX partners by half a drift cell width in order to resolve left right ambiguities. A gas mixture of Ar(90%)CO_2(5%)CF_4(5%) was used, this non-flammable gas was required due to the safety requirements of the tunnel environment of the experiment. Drift cell sizes for the front chambers (FC) are 7 mm and for the back chambers (BC) 15 mm. The front chambers consist of two identical modules in each detector half located upstream of the spectrometer magnet. The back chambers consist of four modules in each detector half, BC1/2 situated immediately downstream of the magnet and the slightly larger BC3/4 situated downstream of the Čerenkov detector. The resolutions achieved by both sets of chambers was about 220 μm.

The Magnet Chambers (MC)

Tracking chambers in the space inside the spectrometer magnet are used to resolve front/back tracking ambiguities and also to detect the relatively low energy tracks which are deflected out of the rear tracking acceptance by the spectrometer magnet. Proportional chambers are used as they can function within the high magnetic fields that exist and a resolution of only ± 1 mm is required in any case. Three modules each with U,V and X planes are used, with a 4 mm spacing between the cathode and anode planes. The centre of each module is separated by 21 mm.

Performance of Tracking Chambers

During both the 1995 and 1996 running periods, the VC's operated with very high noise and many inactive planes due to hardware problems. For both the 1995 and 1996 analysis, no VC information has been used, and front tracks were reconstructed with the FC's alone. Additionally the MC's suffered from hardware failures which also precluded their use in the reconstruction of tracks in 1995. They were fully operational for the 1996 running.

Using this configuration of detectors, in 1995 the momentum resolution for positrons was 1–2 %, depending on kinematics, and the average angular resolution was 0.6 mrad.

3.3.3 The Particle Identification Detectors

The four particle identification detectors separate positrons and hadrons very efficiently, producing a total hadron rejection factor of 10^4, which corresponds to a positron sample with less than 1 % hadron contamination for an average efficiency of 98 % (the PID analysis scheme is described in section 5.3). In addition, the threshold Čerenkov detector separates out a clean pion sample from other hadrons above a certain momentum threshold.

The Calorimeter

The calorimeter serves three functions, it measures the energy of electrons and positrons from radiative processes or π^0 and η decays, it is used as a first level trigger, based on the energy deposited in a localised area, and it provides particle identification information.

Each half of the detector is constructed of an array of 42×10 blocks of lead glass, each with area 9×9 cm^2 and length 50 cm^2, which corresponds to about 18 radiation lengths. The emitted light is detected by a photomultiplier tube connected to each block at the rear of the stack. The energy resolution can be parameterised as

$$\frac{\sigma_E}{E} = \frac{5.1(\%)}{\sqrt{E(\ GeV)}} + 1.5(\%).$$

The spatial resolution of the impact point has been found to be 0.7 cm.

Unlike positrons, hadrons do not deposit all their energy in the calorimeter and hence positron/hadron separation can be achieved by considering the ratio of E/p where the momentum is measured by the spectrometer magnet. The pion rejection factor for the calorimeter alone, defined as the total number of pions divided by the number of pions misidentified as positrons, is about 2500 for a positron efficiency of 95%.

During injection and dumping of the beam, when radiation is high near the beam pipes, the two detector halves are raised by 50 cm away from the beampipe in order to minimise the radiation damage of the lead glass.

The Hodoscopes

Two hodoscopes, H1 and H2, are used to produce triggering information, and H2 is additionally used to provide particle identification information. Each consists of 42 scintillating modules 1 cm thick and 9.3×91 cm^2 in area stacked vertically, with a photomultiplier tube connected via a light guide to each module. H1 is situated in front of the TRD and H2 in front of the calorimeter.

An 11 mm thick lead sheet sandwiched between two 1.3 mm thick stainless steel sheets is positioned immediately in front of the H2 scintillators. Particles traversing this sheet will initiate showering. Due to the different longitudinal showering characteristics of electromagnetic and hadronic showers, electrons and hadrons will deposit different amounts of energy in the H2 scintillators, and this information can be used to discriminate between positrons and hadrons. The pion rejection factor for a positron efficiency of 95% is about 10.

In 1995, between 20 and 100 triggers per second were generated from showers originating from the proton beam, compared to 35 positron triggers. A hodoscope in the forward region, H0, was added in 1996 to eliminate this background. This hodoscope consists of a 3.2 mm thick (0.7% of a radiation length) plastic scintillator for each half of the detector placed in front of the front drift chambers and read out with a single photomultiplier tube for each half. Backward going tracks, associated with background from the proton beam pipe, were eliminated using a time of flight method.

The Transition Radiation Detector (TRD)

Highly relativistic particles crossing a boundary between two materials with different dielectric constants emit transitional radiation. In the HERMES kinematics, only positrons have a high enough γ factor (the Lorentz factor) to produce this radiation in the form of X-rays. As hadrons do not produce this radiation, they can be separated from positrons. The TRD is made of six modules each with a 6.35 cm radiator consisting of randomly orientated polypropylene fibers (which corresponds to an average of 267 dielectric layers) and a multiwire proportional chamber to detect the radiated X-rays. Each proportional chamber has 256 vertical wires and cathode foils stretched to high tension to maintain its relative position. The chambers are filled with a Xe/CH_4 gas mixture, chosen for its high absorption of X-rays. The pion rejection factor for a 90% positron efficiency is 100-120.

The Čerenkov Detector

When the velocity of a charged particle traversing a dielectric medium exceeds that of light in that medium, Čerenkov light is radiated. The minimum value of β of the particle, where $\beta = v/c$ and v is the velocity of the particle, for Čerenkov light to be emitted is $\beta_t = 1/n$, where n is the refractive index of the medium. The Čerenkov counter is situated between BC1/2 and BC3/4 and contains 1.17m of gas radiator. The Čerenkov light is reflected onto photomultiplier tubes with an array of 20 spherical mirrors mounted at the rear of the detector. The mean number of photoelectrons detected for a particle with β close to one is slightly less than three.

In 1995 the gas radiator was chosen to be pure Nitrogen, which resulted in

Čerenkov momentum thresholds for pions, kaons and protons of 5.6, 19.8 and 37.6 GeV respectively. In 1996 this threshold was changed by using a gas mixture of Nitrogen and C_4F_{10} (70%:30%) which resulted in momentum thresholds of 3.8, 13.6 and 25.8 GeV respectively. Thus the identified pion sample in 1995 covered a momentum spectrum of 5.6–19.8 GeV and in 1996 3.8–13.6 GeV. The relatively high momentum threshold for 1995 was set because the collaboration's goal in the first year of running was an accurate inclusive measurement. The Čerenkov threshold was therefore set to optimise the inclusive PID by providing redundancy in case one of the other PID detectors failed. The 1995 Čerenkov setting resulted in 12 % of hadrons being identified as pions and with the 1996 setting 40 % [43].

3.3.4 The Luminosity Monitor

The lumininosity is measured by detecting the interactions of the beam positrons with the electrons of the target nucleons. The interactions monitored are Bhabha scattering, $e^+e^- \rightarrow e^+e^-$, and electron-positron annihilation, $e^+e^- \rightarrow \gamma\gamma$. The rates of these interactions are proportional to the density of the target and the size of the beam current.

To make the measurement, a small calorimeter 7.2 m downstream of the target detects positrons and electrons arriving in coincidence. The horizontal acceptance of the calorimeter is 4.6–8.9 mrad. Only the relative luminosities in each spin state are required for spin asymmetry measurements, thus the absolute acceptance of the detector is not required to be known. The calorimeter is made up of 2×2×200 mm^2 Čerenkov crystals made of $NaBi(WO_4)_2$, chosen for its radiation hardness, with photomultiplier tubes to detect the emitted light. The calorimeter is moved 20 cm in the horizontal plane during injection and dumping of the beam to reduce radiation damage. The Bhabha scattering rate detected for a beam current of 20 mA and ^{3}He target density of 1×10^{15} is 132 Hz, which gives 1% statistical accuracy within 100 s.

3.3.5 The Gain Monitoring System (GMS)

The GMS is used to monitor gain shifts in the photomultiplier tubes of the hodoscopes, calorimeter, Čerenkov and luminosity detectors. Laser light produced by a dye laser system is piped into each photomultiplier tube and additionally to a high stability reference photodiode. The output signals from the photodiode and from each individual photomultiplier tube are compared for different intensities of the laser light. With this information, relative gain shifts can be monitored. No degradation of performance of the photomultiplier tubes has been observed so far.

3.4 The Data Acquisition

3.4.1 The Trigger

A trigger is used to discriminate between deep inelastic scattering events and background events before the detector responses are recorded. The main source of background is from hadrons either produced from beam interactions with the collimators or from photoproduction processes in the target. Within 500 ns of an event occuring, a decision is made on whether or not to initialise the readout electronics. For this to happen, for a DIS positron event it was required that in coincidence with an incident positron bunch from the accelerator, there were hits in the three hodoscopes, H0, H1 and H2 (in 1995 only H1 and H2), and there was a cluster of sufficient energy in the calorimeter. This minimum energy was set to $>$3.5 GeV in 1995 and $>$1.4 GeV in 1996. This resulted in a typical trigger rate in 1995 of 50 Hz for a luminosity of 5×10^{32} nucleons/cm^2/sec. After analysis of the data, it was found that about two thirds of these triggers had tracks and 95% of the reconstructed tracks came from the target.

3.4.2 The Data Acquisition System (DAQ)

The DAQ was capable of recording an event rate of up to 150 Hz for the 1995 and 1996 running periods. The dead time was generally less than 10%. Data are written to disk over the course of the 8–12 hour “fill” of the storage ring. The data are further subdivided into “runs”, which correspond to about 10 minutes of data taking. Data which do not change on an event by event basis (“slowcontrol” data), such as the target polarisation or luminosity rate, are recorded every 10 seconds. This is known as a “burst”.

3.4.3 The Reconstruction Program

Tracks were reconstructed from information on hits in the tracking chambers by the HERMES reconstruction program (HRC) [44]. For track finding, the program uses a tree search algorithm, whereby the whole hit pattern is considered with a resolution that increases in steps until the resolution of the detector is reached. At each step the pattern is checked to see if it is consistent with an allowed track. Partial tracks are found in front of the spectrometer magnet and behind it, and subsequently these partial tracks are matched up. The whole procedure is very fast as it does not involve any calculations to be performed during reconstruction, only look up tables are used. Similarly, momentum look up tables are used to determine the momenta of the tracks. A large table is created once only which contains the positions and slope parameters for each possible track and the momenta that correspond to these tracks. During reconstruction, each track found is then compared with this table to determine its momentum.

Chapter 4

Monte Carlo Simulation Studies

4.1 The Simulation Program

The partonic level quantities of Δu, Δd and $\Delta\overline{q}$ distributions are unfolded from the measured hadron asymmetries using the Monte Carlo (MC). It is vital, therefore, that the MC describes the experimental data properly. Particularly important is the modelling of the fragmentation process, which has parameters that need to be tuned to the experimental data. This is described in this chapter, and in addition studies are made of the MC hadron asymmetries which justify the cuts chosen for real data and give some understanding of the effects which dilute the physics asymmetries.

4.1.1 The Monte Carlo Event Generator

The simulation of a DIS interaction by the MC is undertaken in three separate stages. This is illustrated in figure 4.1.

The PEPSI event generator [45, 46] was used to simulate polarised DIS interactions. The LEPTO event generator code simulates unpolarised DIS interactions [48] and PEPSI is an extension to it which adds the ability to simulate longitudinally polarised nucleons and leptons as initial state particles. PEPSI simulates the physics of the DIS interaction and the evolution of the partonic system immediately after the interaction by calculating spin dependent matrix elements to first order in α_s, the strong coupling constant.

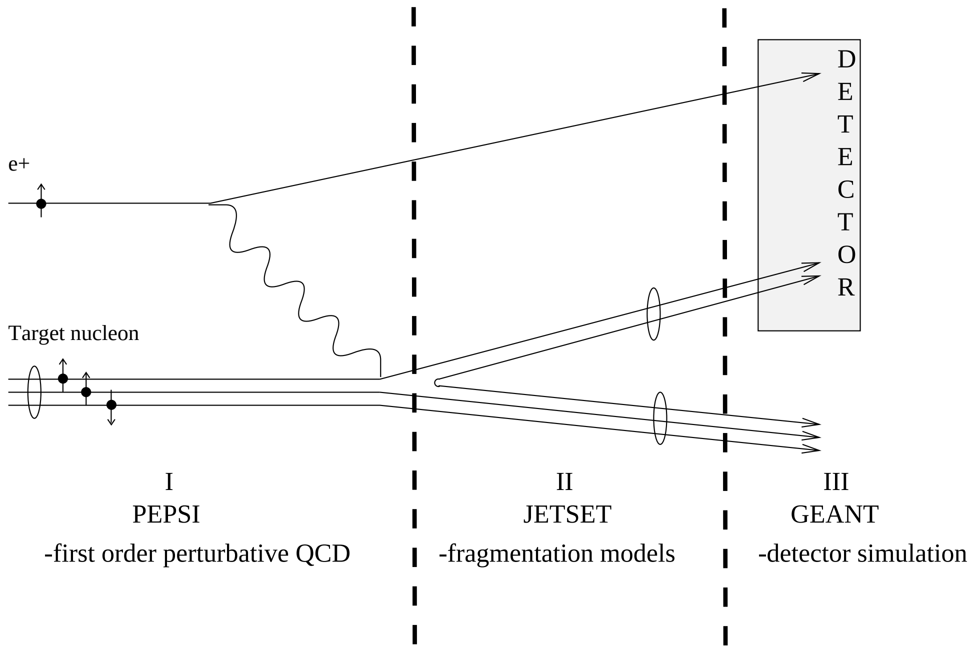

Figure 4.1: Schematic showing how the DIS process and subsequent fragmentation is simulated by the Monte Carlo.

As the distance between partons becomes larger, α_s becomes large due to the confinement property of QCD. Perturbative QCD can no longer be applied and for this second stage of the simulation process, where the coloured partons are transformed into colourless hadrons, there is no calculable theory, only phenomenological models. The Lund string fragmentation model [49] has been chosen for this analysis. This second stage of fragmentation is dealt with by the JETSET code [50].

The output after these two stages of simulation (known as event generator level MC) is events which would be observed by a perfect detector – the identification and kinematics of all particles arising from each interaction is known and there is no particle mis-identification or detector smearing.

To take the simulation a stage further, as is done in the full HERMES Monte Carlo (HMC) [51], the particles produced by the event generator can then be tracked through the detector with the GEANT code [52]. Physics interactions which occur within the detector are simulated, such as the production of secondary particles, the decay of unstable particles and the effect of the spectrometer magnet on particle trajectory. Additionally the response of each detector is modelled. The final output from this full simulation is at an equivalent level to that of the experimental data – i.e. particle tracks have to be reconstructed from hits recorded in the detectors in just the same manner as for the experimental data.

The full MC simulation is extremely time consuming, taking a factor of $\sim 10^4$ more cpu time per event than the event generator level MC. If the effect of the detector is assumed constant for each spin state, then in a spin asymmetry it will cancel out. In fact, a study has been done using the full MC which showed that both the acceptance and all simulated processes within the detector have a negligible effect on the inclusive positron asymmetry [53, 54]. The event generator level of MC is therefore sufficient when simulating spin asymmetries.

4.1.2 Configuration of Event Generator

The event generator was configured to model the HERMES experiment as closely as possible.

Events were generated within the HERMES kinematic range, namely

- $E_{Beam} = 27.52\, GeV^2$
- $Q^2 \; > \; 1.0\, GeV^2$; $W^2 \; > \; 4.0\, GeV^2$; $y \; < \; 0.85$

In order to model the detector acceptance, a simple geometric acceptance cut was implemented,

- $0.040 <\mid \theta_y \mid< 0.140$
- $\mid \theta_x \mid< 0.140$

and additionally a minimum momentum cut of 1.0 GeV was applied to all generated particles. The cut on θ_x is tighter than that for real data due to the fact that PEPSI does not have any simulation of the magnetic field in the detector (without the magnetic field the acceptance would be narrower).

To account for the Čerenkov detector thresholds set in the real experiment (see chapter 3), for ^{3}He data the momentum cut for identified pions was set to

- $6.0 < p < 21.0\,GeV$

whereas for proton data this was set to

- $4 < p < 13.5\,GeV$.

As interactions in the detector are not modelled, all unstable particles which in reality would decay within the detector volume (such as K^0_S,$K^{\pm}$,ρ^0,Λ, etc) were allowed in the event generator to decay at the interaction point.

The QCD calculations performed by the event generator require both unpolarised and polarised parton distributions. For the MC studies presented in this chapter, the Gehrmann-Stirling parameterisation was used for the polarised distributions [19]. This differs only slightly from the GRVOG parameterisation in that all points are evolved to a fixed Q^2 of 4 GeV^2, whereas in HERMES a range of Q^2 exists over the x range. While the differences are very small, the GRVOG parameterisation, which is able to evolve to different Q^2 values, is more correct and has been used for the rest of the thesis. The unpolarised distributions were taken from the parameterisation of Glück, Reya and Vogt [55].

The events were generated on Pentium-Pro 200 PC's at a rate of about 17k events per minute.

4.2 Simulation of the Fragmentation Process

4.2.1 The String Fragmentation Model

The QCD prediction of linear confinement is the basis of the string fragmentation model. As a q and $\overline{q}$ move apart from each other in the centre of mass frame, a colour flux tube (or string) can be pictured stretching between them. The potential energy stored in this string increases as the quark separation increases until at some point it will break through the production of a $q\overline{q}$ pair. This process of string breaking continues until only on-mass-shell hadrons remain. The production of $q\overline{q}$ pairs is governed by a quantum mechanical tunneling mechanism and the relative probability for this is given by

$$exp\left(-\frac{\pi m^2}{\kappa}\right)\left(-\frac{\pi p_\perp^2}{\kappa}\right). \tag{4.1}$$

Here m is the mass of the quark, κ is the string constant (the amount of energy stored per unit length) and $p_\perp$ is the transverse momentum of the quark. The string itself has no transverse momentum, so $p_\perp$ of each quark produced in a pair is balanced by its partner. The resultant hadrons will have a $p_\perp$ made up from the sum of $p_\perp$'s of their constituent quarks. As can be seen from equation 4.1, the p_x and p_y distributions are Gaussian in shape. The width of these distributions are defined through the use of a free parameter, the root-mean-square $p_\perp$ of a quark (parameter PARJ(21) in the JETSET code).

The way in which the energy and momentum is shared between each hadron produced after each string break is defined by the 'Lund symmetric fragmentation function' [56]

$$f(z) \propto z^{-1}(1-z)^a exp\left(\frac{-b(m^2+p_\perp)}{z}\right), \tag{4.2}$$

where z is the energy taken by each hadron from the remaining available energy,

$$z = \frac{(E+p_z)_{new}}{(E+p_z)_{old}}, \tag{4.3}$$

and m is the hadron's mass and $p_\perp$ its transverse momentum. Here a and b are free parameters (parameters PARJ(41) and PARJ(42) in the JETSET code).

In the DIS case of a parton being knocked out of the target nucleon, leaving a remnant, the simplified example outlined above needs to be modified. If the struck parton is a valence quark, then the remnant is a diquark and hadronisation takes place in the way described above for the simple quark-antiquark system, but with the production of quark-antiquark pairs and diquark-antidiquark pairs until hadrons are formed. If the struck quark is a sea quark then in the resulting four quark system, a baryon or meson is produced depending on whether the left over partner of the struck sea quark is a quark or antiquark, respectively, leaving the other parton system to hadronise in the normal way.

4.2.2 Fitting the Fragmentation Parameters

The default free parameters in JETSET (PARJ(21),PARJ(41) and PARJ(42)) have been fitted to high energy e^+e^- data from LEP. While the fragmentation process is assumed to be equivalent for both e^+e^- and DIS interactions, these parameters are dependent on the QCD effects that are included in the MC. The default parameters were determined for a MC with higher order QCD effects simulated by parton showering and leading log approximations, which is important for high energy experiments which require simulations of jets and multijet effects [48]. As HERMES does not have high enough energy to produce jets, only first order matrix elements are calculated and no parton showering has been implemented. The MC for which the default JETSET parameters are valid is therefore very different from that used for simulations of the HERMES kinematic region, and thus it is necessary to adjust the fragmentation parameters such that the MC data gives an accurate description of the experimental data.

The procedure for fitting the MC data to the experimental data by changing the fragmentation parameters is summarised in figure 4.3. The event generator level MC was used for the fitting because to use the full MC simulation would be prohibitively time consuming. In order to compare this level of data with experimental data, a correction for detector effects such as detector efficiency and resolution and track reconstruction efficiency was made. This was done by multiplying each bin i of each distribution of the experimental data by correction factors,

$$D_{i\ CORRECTED} = \frac{D_{i\ EVENT\,GENERATOR}}{D_{i\ FULL\,MC}} * D_{i\ EXPERIMENTAL}. \tag{4.4}$$

The detector correction factor for the z distribution is shown in figure 4.2. A study has been done to identify the individual contributions to this correction factor [57]. It was found that about 14 % of generated positrons are lost due to tracking and reconstruction inefficiencies. About 7 % of generated hadrons are lost by absorption and bending within the detector volume. Particle identification and trigger efficiencies make up the remaining small losses. The rise of the correction factors at high z is caused by the higher $\frac{dE}{dx}$ losses in the detector for high energy hadrons.

The corrected data was then compared to the event generator level data. The z and $p_\perp$ distributions, in five separate bins in Q^2 (1-2 GeV^2, 2-4 GeV^2, 4-6 GeV^2,6-

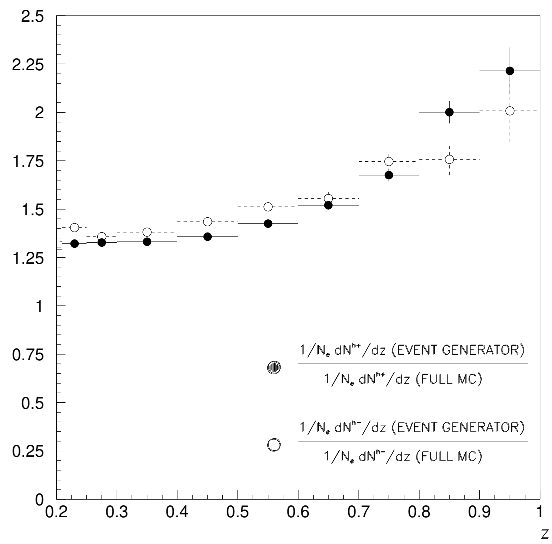

Figure 4.2: The detector correction factor for the z distribution of positive (closed circles) and negative (open circles) hadrons.

10 GeV^2 and >10 GeV^2) and for positive and negative hadrons separately were used for fitting within the ranges

- $0.2 < z < 0.9$
- $0.1 < p_{\perp} < 0.9$

An iterative fitting procedure was used whereby the event generator was run using a particular set of trial parameters and the difference between the generated data and corrected experimental data for each bin, measured in units of χ^2, was then calculated. The fitting algorithm then chose another set of trial parameters and the event generator would run again. These steps were repeated until the χ^2 was minimised.

The fragmentation process is independent of the polarisation of the particles involved in the interaction. It is acceptable therefore to use unpolarised data for the fitting procedure. Unpolarised proton data was used because more unpolarised experimental data was available than polarised data at the time the fit was carried out (higher unpolarised target densities are achievable compared to polarised target densities). The selection cuts for this experimental data were the same as those described in section 4.1.2 for the MC. Additionally, the detector response cuts and data quality cuts used were the same as are described in chap-

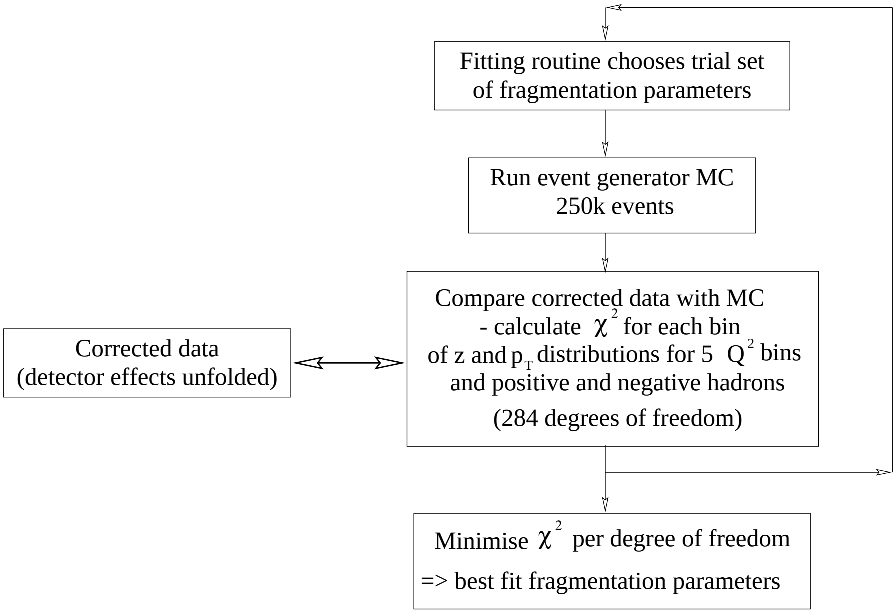

Figure 4.3: Schematic showing procedure for fitting the Monte Carlo fragmentation parameters.

ter 5, except for the fact that for this case the data is unpolarised so that target and beam polarisation cuts are irrelevant. Each generated sample consisted of 250 000 events.

The optimum parameters found after this tuning procedure are shown in table 4.1. To see the effect of the change in PARJ(41) and PARJ(42), the Lund fragmentation function calculated using the default parameters and the fitted parameters is shown in figure 4.4. The result of the fit is to create more low energy string breaks, resulting in more low energy hadrons after fragmentation. This is to be expected as the MC uses only matrix elements calculations for the hadronisation, and thus this 'softening' and 'widening' of the fragmentation process accounts for low energy parton emission which would otherwise be explicitly simulated by higher order QCD simulations for which the default parameter set were tuned [48].

The full MC (HMC) has been produced with the default fragmentation parameters and with the fitted fragmentation parameters. Figure 4.5 shows the z distributions of hadrons for these samples compared to experimental data. The deficit in the number of low z negative hadrons is not understood at present and

Parameter name	Default value	Fitted value
PARJ(21)	0.36	0.34
PARJ(41)	0.30	0.82
PARJ(42)	0.58	0.24

Table 4.1: The JETSET parameters before and after the fitting.

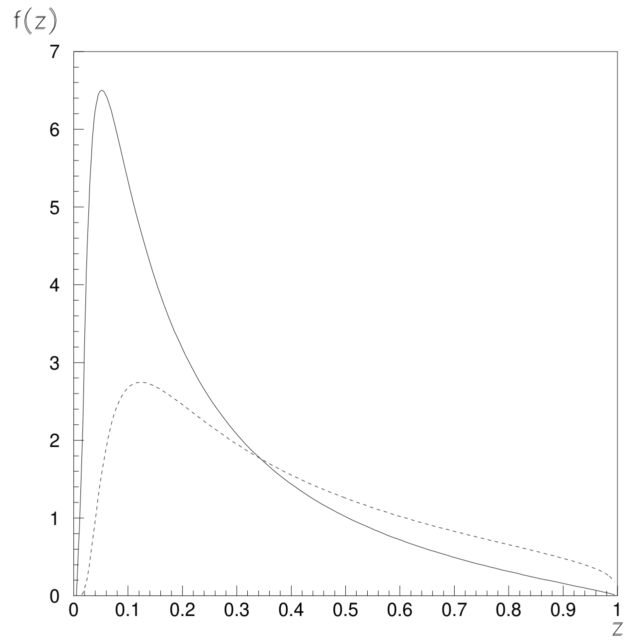

Figure 4.4: The Lund symmetric fragmentation function. The dotted line shows the function drawn with JETSET default parameters (tuned for LEP experiments), the solid line shows the function drawn with the parameters tuned to HERMES data. This is drawn for pions with average $p_\perp$ of 0.45 GeV (as measured at HERMES).

studies are ongoing into understanding the cause of it.

(a)

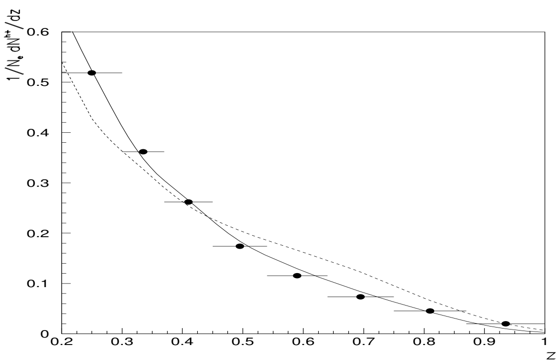

(b)

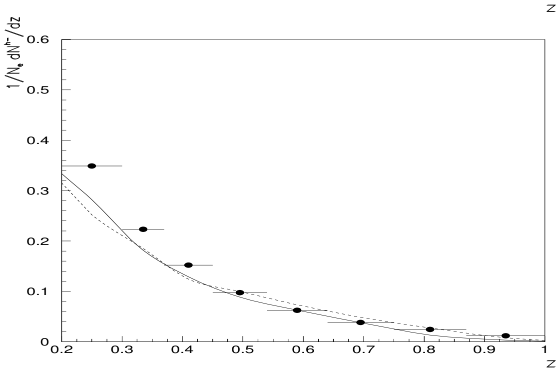

Figure 4.5: The z distribution for (a) positive and (b) negative hadrons. The closed circles are experimental data, the dashed line HMC with default fragmentation parameters and the solid line HMC with the fitted fragmentation. As can be seen, the result of the fitting is to increase the proportion of low energy particles and decrease the proportion of high energy particles.

4.3 Simulation of Asymmetries

The asymmetry calculated from Monte Carlo data

Denoting the parallel spin state as + and the antiparallel spin state as $-$, the MC asymmetry can be expressed as

$$A^h(x) = \frac{N^h_-(x)L_+ - N^h_+(x)L_-}{N^h_-(x)D^h_+(x,Q^2)L_+ + N^h_+(x)D^h_-(x,Q^2)L_-} \tag{4.5}$$

where h represents any of the six possible hadron combinations, namely $h = (h^+ - h^-), (h^+), (h^-), (\pi^+ - \pi^-), (\pi^+), (\pi^-)$. $N^{h\pm}_\pm$ is the number of hadrons type $h^\pm$ in coincidence with a DIS positron in spin state (+) or ($-$). The beam and target polarisations are 100% in the MC and hence there is no correction required for these quantities. $L_{\pm}$ is the MC luminosity, defined as

$$L_{MC} = \frac{Number\ of\ events\ generated}{Cross\ section\ of\ process} \tag{4.6}$$

$D_{\pm}^{h\pm}(x, Q^2)$ is the virtual photon depolarisation factor discussed in the next section.

To compare the measured MC asymmetries with a theoretical prediction, it is useful to use the charge difference spin asymmetry. To do this for the single hadron spin asymmetries would require knowledge of the fragmentation functions, as was discussed in section 2.3.3. Thus for the MC studies presented in the rest of this chapter, the charge difference asymmetry has been studied, requiring only the parton distribution functions as input to the theory (equation 2.32). The conclusions derived for the charge difference asymmetry hold also for the single hadron asymmetries.

The depolarisation factor

The depolarisation factor of the virtual photon is a kinematic factor calculated from QED to be

$$D(x, Q^2) = \frac{y(2-y)(1+\frac{1}{2}\gamma^2 y)}{y^2(1+\gamma^2) + 2(1-y-\frac{1}{4}\gamma^2 y^2)(1+R(x,Q^2))} \tag{4.7}$$

where $y = \nu/E$, $\gamma^2 = Q^2/\nu^2$ and $R(x, Q^2) = \sigma_L/\sigma_T$. All photons are transversely polarised in the MC and hence R is set to zero in this case. This depolarisation factor is averaged over Q^2 and calculated separately for each hadron type, charge and spin state. Figure 4.6 shows this depolarisation factor for h^+ and h^- for experimental data.

Simulation of ^3He target

The wave function for ^{3}He is dominated by the configuration where the proton spins are opposite to each other and thus pair to zero. The simulation of this configuration by PEPSI is called "ideal" ^{3}He. In reality, the proton spins do not completely cancel and there is a small residual proton polarisation (-2.7%) [58]. This situation can also be simulated by PEPSI when configured to simulate "real" ^{3}He. The difference for the charge difference pion asymmetries is shown in figure 4.7.

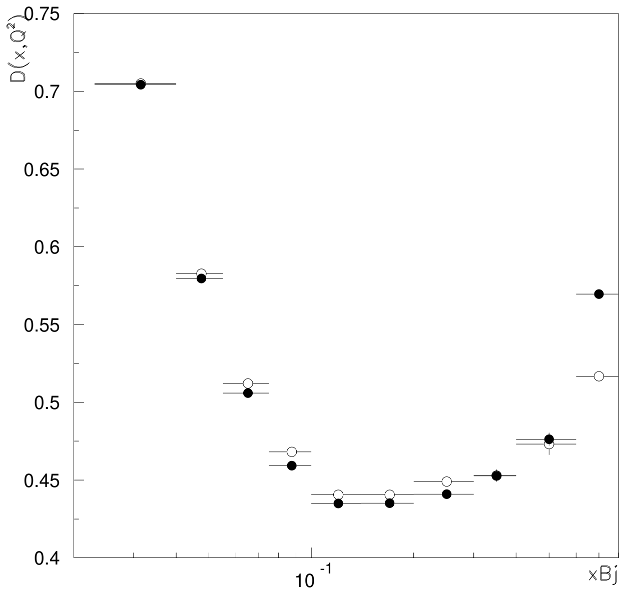

Figure 4.6: Photon depolarisation factor $D(x, Q^2)$ averaged over all Q^2 for h^+ (closed circles) and h^- (open circles) events. This is taken from experimental data (1995 data set).

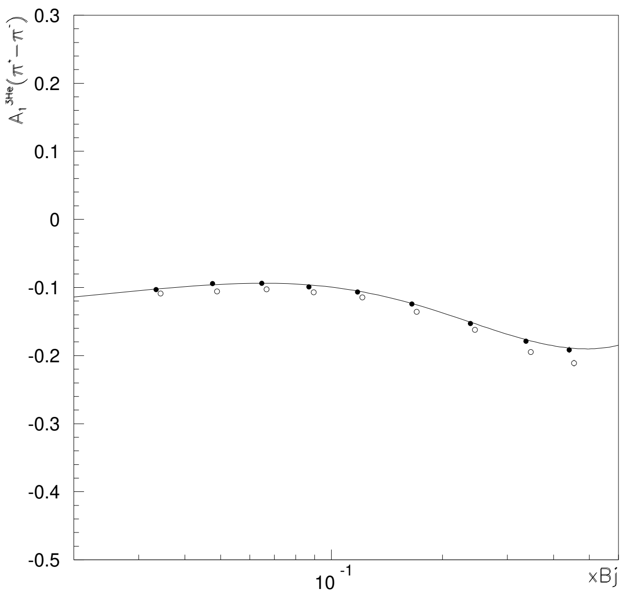

Figure 4.7: Comparison of charge difference pion asymmetry for simulation with an "ideal" (closed circles) and a "real" (open circles) ^{3}He target. In order to make easy comparisons, the x and y scales are kept the same as for other figures in this chapter.

4.3.1 Results of Asymmetry Simulations

To check the integrity of the MC, a 4π detector was simulated with an ideal fragmentation process. The table below describes this scheme:

Struck Quark Flavour	Final state hadron produced
u	π^+
$\overline{u}$	π^-
d	π^-
$\overline{d}$	π^+
s,$\overline{s}$ switched off as gluons switched off	

Only with this perfect fragmentation scheme can the theoretical prediction for the asymmetry be produced, as shown in figure 4.8. Additionally, this test shows that the MC can reproduce its input theory.

Dilutions of the asymmetry

As already discussed, it is important to minimise the contamination of the pion sample from target and central region fragments. A useful variable to use a selection cut on to reduce target contamination is x_F, a measure of the fraction of the longitudinal momentum carried by the final state hadron in the centre of mass system ($x_F = p_L^*/W$, where p_L^* is the longitudinal momentum of the hadron in the centre of mass system). Target fragments are generally at negative x_F and central region fragments at low x_F while the current region fragments are at high positive x_F. Figure 4.9 shows that the HERMES detector acceptance predominantly accepts only leading hadrons and thus most target fragments are not detected. By additionally applying a minimum x_F cut on the hadron sample, one can maximise the contribution from the current region. A minimum cut on z, the energy fraction carried by the pion ($z = E_h/\nu$), also helps to isolate the current region. As W^2 increases, the separation between current and target regions increases [59]. Thus a minimum W^2 cut of 10.0 GeV^2 is applied to make the x_F and z cuts more efficient at isolating the current region.

Figure 4.10 shows the charge difference pion asymmetry for standard kinematic cuts for both an "ideal" ^{3}He and a proton target. The theory lines drawn for each target have been calculated for an "ideal" ^{3}He and for a proton tar-

(a)

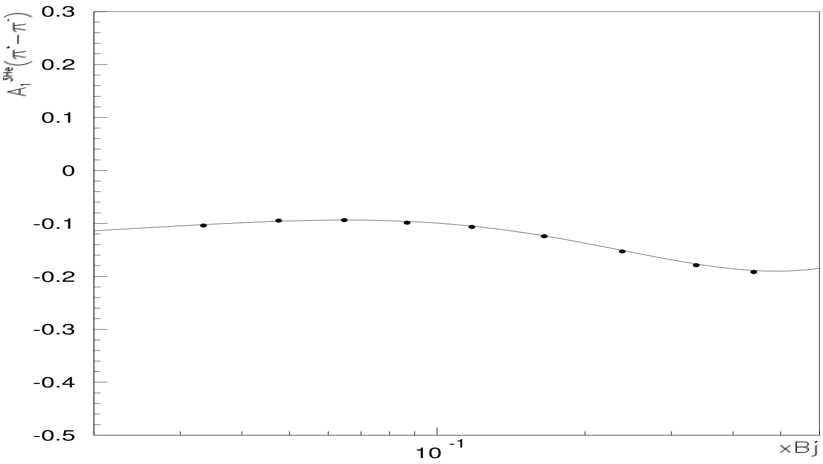

(b)

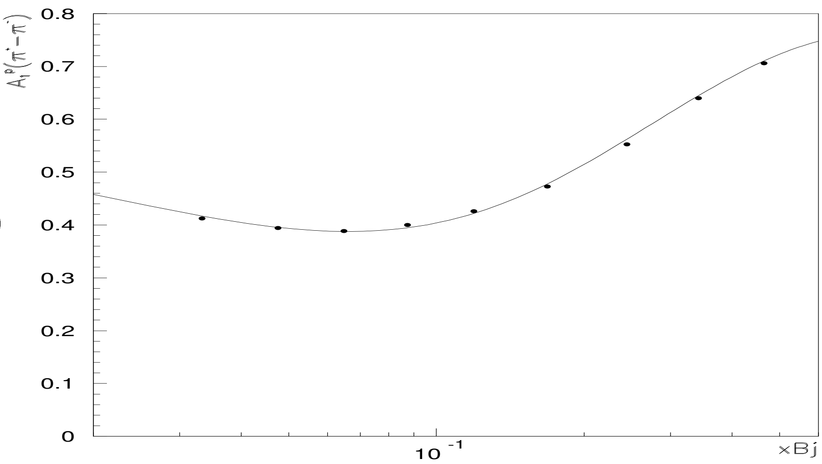

Figure 4.8: PEPSI simulation of the charge difference pion asymmetry for (a) a ^{3}He target and (b) a proton target. An artificial fragmentation scheme was used to produce this data. The lines show the theoretical prediction. In order to make easy comparisons, the x and y scales are kept the same as for other figures in this chapter.

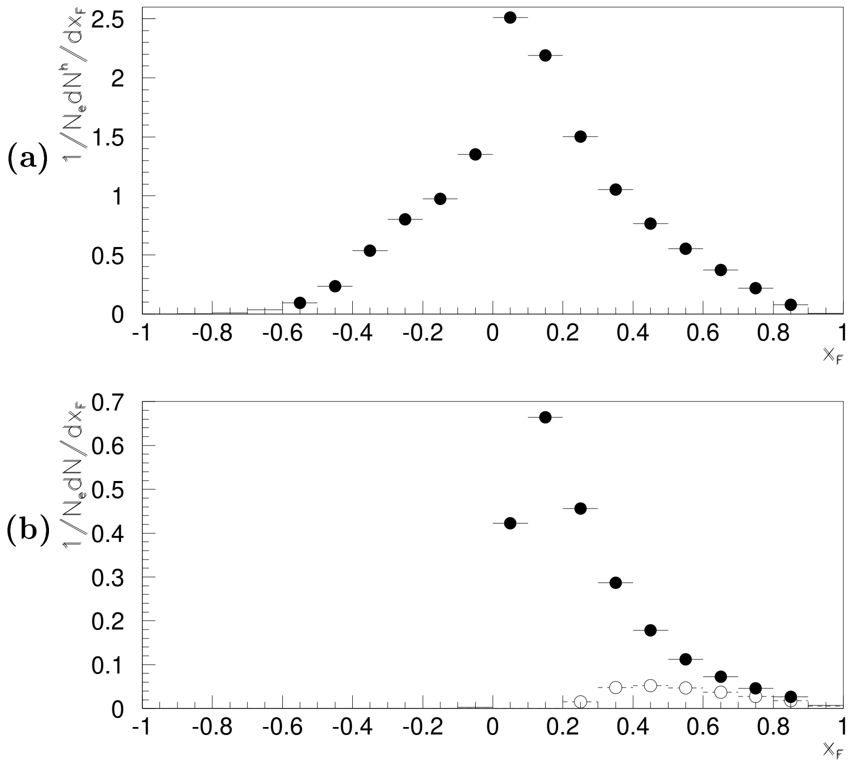

Figure 4.9: (a) shows the x_F distribution from an MC simulation of a detector with 4π acceptance. (b) shows the measured x_F distribution at HERMES, taken from 1995 data. The closed circles show the hadron distributions. As can be seen, the HERMES acceptance effectively cuts away most of the target contamination. The open cirles show the pion distribution. Due to the Čerenkov detector's momentum threshold for identified pions ($p > 6\ GeV$ for 1995 data), the pion sample has practically no contamination from target or central region fragments.

get respectively, using the same Gehrmann-Stirling parton distribution functions which were the input to the MC. The differences between the MC data and this line correspond to the distortions caused by the fragmentation process.

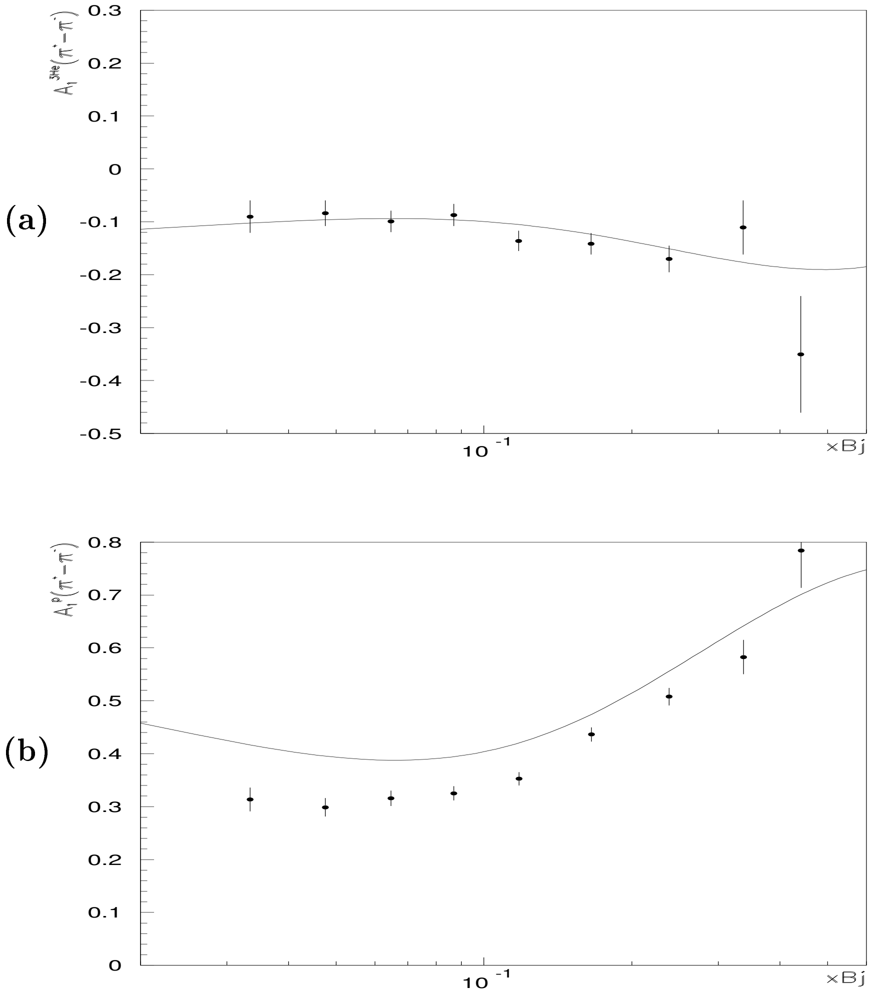

Figure 4.10: PEPSI simulation of the charge difference pion asymmetry for (a) an ideal ^{3}He target and (b) a proton target. The pions were required to have $x_F > 0.1$ and $z > 0.2$. The lines show the theory predictions for a ^{3}He and proton target respectively. The polarised and unpolarised parton distribution functions used in evaluating these predictions were the same as those used to produce the MC data itself.

In the real data set, particularly for the 1995 data, the yield of identified pions is poor. It is useful instead to use the hadron sample which has much better yields (approximately six times better for 1995 data), though it is inevitably contaminated by the presence of kaons and protons in addition to pions. Figure 4.11 shows the difference in the asymmetry for pions and for hadrons.

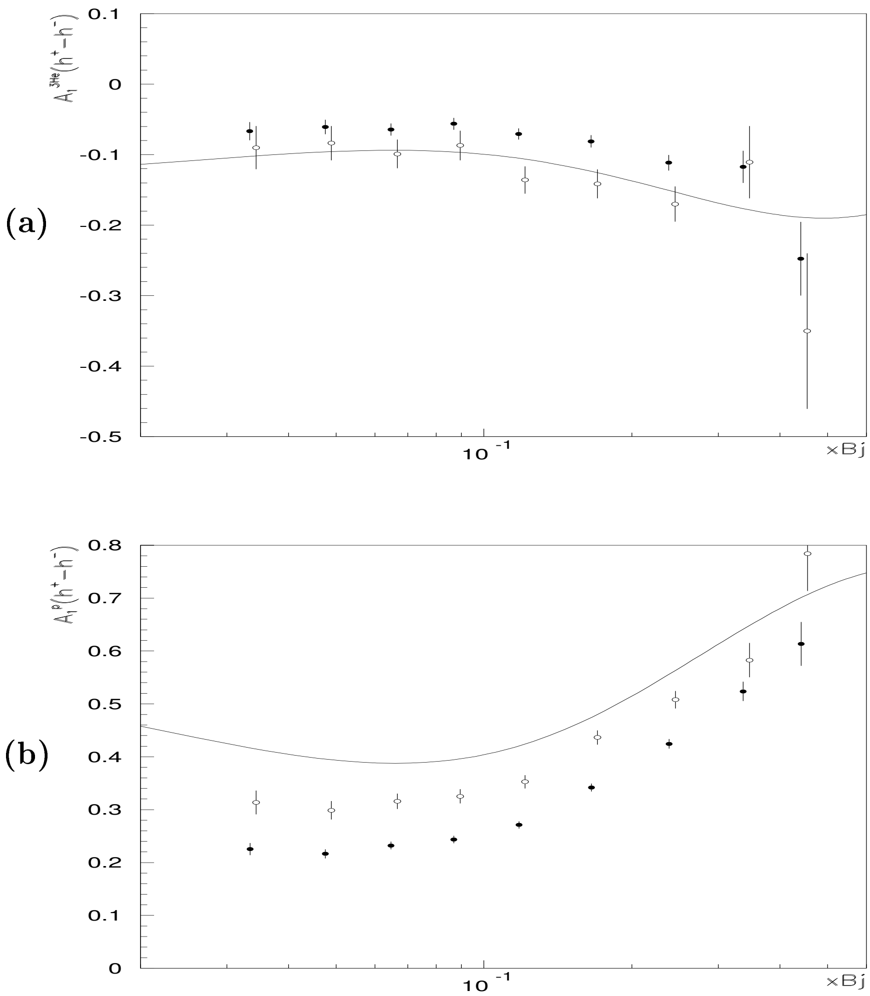

Figure 4.11: PEPSI simulation of the charge difference asymmetry for pions (open circles) and hadrons (closed circles) for (a) a ^{3}He target and (b) a proton target. For this data, the pion and hadrons were required to have $x_F > 0.1$ and $z > 0.2$. The lines show the theory expectation.

Figure 4.12 shows the effect of varying the minimum z and x_F cuts on the hadron sample. As the minimum z and x_F cuts become higher, the selected data sample contains less contamination from the target and central region and the resulting asymmetry gets closer to the theory line. This effect is not seen for the pion sample because the high effective momentum cut due to the Čerenkov threshold means that there is little target or central region contamination (effectively their average z and x_F is higher than that for the hadron sample).

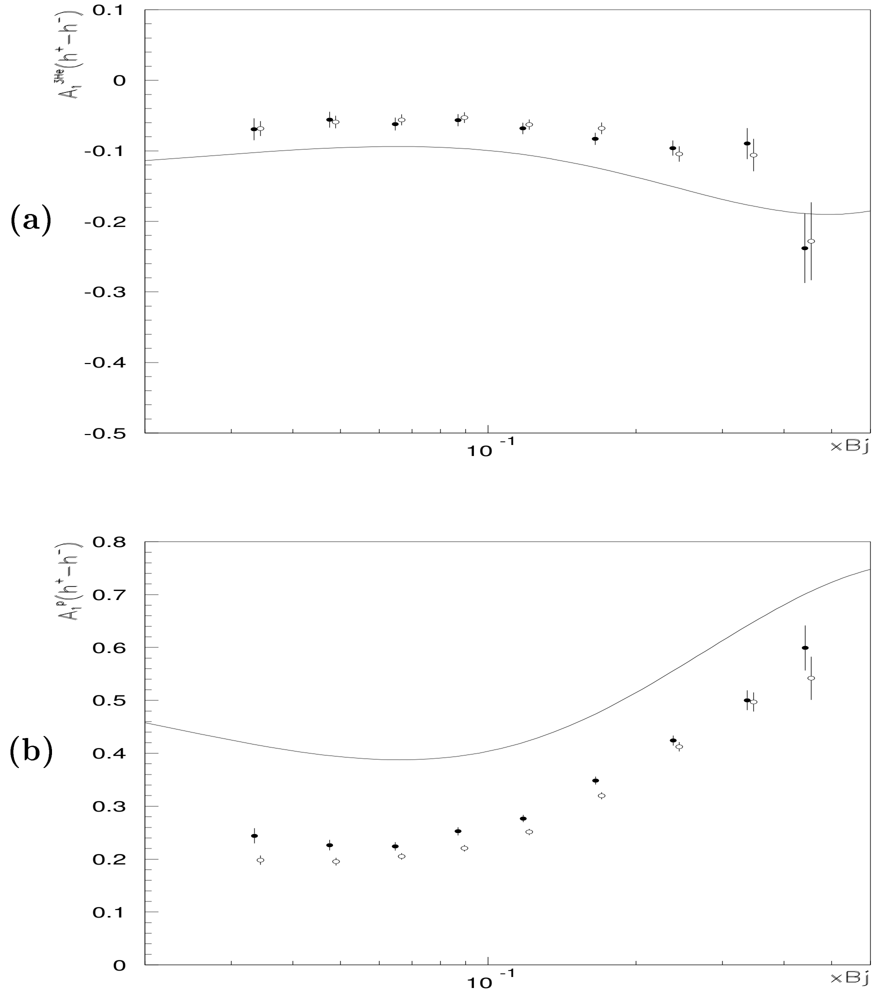

Figure 4.12: PEPSI simulation of the charge difference pion asymmetry for $z > 0.3$ and $x_F > 0.1$ (closed circles) and $z > 0.1$ and $x_F > 0.0$ (open circles) for (a) a ^{3}He target and (b) a proton target. The lines show the theory expectation.

In the asymmetries calculated so far, all hadrons in each DIS event have been selected, so long as they pass the z and x_F cuts. An additional selection method has been investigated to reduce the target region contamination. To increase the probability of the hadron coming from the struck quark, only the highest energy hadron in an event which passes the z and x_F cuts is counted. The comparison between the two methods is shown in figure 4.13. As can be seen, there is nothing to be gained from this additional cut, other than a loss in statistics. Once again this is due to the fact that generally only leading hadrons get into the HERMES acceptance.

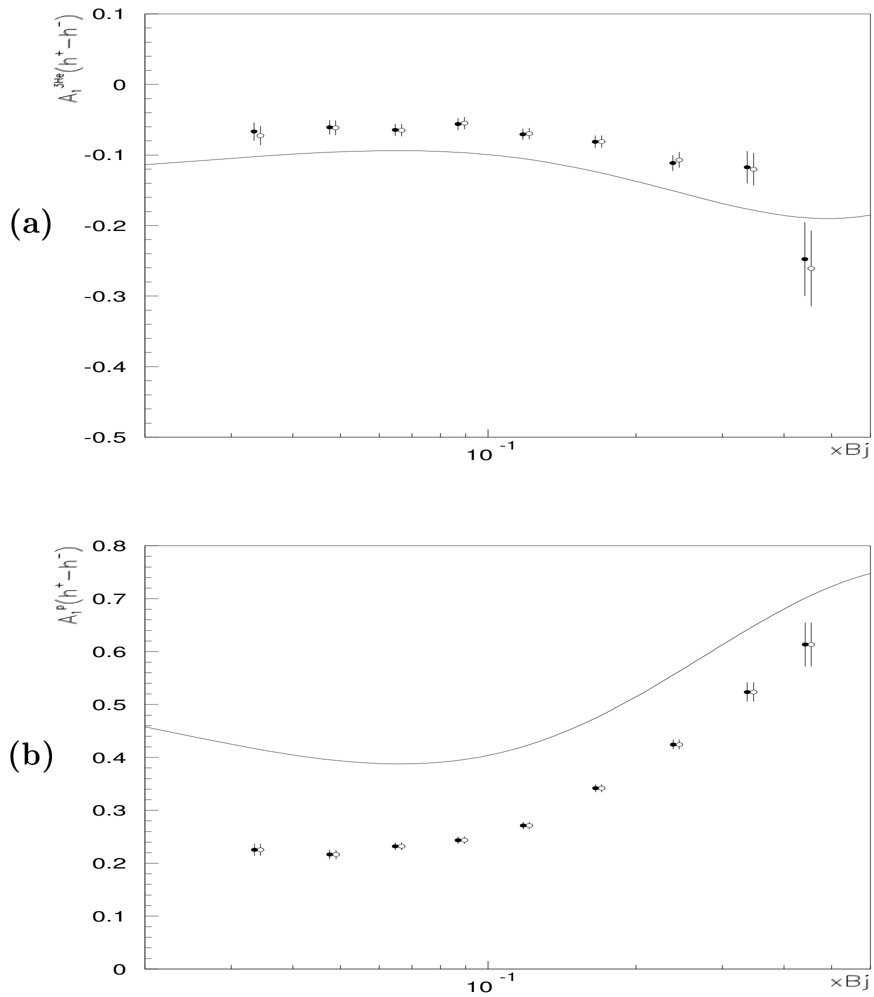

Figure 4.13: PEPSI simulation of the charge difference asymmetry for leading (closed circles) and all hadrons (open circles) for (a) a ^{3}He target and (b) a proton target. For this data, the hadrons were additionally required to have $x_F > 0.1$ and $z > 0.2$. The lines show the theory expectation.

Q^2 dependence

The asymmetry is calculated using just one bin in Q^2. However, to deal with the Q^2 dependence of the photon depolarisation factor more appropriately, a different way of calculating the asymmetry was investigated. The asymmetry was calculated separately in five Q^2 bins (1-2 GeV^2, 2-4 GeV^2, 4-6 GeV^2,6-10 GeV^2 and >10 GeV^2) and the final result made from the average of these five results. No significant differences were seen between using this method and the standard method of calculating the asymmetry for any of the MC hadron asymmetries.

4.3.2 Conclusions from simulation studies

It has been seen that the fragmentation process causes a dilution of the charge difference pion asymmetry from the theoretical prediction, or the case where the fragmentation process is artificially switched off. These dilutions can be seen more clearly for a proton target than for a ^{3}He target simply because the asymmetry is three times larger and thus the dilution effects are magnified.

The dilution is worse for the hadron sample than for the pion sample due to the presence of kaons and protons in the hadrons and also due to the fact that the hadron sample covers a larger range in momentum than the pion sample (due to the low Čerenkov momentum threshold cutoff for identified pions), and hence has more target and central region contamination. A kinematic cut of $x_F > 0.1$ and $z > 0.2$ has been seen to be adequate in minimising the contamination from target and central regions, given that the HERMES acceptance removes most of this contamination in any case.

Thus the MC has shown that the fragmentation process causes significant dilutions to the hadron spin asymmetries. In order to measure the partonic level quantities, namely Δu, Δd and $\Delta\overline{q}$, the hadronic level asymmetries must be corrected for these fragmentation effects. The MC fragmentation model has been tuned so that it describes the HERMES data reasonably well and thus can be used to make this correction.

Chapter 5

Event Selection

In this chapter the selection of events for analysis is described. This analysis has made use of the results from the HERMES inclusive analysis group which has produced a list of good data quality bursts for each year of data taking. Not all the inclusive group's cuts were applicable, but those implemented in this analysis are summarised here. Similarly, the particle identification scheme is common to all HERMES analysis, and it is summarised briefly here. The small differences that exist between the 1995 and 1996 analysis are discussed at the end of this chapter.

5.1 Data quality burst level selection

Data quality selection was performed at the fill, run and burst level (see section 3.4.2). After first level selection using the information in the experimental log books to eliminate fills and runs with obvious problems (such as unpolarised target running, parts of the spectrometer switched off or unreliable target or beam polarimetry) the following cuts were made at the burst level :

- **Target polarisation :** it was required that
  - the target was not switching polarisation state within the burst
  - either the target pumping cell polarimeter (PCP) or the target optical monitor (TOM) measured $30\,\% < P_T < 60\,\%$.

- **Beam polarisation :** for each fill a fit was made to the minute by minute readout to smooth the statistical fluctuations. Then it was required that

  – $40\,\% < P_B < 70\,\%$.

  Figure 5.1 shows the beam and target polarisation distributions for the year.

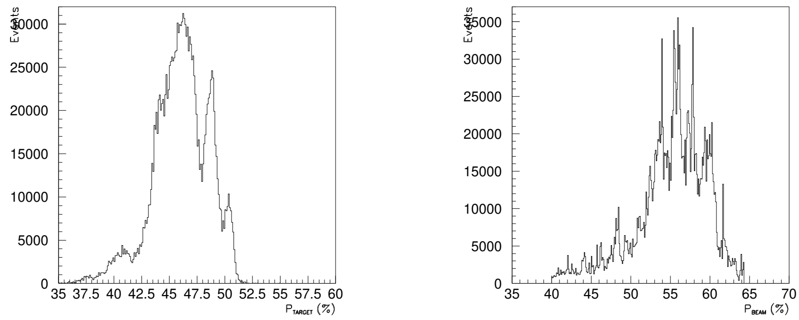

(a) **(b)**

Figure 5.1: The distributions of (a) the target polarisation and (b) the beam polarisation for all accepted events.

- **Data acquisition system (DAQ) :**

  – the first three bursts and last burst of each run were rejected as during these periods the DAQ was initialising or terminating the run.

  – cut on the live time $50\,\% < T_{live} < 100\,\%$. This distribution is shown in figure 5.2. The live time is defined as the number of triggers accepted by the DAQ system divided by the number of triggers generated.

  – cut on the burst length $9\,s < T_{burst} < 11\,s$.

- **Luminosity :** to cross check the luminosity detector's performance, its rate was compared to the product of the beam current and target density. It was required that :

  – the beam current (I) was within the range $8\,mA < I < 32\,mA$

  – the target density was within the range $0.85 \times 10^{15} < n < 1.4 \times 10^{15}$, where n is the density in nucleons/cm^2.

  – the luminosity monitor rate ($\dot{N}_{lumi}$) was within the range $40\,Hz < \dot{N}_{lumi} < 210\,Hz$. Figure 5.2 shows this distribution.

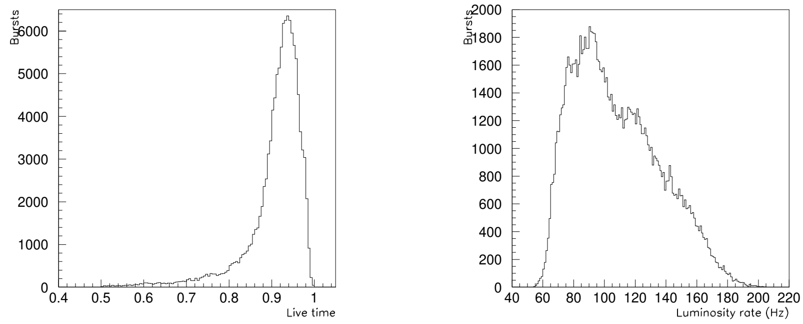

(a) **(b)**

Figure 5.2: (a) the DAQ live time and (b) the measured luminosity rate for all accepted bursts.

  - the ratio $\frac{\dot{N}_{lumi}}{nI}$ was within the range $5 \times 10^{-15} < \frac{\dot{N}_{lumi}}{nI} < 7.2 \times 10^{-15}$.

- **Detector trips :** to detect high voltage trips of the tracking chambers, the tracking efficiencies were calculated for each plane and affected bursts were rejected. This was also done for the Čerenkov and TRD, but at a run rather than burst level due to the fact that these detectors are less efficient and need more time to accumulate enough counts to perform the efficiency analysis. For the calorimeter and preshower, the gain monitoring system (GMS) was used to detect bad modules by comparing the nominal gains with the measured average gain. This was also done at run level to gain enough statistics to perform the analysis. Following these checks, it was required that

  - no trips were recorded for the tracking chambers in either the top or bottom detector. This differs from the inclusive group's analysis which could consider top and bottom detectors completely independently.
  - for particle identification, at least the calorimeter, preshower and Čerenkov detectors were fully functional.

- **Overall stability :** to avoid fills with many instabilities

  - at least 100 bursts in each spin state and each detector half were required for each fill. As well as indicating general instability, these fills with little data in them were rejected because the asymmetries are calculated per fill (to avoid time dependencies, as explained in section 7.3) and it is necessary to have enough statistics within each fill to do this.

- runs with only a small fraction of good bursts were rejected (> 40 % of good bursts were required within a run).
- if there were frequent changes from good to bad quality within a run, it was rejected (it was required that $\frac{n_{gaps}}{n_{bursts}} < 0.10$ where n_{gaps} is the number of gaps between each series of good bursts and n_{bursts} is the total number of bursts in the run).

5.2 Charge multiplicity study

The positive (negative) charge multiplicity per event, defined as the number of positively (negatively) charged particles in coincidence with a DIS positron, is a sensitive measure of data quality for semi-inclusive physics. The average positive and negative charge multiplicities per run were calculated and the error-weighted differences from the mean,χ_i, were calculated, where $\chi_i = \frac{x_i - \bar{x}}{\sigma_i}$, with x_i the multiplicity for a run i and σ_i its statistical error. $\bar{x}$ is the mean for all runs, found to be 0.223 for positive particles and 0.149 for negative particles. With this definition, a run with a χ_i of one represents a 1 σ difference from the mean of the distribution.

The χ_i distributions for positive and negative charge multiplicities for the whole running period are shown in figure 5.3. For the positive charge multiplicity the χ^2 per degree of freedom was found to be 0.83 and for negative 0.86. In figure 5.4 the distributions for one fill are shown and it can be seen that there is no fill dependence.

Using this data, runs were only accepted if both their positive and negative charge multiplicities were within 3σ of the means for the whole running period. The means were calculated separately for each spin state. 45 runs (consisting of 2251 bursts) are rejected by this cut, leaving a final total of 64 464 bursts in 1412 runs to be analysed.

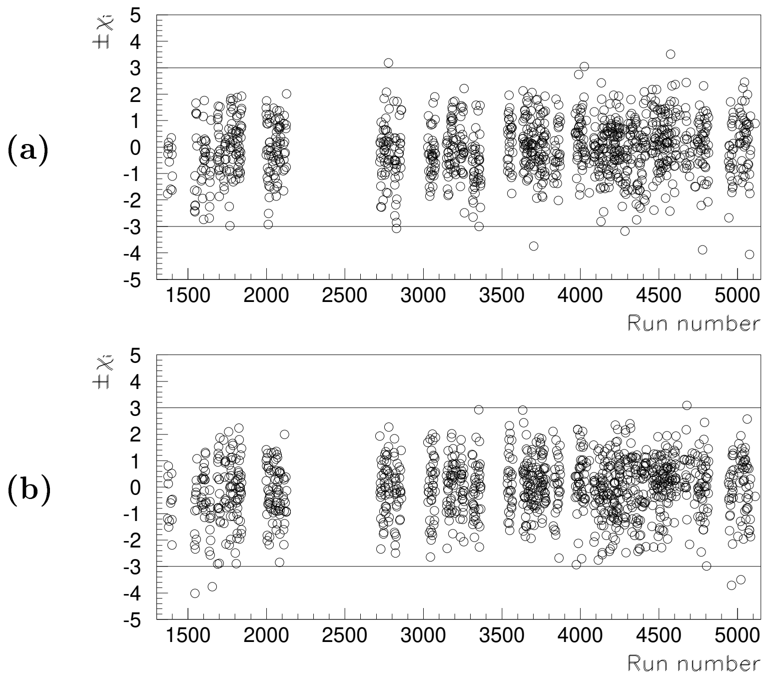

Figure 5.3: The weighted differences from the mean for (a) the positive and (b) negative charge multiplicities, where the means are calculated separately for each spin state. The distribution shown here is for one spin state. The lines are drawn at $\pm 3\sigma$ where the cut is made.

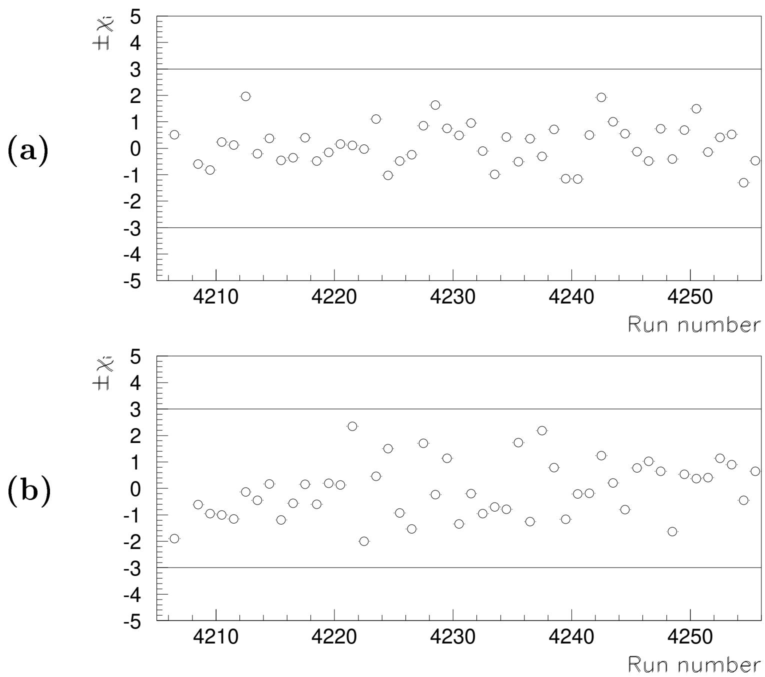

Figure 5.4: The weighted differences from the mean for (a) the positive and (b) the negative charge multiplicities for a typical fill. The χ^2 per degree of freedom is 0.65 for the positive charge multiplicity and 0.91 for the negative.

5.3 Particle Identification

A full description of the HERMES particle identification scheme can be found in [60]. Rather than simply using cuts on individual detector responses, it has been found that a "log likelihood" method is more efficient. This is summarised briefly here.

Each detector's response can be defined in terms of the conditional probability L^i_D that the response in detector D was caused by particle type i. These "parent distributions" are analytical expressions fitted to test beam measurements with the separate detector modules.

A quantity known as PID3 is used to combine the information from the calorimeter, preshower and Čerenkov detectors. It is defined as

$$\text{PID3} = log_{10}\left(\frac{L^e_{cal}L^e_{pre}L^e_{cer}}{L^h_{cal}L^h_{pre}L^h_{cer}}\right). \tag{5.1}$$

When used in conjunction with the TRD, good separation can be achieved between electrons/positrons and hadrons, as shown in figure 5.5. The TRD was not implemented into the likelihood scheme because of initial problems with its calibration. Also, it was the most unstable detector during the 1995 run, and it was useful to decouple it from the main PID scheme to enable data to be used even when the TRD was not working.

Different cuts were used depending on whether the TRD was functioning properly or not. When all four PID detectors were working, the PID value was defined as

$$\text{PID} = \text{PID3} + 0.31 \times \text{TRD} - 5.48. \tag{5.2}$$

If either half of the TRD was not working, then the PID value was taken to be

$$PID = PID3. \tag{5.3}$$

Then the following PID cuts were used

- PID $>$ 2.0 for electrons/positrons.
- PID $<$ -1.0 for hadrons.

This represents a linear "valley cut" in the PID3-TRD plane (see figure 5.5) when all four PID detectors were functioning or in the PID3 distribution alone for the case when the TRD was not functioning.

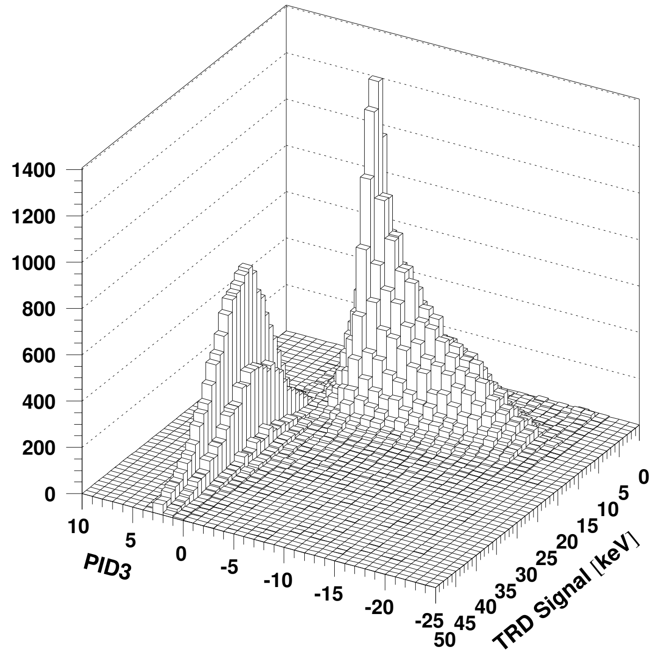

Figure 5.5: The distribution for PID3 versus the TRD response for all particles. This plot has been created using HERMES 1995 data. A clear separation is seen between positrons/electrons (PID3 > 0) and hadrons (PID3 < 0), even if the TRD plane is not used to enhance this separation.

The average contamination due to particle misidentification in both the positron and hadron samples was found to be less than 1% with efficiency greater than 98% [60, 61].

5.4 Track selection

Hadrons counted in the asymmetries were required to be coincident with a DIS positron, defined as

- the highest energy particle in the event satisfying the electron/positron PID signature with
  - $Q^2 > 1.0\, GeV^2$, to be within the DIS kinematic region,

– $W^2 > 4.0\,GeV^2$, to avoid the resonance region and

– $y < 0.85$ to ensure the radiative corrections are small.

The distribution of accepted events in the Q^2-ν kinematic plane is shown in figure 5.6.

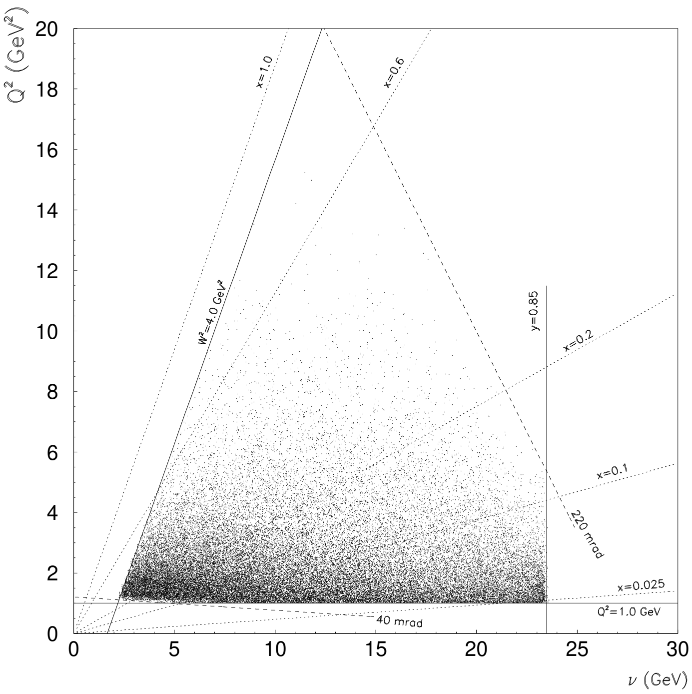

Figure 5.6: The distribution of events selected for the analysis in the Q^2-ν kinematic plane. The dashed lines show the limits of the acceptance. The solid lines show the applied cuts. The dotted lines show the contours of x.

Positron tracks were required to have their vertices originating from the target cell by requiring

- $z_{vertex} < \pm 20$ cm ; $r_{vertex} < 0.75$ cm

where z_{vertex} is the interaction point's extrapolated distance along the z axis and r_{vertex} its perpendicular distance from the z axis. Figure 5.7 shows the z_{vertex} and r_{vertex} distributions for all tracks before these cuts are made.

To ensure that all the energy of the positron is detected, a fiducial volume cut at the calorimeter was made on all tracks

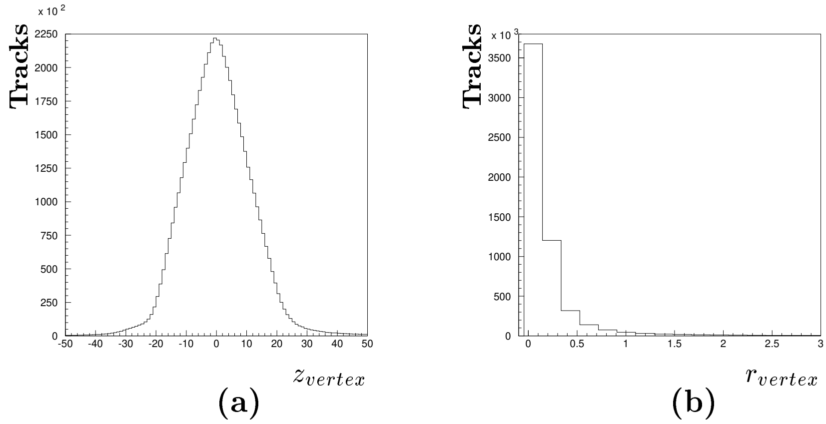

Figure 5.7: (a) the z_{vertex} and (b) the r_{vertex} distributions for all tracks from DIS events before the vertex cuts are made.

- $| x | < 175\, cm\,;\; | y | > 30\, cm.$

An acceptance cut for all tracks was made to avoid the septum plate and to avoid the edges of the detector where the acceptance cannot be easily modelled by the Monte Carlo,

- $0.040 <| \theta_y |< 0.140$
- $| \theta_x |< 0.180.$

Figure 5.8 shows the distribution of all tracks in the θ_x - θ_y plane after this cut.

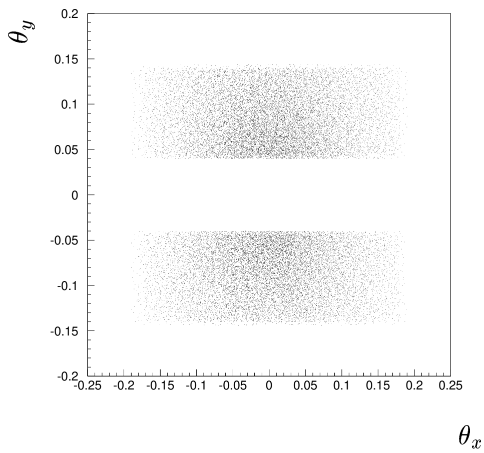

Figure 5.8: The θ_x - θ_y distribution for the hadron sample, after all cuts have been made.

For a track to count as a hadron it was required that it was a

- charged track with hadron PID signature.

For a hadron to be identified as a pion it was additionally required that

- 6.0 GeV $<$ p $<$ 21.0 GeV and $n_{Ce} > 0.25$,

where n_{Ce} is the average number of photoelectrons detected in the Čerenkov counter.

To accept only hadrons with a high probability of coming from the current region (see chapter 4), each hadron was required to have

- $x_F > 0.1$,
- $z > 0.2.$ and
- $W^2 > 10.0$ GeV^2

5.5 Differences for 1996 data

5.5.1 Data Quality

The main differences between the 1995 and 1996 analysis are summarised in this section.

- **Target polarisation :** cut on raw target polarisation measured by Breit-Rabi Polarimeter : $80\,\% < P_T < 99\,\%$.
- **Beam polarisation :** $30\,\% < P_T < 80\,\%$.
- **Data Acquisition system :**
  - cut on the live time $80\,\% < T_{live} < 100\,\%$. This higher cut reflects the lower data taking load on the DAQ in 1996 due to the much less dense target being used.

  - cut on the burst length $0\,s < T_{burst} < 11\,s$. This looser cut is required because the target polarisation was changed every 40–70 seconds in 1996. Thus rather than throwing away each burst where a target flip occurs (as was done in 1995), the burst was split into two sections and the section affected by the spin flip was thrown out, leaving a short burst of good data.

- **Luminosity :**
  - the beam current was within the range $8\,mA < I < 50\,mA$. This higher upper limit reflects the higher beam currents available in 1996 due to better performance of the accelerator.
  - the luminosity monitor rate was within the range $5\,Hz < \dot{N}_{lumi} < 60\,Hz$. This lower cut is due to the lower target density in 1996 compared to 1995.
  - unlike the 1995 data, there is no cut on the target density, as this could not be measured accurately with the 1996 target apparatus.

- **Detector trips :** detection was aided by data from the CAEN high voltage system which was not used in 1995. This recorded changes in high voltage over time for each wire chamber.

5.5.2 Particle Identification

The 1996 PID scheme was very similar to 1995. The exception is that the TRD was included into the likelihood scheme. Thus the PID variable used was

$$\mathrm{PID} = log_{10}\left(\frac{L^e_{cal}L^e_{pre}L^e_{cer}L^e_{TRD}}{L^h_{cal}L^h_{pre}L^h_{cer}L^h_{TRD}}\right). \tag{5.4}$$

Then the following PID cuts were used

- PID $>$ 0. for electrons/positrons.
- PID $<$ -2.0 for hadrons.

Just as for the 1995 data, the contamination of both the positron sample and the hadron sample is negligible.

5.5.3 Track Selection

Track selection for the 1996 analysis was identical to that used for the 1995 analysis.

5.6 Background Corrections

Charge symmetric backgrounds

Photoproduction is potentially a large source of background to the DIS process in *ep* scattering. While for this process the positron will usually be scattered through a small angle and will not be detected, the production of π^0 's and the subsequent decay through pair production to e^+e^- pairs, may lead to misidentified DIS positron events. Additionally the process forms a background source of hadrons which could potentially be misidentified as DIS positrons through false particle identification. While this can equally well happen for DIS processes, Monte Carlo studies have shown that the hadrons produced from photoproduction have a mean energy of around 7 GeV [62], higher than the mean energy of hadrons from DIS processes, thus increasing the likelihood of being misidentified as DIS positrons.

A subtraction is made to account for the pair production background. If an electron passes all the cuts for a DIS positron (other than that of charge), then one DIS positron event, with identical kinematics as the electron event, is subtracted. Assuming equal probabilities of identifying positrons as electrons from pair production, this procedure will remove from the DIS sample the hidden positrons originating from pair production.

A similar procedure is used to account for hadrons being misidentified as DIS positrons. Assuming that it is equally probable that a hadron is misidentified as an electron as a positron, if an electron passes all the cuts for a DIS positron (other than the charge), then one event, with the same kinematics as the electron, is subtracted from the DIS positron sample. This subtraction is indistinguishable from the pair production background. In addition however, for each hadron in coincidence with this electron, a hadron of opposite charge is subtracted from the count rate of hadrons in coincidence with a DIS positron. For example if a $\pi^+\pi^-$

is produced in an event, and the π^- is misidentified as an electron which passes the DIS cuts, then an e^+ and a π^- is subtracted.

Hence this background is subtracted for all charge symmmetric processes (or at least all processes which result in charge symmetric processes being detected – for example the photoproduction process of diffractive scattering can produce the charge asymmetric $\pi^+\pi^-p^+$, however the proton generally is not in the acceptance, leaving a charge symmetric background).

In total 21 000 background events in the 1995 data has been accounted for, representing about 1% of the total number of events analysed.

ρ production

Pions which come from the decay of ρ meson particles are another source of background. However, in the 1995 data sample, the total number of ρ mesons which could be reconstructed from events with a $\pi^+\pi^-$ pair in the acceptance and a DIS positron in coincidence, was found to be only 1 600. While there will be additional ρ events with only a single pion in the acceptance, this number is expected to be correspondingly small.

Chapter 6

Extraction of the Spin Asymmetries

6.1 Calculation of the Asymmetries

The spin asymmetries measured from the data have to be corrected for the beam and target polarisations. In addition the count rates have to be normalised by the luminosity delivered to each spin state, which is the product of the luminosity monitor rate and the data acquisition live time.

If in a burst i, the total count rate for a particle h for each spin state ($+$ or $-$) is $N^h_{i\pm}$, the total integrated luminosity is $L_{i\pm}$, the data acquisition live time is T_{DAQi}, then the general formula for the measured spin asymmetry can be written as

$$A^h(x) = \frac{N^h_-(x)L_+ - N^h_+(x)L_-}{N^h_-(x)D^h_+(x,Q^2)L_+P_+ + N^h_+(x)D^h_-(x,Q^2)L_-P_-} \tag{6.1}$$

where

$N^h_\pm = \sum_i N^h_{i\pm}$,

$L_\pm = \sum_i L_{i\pm} * T_{DAQi}$,

and the summations are over all bursts in the data. $P_\pm$ is the averaged polarisation correction factor (the product of the measured beam and target polarisations) and $D^h_\pm(x,Q^2)$ is the averaged photon depolarisation factor. Both these latter two quantities are averaged per event for each spin state.

The asymmetries were calculated for each fill and then the results for each fill averaged to give the final values for the asymmetries (see section 7.3).

The statistical error calculation for the asymmetries is shown in Appendix A.

6.2 Particle Yields

6.2.1 1995 (^{3}He target) data

After all cuts, there remain

- 2157652 e^+
- 284249 h^+
- 177907 h^-
- 53088 π^+
- 37803 π^-

The average polarisation correction factor ($P_{Beam} * P_{Target}$) for this data was 0.25.

6.2.2 1996 (p target) data

After all cuts, there remain

- 706705 e^+
- 87778 h^+
- 49658 h^-
- 35774 π^+
- 24580 π^-

The average polarisation correction factor ($P_{Beam} * P_{Target}$) for this data was 0.42.

6.3 Asymmetry results

6.3.1 1995 (^{3}He target) data

Figures 6.1 and 6.2 show the hadron and pion asymmetries for a ^{3}He target. Figure 6.3 shows the inclusive positron asymmetry. These results are summarised in tables 6.2, 6.3 and 6.6.

The x binning used for each asymmetry is shown in table 6.1.

Bin number	x bin range
1	0.023-0.040
2	0.040-0.055
3	0.055-0.075
4	0.075-0.100
5	0.100-0.140
6	0.140-0.200
7	0.200-0.300
8	0.300-0.400
9	0.400-0.600

Table 6.1: The binning in x used throughout the analysis.

x bin	$< x >$	$< Q^2 >$	$A^{h^+-h^-}$	$\delta A^{h^+-h^-}$	A^{h^+}	δA^{h^+}	A^{h^-}	δA^{h^-}
1	0.033	1.21	-0.012	0.157	-0.051	0.032	-0.079	0.037
2	0.048	1.45	-0.108	0.135	-0.011	0.033	0.021	0.039
3	0.065	1.75	-0.055	0.125	-0.030	0.034	-0.021	0.042
4	0.087	2.14	-0.107	0.128	-0.035	0.039	0.027	0.049
5	0.118	2.71	-0.076	0.122	-0.024	0.041	0.009	0.053
6	0.165	3.68	0.052	0.134	0.006	0.049	-0.022	0.066
7	0.238	5.18	-0.361	0.166	-0.155	0.067	0.064	0.092
8	0.337	7.21	-0.055	0.339	-0.092	0.138	-0.229	0.199
9	0.447	9.81	0.248	1.063	-0.110	0.289	0.308	0.648

Table 6.2: Semi-inclusive hadron asymmetries for a ^{3}He target.

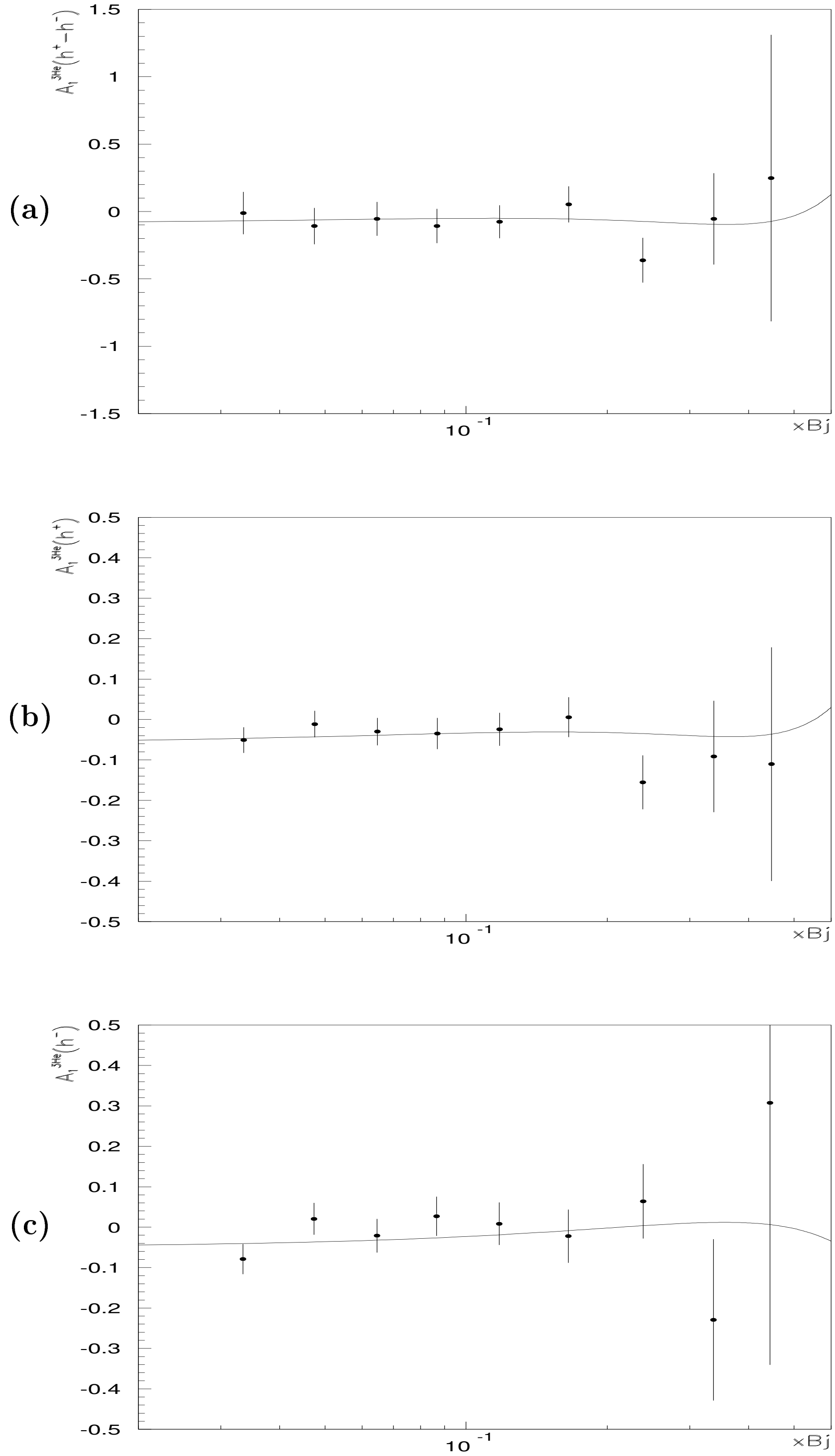

Figure 6.1: The hadron asymmetries on ^{3}He: (a) charge difference (b) h^+ (c) h^-. The lines drawn are fits to a MC simulation of the hadron asymmetries generated using the GRVOG parameterisation.

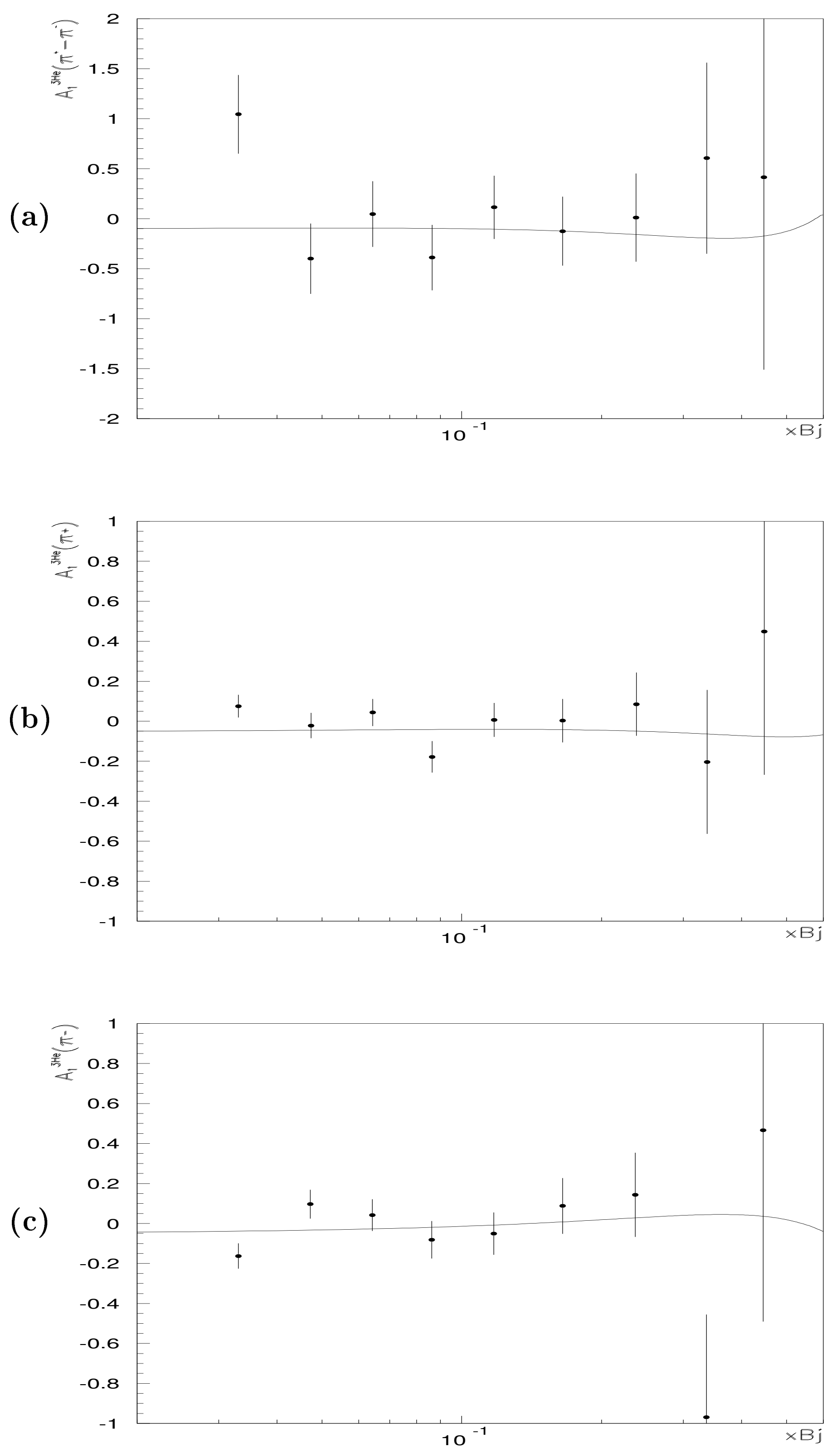

Figure 6.2: The pion asymmetries on ^{3}He: (a) charge difference (b) π^+ (c) π^-. The lines drawn are fits to a MC simulation of the pion asymmetries generated using the GRVOG parameterisation.

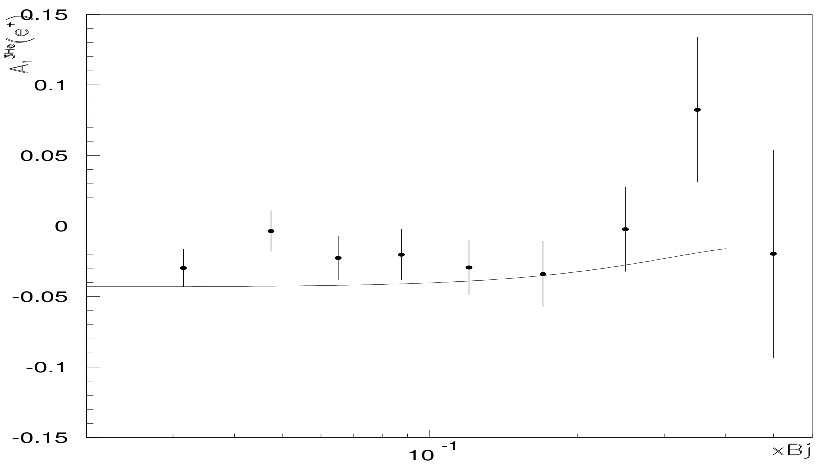

Figure 6.3: The inclusive positron asymmetry. The line drawn is a fit to a MC simulation of the inclusive positron asymmetry generated using the GRVOG parameterisation.

x bin	$< x >$	$< Q^2 >$	$A^{\pi^+-\pi^-}$	$\delta A^{\pi^+-\pi^-}$	A^{π^+}	δA^{π^+}	A^{π^-}	δA^{π^-}
1	0.033	1.211	1.044	0.394	0.075	0.057	-0.163	0.063
2	0.047	1.500	-0.400	0.353	-0.022	0.063	0.097	0.072
3	0.064	1.869	0.047	0.329	0.044	0.068	0.042	0.079
4	0.086	2.369	-0.389	0.328	-0.178	0.079	-0.082	0.094
5	0.118	3.100	0.115	0.316	0.007	0.085	-0.051	0.106
6	0.165	4.206	-0.125	0.345	0.003	0.109	0.088	0.140
7	0.239	5.867	0.011	0.441	0.085	0.158	0.144	0.210
8	0.337	8.046	0.606	0.956	-0.204	0.360	-0.969	0.514
9	0.451	10.70	0.414	1.924	0.449	0.717	0.466	0.957

Table 6.3: Semi-inclusive pion asymmetries for a ^{3}He target.

6.3.2 1996 (p target) data

Figures 6.4 and 6.5 show the hadron and pion asymmetries for a proton target. Figure 6.6 shows the inclusive positron asymmetry. These results are summarised in tables 6.4, 6.5 and 6.6.

x bin	$< x >$	$< Q^2 >$	$A^{h^+-h^-}$	$\delta A^{h^+-h^-}$	A^{h^+}	δA^{h^+}	A^{h^-}	δA^{h^-}
1	0.033	1.20	0.231	0.138	0.133	0.037	0.082	0.046
2	0.048	1.44	0.105	0.125	0.099	0.037	0.094	0.047
3	0.065	1.74	0.183	0.123	0.122	0.038	0.080	0.049
4	0.087	2.13	0.163	0.120	0.220	0.043	0.261	0.057
5	0.118	2.71	0.256	0.116	0.260	0.045	0.260	0.061
6	0.166	3.66	0.225	0.120	0.282	0.053	0.335	0.076
7	0.239	5.19	0.765	0.151	0.553	0.069	0.289	0.102
8	0.338	7.27	0.211	0.286	0.305	0.137	0.415	0.203
9	0.450	9.90	1.317	0.555	0.976	0.266	0.526	0.422

Table 6.4: Semi-inclusive hadron asymmetries for a proton target.

x bin	$< x >$	$< Q^2 >$	$A^{\pi^+-\pi^-}$	$\delta A^{\pi^+-\pi^-}$	A^{π^+}	δA^{π^+}	A^{π^-}	δA^{π^-}
1	0.033	1.211	0.391	0.248	0.152	0.047	0.072	0.055
2	0.047	1.500	0.258	0.257	0.103	0.051	0.048	0.059
3	0.064	1.870	0.236	0.248	0.122	0.054	0.076	0.063
4	0.086	2.369	0.462	0.225	0.300	0.061	0.213	0.076
5	0.118	3.100	0.203	0.231	0.208	0.066	0.212	0.083
6	0.165	4.206	0.335	0.236	0.298	0.081	0.265	0.105
7	0.239	5.867	0.804	0.307	0.552	0.111	0.344	0.150
8	0.337	8.046	0.705	0.697	0.479	0.234	0.310	0.307
9	0.451	10.70	1.023	1.196	1.349	0.484	1.743	0.695

Table 6.5: Semi-inclusive pion asymmetries for a proton target.

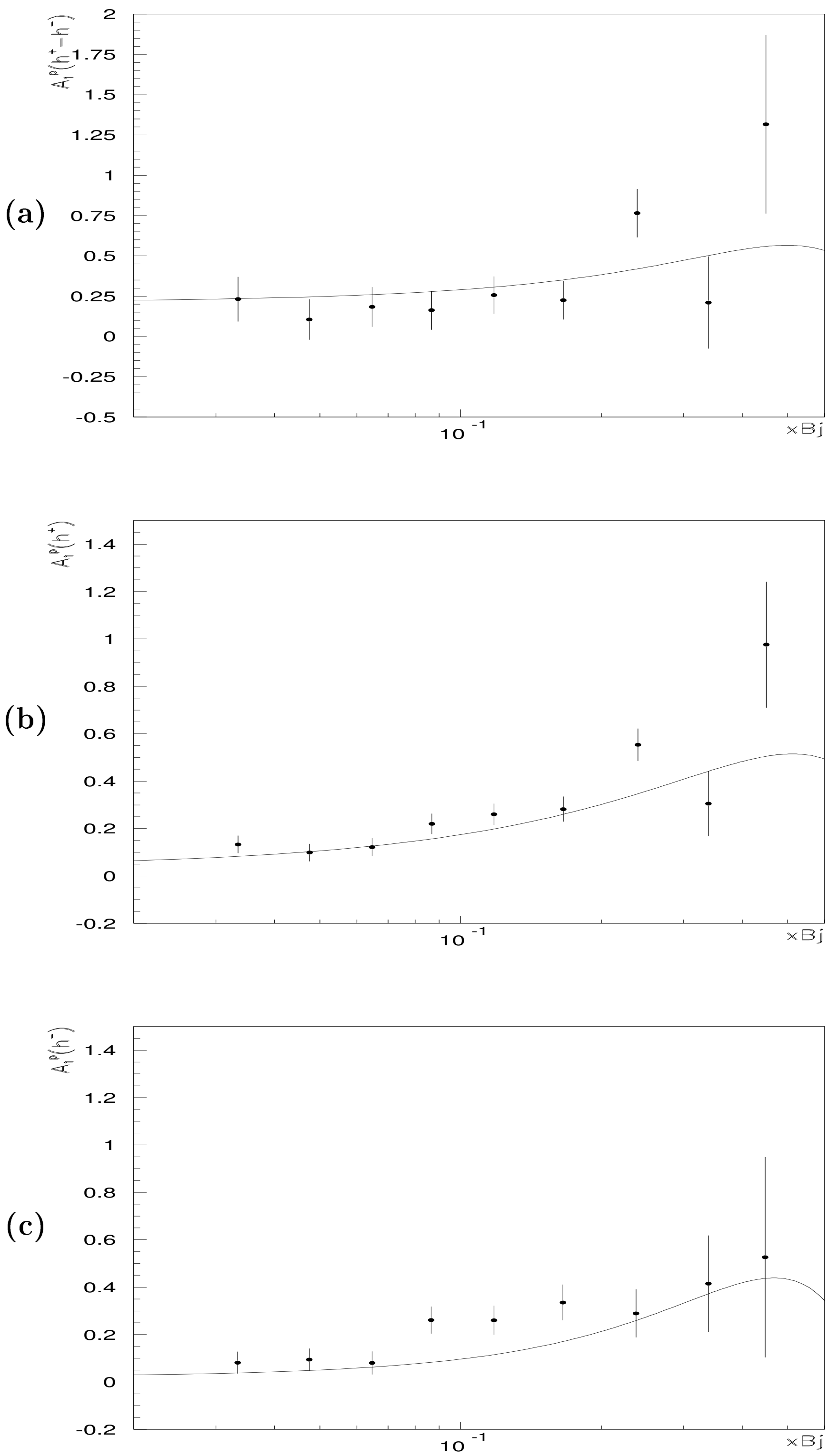

Figure 6.4: The hadron asymmetries for a proton target: (a) charge difference (b) h^+ (c) h^-. The lines drawn are fits to a MC simulation of the hadron asymmetries generated using the GRVOG parameterisation.

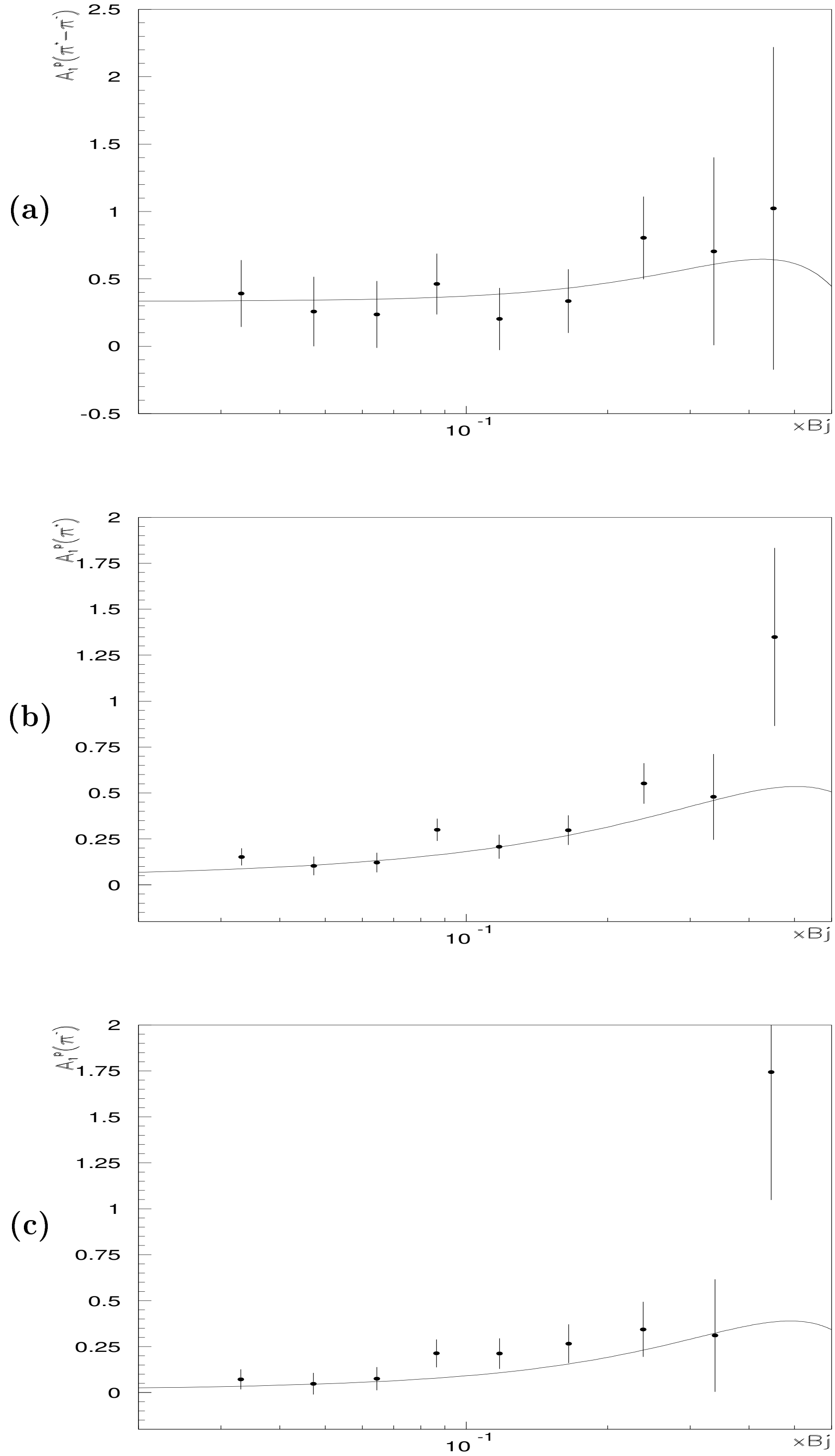

Figure 6.5: The pion asymmetries for a proton target: (a) charge difference (b) π^+ (c) π^-. The lines drawn are fits to a MC simulation of the pion asymmetries generated using the GRVOG parameterisation.

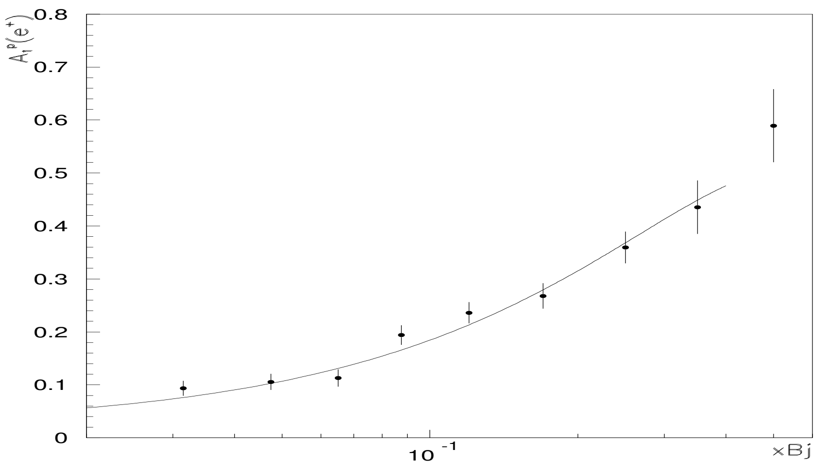

Figure 6.6: The inclusive positron asymmetry for a proton target. The line drawn is a fit to a MC simulation of the inclusive positron asymmetry generated using the GRVOG parameterisation.

x bin	$A^{e^+}_{^3He}$	$\delta A^{e^+}_{^3He}$	$A^{e^+}_p$	$\delta A^{e^+}_p$
1	-.0298	.01336	.0934	.0141
2	-.0035	.01445	.1055	.0152
3	-.0227	.01548	.1130	.0164
4	-.0204	.01800	.1941	.0187
5	-.0295	.01943	.2362	.0200
6	-.0341	.02344	.2679	.0241
7	-.0024	.02991	.3593	.0300
8	.0823	.05144	.4354	.0506
9	-.0197	.07371	.5893	.0690

Table 6.6: Inclusive positron asymmetries for ^{3}He and proton targets.

Chapter 7

Systematic Uncertainties on the Extraction of the Asymmetries

The systematic studies carried out on the semi-inclusive asymmetries for the 1995 data set are reported here.

7.1 Comparison of the Inclusive and Semi-Inclusive Asymmetries

As the asymmetry in the inclusive channel is built up from exclusive final states containing hadrons, the semi-inclusive *total* hadron asymmetry (i.e. $A^{h^{+}+h^{-}}$) should be the same as the inclusive asymmetry. As seen in Figure 7.1, good agreement is seen between the two asymmetries.

7.2 Hadron kinematic cuts

Figure 7.2 shows the hadron asymmetries for two different values of z and x_F cut. The two sets of asymmetries show no significant differences.

The same study for the pion asymmetries does not show any differences due to the pions' higher average z and x_F caused by the Čerenkov detector's momentum threshold of 6.0 GeV for pion identification.

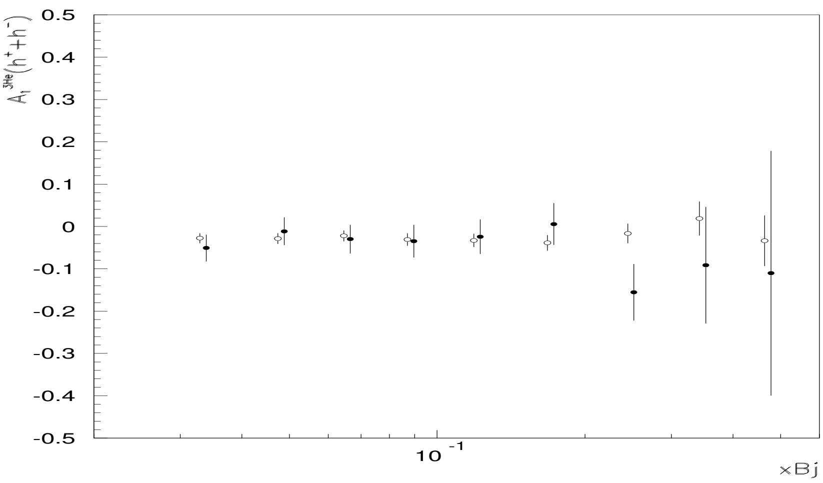

Figure 7.1: The asymmetry made for $h^+ + h^-$ (closed circles) compared to the official HERMES inclusive A_1 result [63] (open circles).

7.3 Summing versus Averaging

The simple formula for an asymmetry in a count rate measured over a certain time period can be expressed as

$$A_1 = \frac{\epsilon_1 N_1^+ - \epsilon_1 N_1^-}{\epsilon_1 N_1^+ + \epsilon_1 N_1^-}, \tag{7.1}$$

where $N^{\pm}$ are the count rates for the + and − spin states and ϵ_1 is some counting efficiency, assumed to be constant for each spin state over the time period. This efficiency could represent the overall detector efficiency, the trigger efficiency or whatever other possible cause of a systematic effect on the count rates. Provided it is constant over the time period, this efficiency will cancel out in the asymmetry. A fill is a natural time period to use – it is most likely that the efficiency is constant over the whole fill whereas this is less likely over different fills.

If all the time periods for the entire data period are added together, one gets

$$A = \frac{(\epsilon_1 N_1^+ + \epsilon_2 N_2^+ + ...) - (\epsilon_1 N_1^- + \epsilon_2 N_2^- + ...)}{(\epsilon_1 N_1^+ + \epsilon_2 N_2^+ + ...) + (\epsilon_1 N_1^- + \epsilon_2 N_2^- + ...)} \tag{7.2}$$

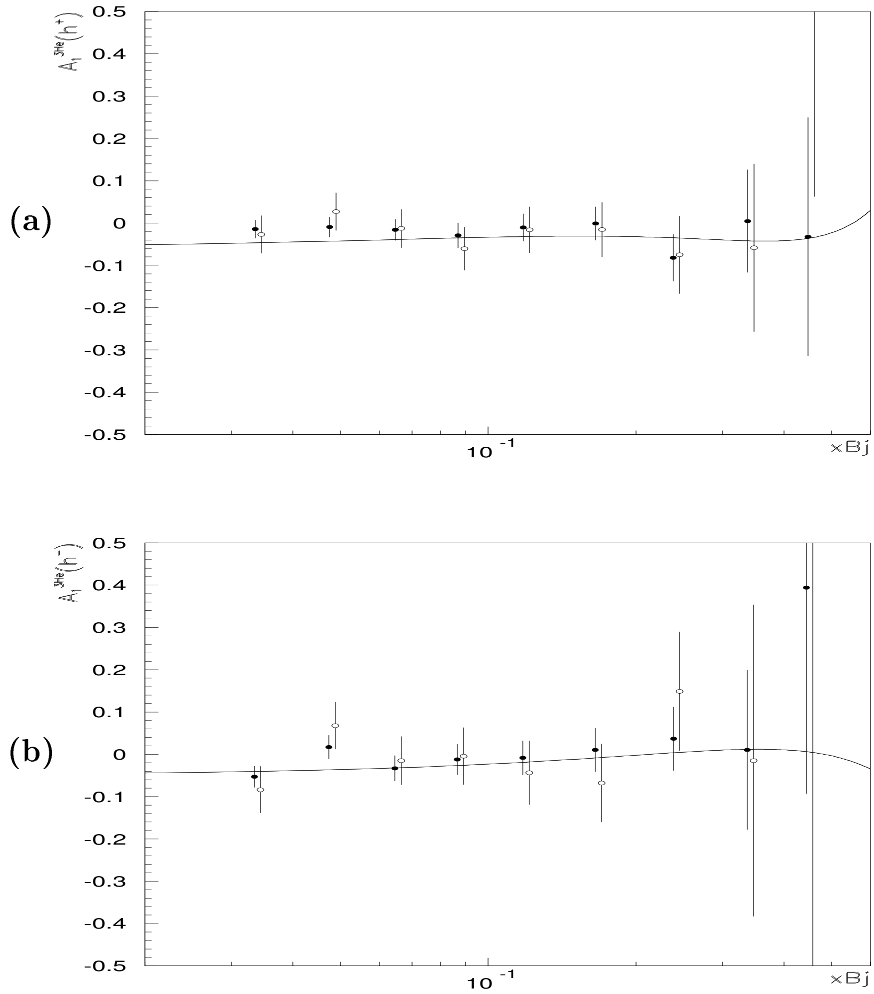

Figure 7.2: The hadron asymmetries for two different kinematic cuts. A cut on the hadron sample of $x_F > 0.0$ (closed circles) is compared to a cut of $x_F > 0.1$ and $z > 0.3$ (open circles) for (a) the h^+ asymmetry (b) the h^- asymmetry. The lines drawn are a fit to MC data generated using the Gehrmann-Stirling polarised parton parameterisation.

and there is no cancellation of the systematic effects on the count rates. Thus by making asymmetries per fill, the systematic error is reduced.

The comparison of summing all the data up over the year and then making the asymmetry with making the asymmetries on a fill by fill basis and then averaging is shown in figure 7.3. No significant differences are seen between the two sets of asymmetries, showing that any systematic changes between fills is small.

(a)

(b)

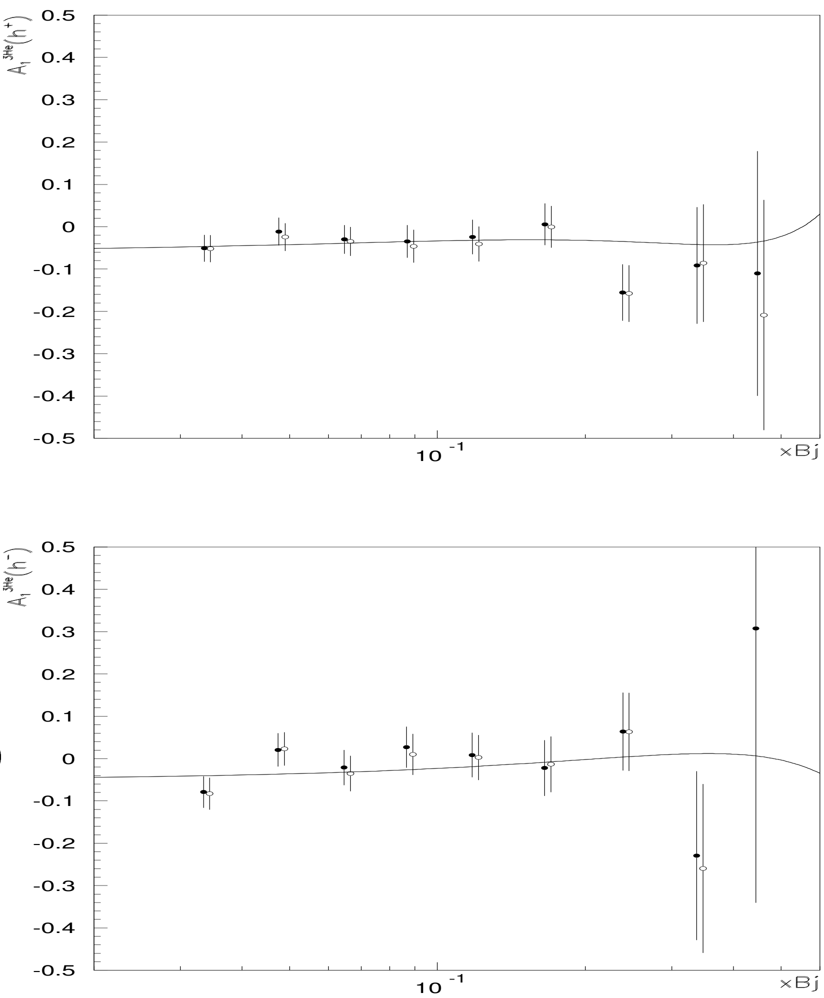

Figure 7.3: The hadron asymmetries calculated by summing all the data and then calculating the asymmetry (open circles) or by calculating the asymmetry for each fill and then averaging the results (closed circles). (a) h^+ asymmetry (b) h^- asymmetry.

7.4 Stability over time

To check for any time dependency of the asymmetries, the asymmetry per fill, averaged over all x bins, was calculated and its time dependence studied. The error-weighted differences from the mean,χ_i, were calculated, where $\chi_i = \frac{A_i - \bar{A}}{\sigma_i}$, with A_i the asymmetry for fill i, σ_i its statistical error and $\bar{A}$ the average asymmetry for all fills (shown in table 7.1). Figure 7.4 shows the results plotted against fill number. Normal χ^2 values were found, 0.83 for the charge difference asymmetry, 1.12 for the positive hadron asymmetry and 1.14 for the negative hadron asymmetry. It can be concluded therefore that no time dependency of the asymmetries is observed.

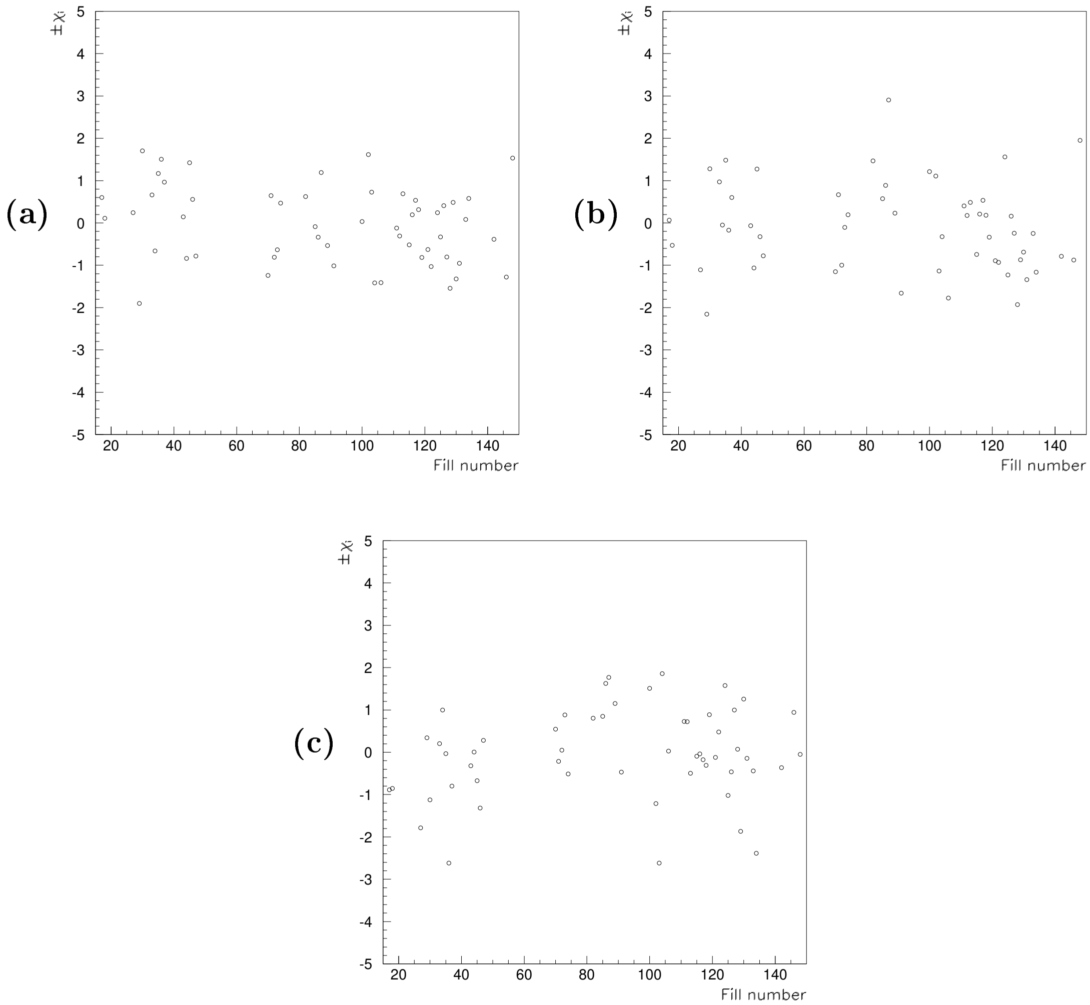

Figure 7.4: The weighted differences from the mean asymmetry for the (a) $h^+ - h^-$, (b) h^+ and (c) h^- asymmetries plotted against fill number.

7.5 False Asymmetries

A study has been made to identify non-statistical yield fluctuations in the data by randomising the target spin bits assigned in the data. A random spin bit was applied to each run in the data and then a normal asymmetry analysis was performed, with the measured asymmetry averaged over all x bins. This procedure was repeated 3000 times, each time with a different set of random spin bits. For each particle type, the resulting 3000 asymmetries were plotted as a histogram. Provided the spin bits are truly random, the resulting distribution should be a gaussian centred at zero. In addition, the width of the distribution should be the same as the statistical error of the asymmetry.

The results are shown in figure 7.5 and summarised in table 7.1. For each particle type, the widths of the gaussians are slightly larger than the statistical errors of the asymmetries. This indicates yield fluctuations in the data due to unidentified systematic problems with the experiment. The last column of table 7.1 shows the relative size of the yield fluctuations compared to the statistical error. A similar result was found for the inclusive positron asymmetry, with the size of the fluctuations found to be 46 % of the statistical error [54]. An investigation into the cause of the fluctuations has been made [53, 54]. No single component of the detector was found to be the source of the fluctuations; instead it is thought that the general, combined instabilities of each of the detector components in the first year of running was to blame. No yield fluctuations have been found for the 1996 spin asymmetries [64].

Asymmetry type	True asymmetry value	Width of random asymmetry distribution	Size of yield fluctuation (% σ_{Stat})
h^+	-.0343 ± .0145	.0156 ± 0.0002	40 %
h^-	-.0090 ± .0183	.0191 ± 0.0002	32 %

Table 7.1: Summary of the randomised spin bit study. The last column shows the size of the effect relative to the statistical error $((\sigma^2_{False} - \sigma^2_{Stat})^{\frac{1}{2}}/\sigma_{Stat}$, where σ_{False} is the width of the randomised asymmetry distribution and σ_{Stat} is the statistical error of the asymmetry).

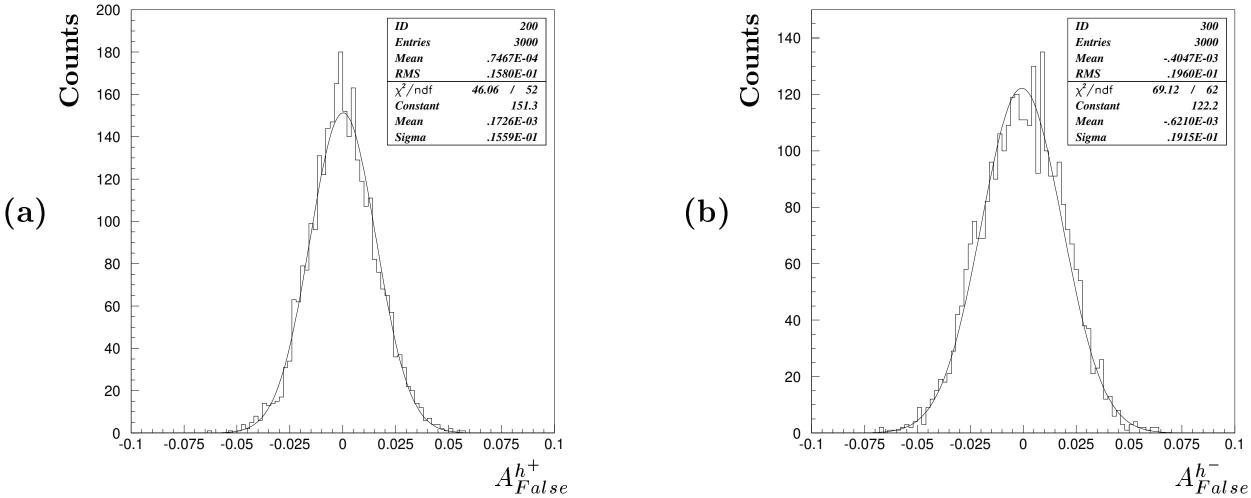

Figure 7.5: The resulting asymmetries for random target spin bits applied to each run of the data 3000 times, for the (a) h^+ and (b) h^- asymmetries. A gaussian fit was made to each distribution.

Chapter 8

Extraction of the Polarised Quark Distributions

8.1 The Charge Difference Pion Extraction

8.1.1 Description of the Method

The charge difference pion asymmetries can be used to extract the Δu and Δd valence distributions, as described in section 2.3.3. Using equation 2.32 and the equivalent for a ^{3}He target,

$$A_{^3He}^{\pi^+-\pi^-}(x) = \frac{-\Delta u_v(x) + 4\Delta d_v(x)}{7u_v(x) + 2d_v(x)}, \tag{8.1}$$

one obtains expressions for $\Delta u_v(x)$ and $\Delta d_v(x)$,

$$\Delta u_v(x) = \frac{1}{15}[4(4u_v - d_v)A_\pi^p + (7u_v + 2d_v)A_\pi^{^3He}] \tag{8.2}$$

$$\Delta d_v(x) = \frac{1}{15}[(4u_v - d_v)A_\pi^p + 4(7u_v + 2d_v)A_\pi^{^3He}]. \tag{8.3}$$

As described in chapter 4, this method requires a correction for the fragmentation process. The magnitude of this correction is estimated below. In addition, a small correction is required as the theory assumes that the ^{3}He target is “ideal” (see section 4.3), and a correction must be made for the polarisation of the protons within the target atoms.

8.1.2 Results

Due to the relatively low identified pion yields, particularly for the 1995 data, and the fact that the difference in two count rates has to be taken, the statistical uncertainties arising from using the charge difference method are large.

It is possible to use hadron asymmetries instead of identified pion asymmetries in order to improve the statistical uncertainty of this method. However, this would require an additional MC correction due to the fact that within the hadron sample, though the majority of particles are pions, there also exists significant contamination from other types of hadrons, primarily kaons and protons, which is not taken into account by the theory.

Both pion and hadron results are shown in figure 8.1. For this analysis, the unpolarised quark distributions were taken from [55].

(a)

(b)

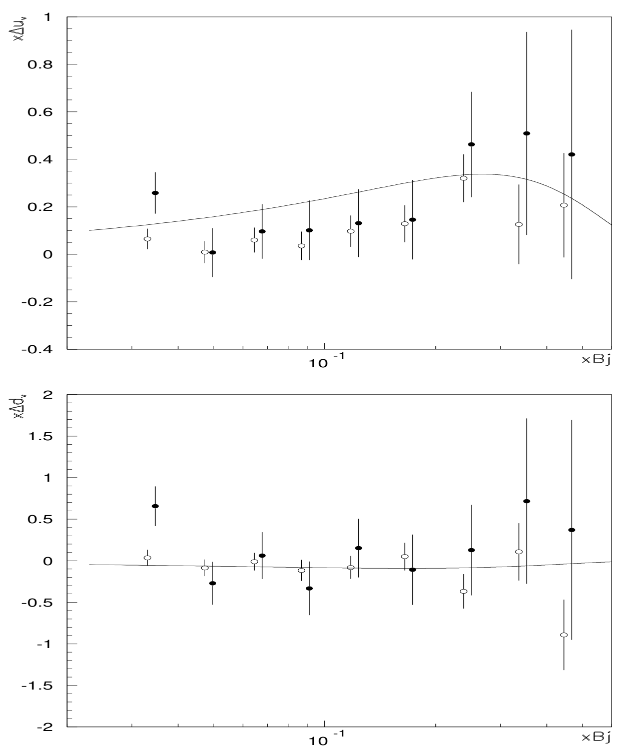

Figure 8.1: (a) the $x\Delta u$ and (b) the $x\Delta d$ valence distributions extracted using the charge difference pion asymmetry method (closed circles). Instead of using a pure pion sample, the result of the extraction method using the whole hadron sample is also shown (open cirles). For comparison, the line shows the parameterisation of GRVOG.

Consistency Check

To demonstrate the consistency of the method, the analysis was carried out on a MC data sample. The results are shown in figure 8.2. As can be seen, the extracted polarised distributions do not match the input polarised distributions. This difference is due to the fragmentation process.

(a)

(b)

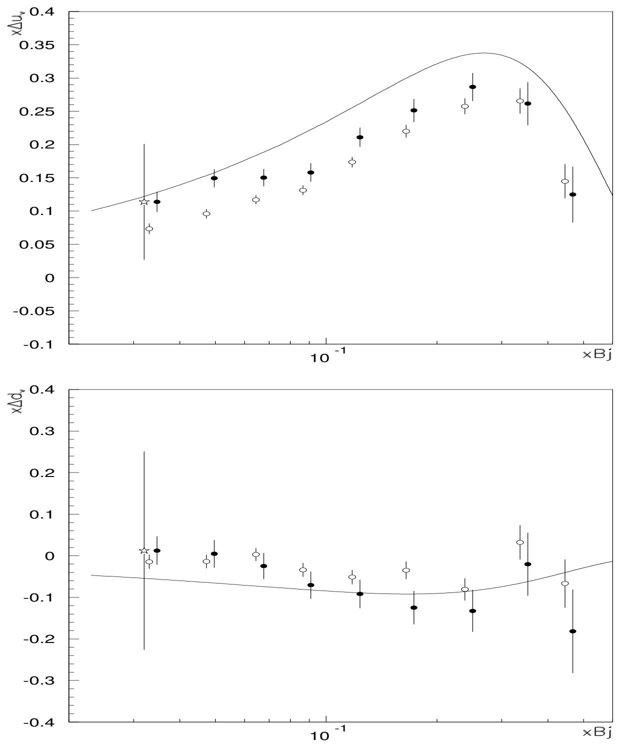

Figure 8.2: Extraction from MC data of (a) the $x\Delta u$ and (b) the $x\Delta d$ valence distributions using the charge difference pion asymmetry method (closed circles). The lines drawn show the GRVOG parameterisation which is the input to the MC. As can be seen, the original input parameterisations cannot be recovered. To compare the size of this effect with the statistical uncertainty of the experimental data, the extraction from experimental data using charge difference pions is shown for the first bin in x (asterisks) (note that the values of these two points have been shifted – only the error bars should be considered). The method is also shown using the hadron sample rather than the pion sample. Here the discrepancy between the extracted and input parameterisations is bigger due to additional contamination of the hadron sample with kaons and protons not accounted for in the charge difference extraction theory.

8.1.3 Conclusions

It has been shown that the charge difference method of extraction requires a MC correction for the fragmentation process. This is a complicated correction to make as it is dependent on the size of the asymmetry and hence on the size of the polarised quark distributions themselves. In addition the method results in large statistical uncertainties and no sensitivity to the sea polarisation. Instead of pursuing this method further therefore, an alternative method is used.

8.2 The Monte Carlo Fit Method of Extraction

The MC fit method uses both the semi-inclusive hadron asymmetries and the inclusive positron asymmetries for both ^{3}He and proton targets. A fit of the MC asymmetries to the experimental data asymmetries is performed, varying the polarised quark distributions which are the input to the MC. The method allows all the measured spin asymmetries to be used together, maximising the information used. In this fitting method, no explicit correction for the fragmentation process is required to be made to the asymmetries as the same hadron level quantities are being compared, namely the experimental and the MC asymmetries.

8.2.1 Description of the Method

The following assumptions, common to those made in the GRVOG parameterisation, were made. The fitted polarised distributions were constrained by the positivity requirement of the unpolarised quark distributions,

$$|\Delta q_k(x)| \leq q_k(x), \tag{8.4}$$

where k are the active quark flavours, $k = u, d, s, \overline{u}, \overline{d}, \overline{s}$. Additionally it was assumed that SU(3) flavour symmetry holds, such that

$$\Delta\overline{u}(x) = \Delta\overline{d}(x) = \Delta\overline{s}(x) = \Delta s(x) \equiv \Delta\overline{q}(x). \tag{8.5}$$

This leaves three polarised distributions to be fitted, Δu,Δd and $\Delta\overline{q}$. Rather than fitting the parameters from scratch, the starting point of the fit was taken to be the GRVOG parameterisation and corrections factors to this parameterisation, $c_u(x), c_d(x), c_{\overline{q}}(x)$ were varied,

$$\Delta u_{FIT}(x) = c_u(x) \cdot \Delta u_{GRVOG}(x) \tag{8.6}$$

$$\Delta d_{FIT}(x) = c_d(x) \cdot \Delta d_{GRVOG}(x) \tag{8.7}$$

$$\Delta \overline{q}_{FIT}(x) = c_{\overline{q}}(x) \cdot \Delta \overline{q}_{GRVOG}(x). \tag{8.8}$$

Six asymmetries measured in the experimental data were used to constrain the fit, the semi-inclusive positive and negative hadron asymmetries and the inclusive positron asymmetries from the data for ^{3}He and proton targets. Each bin in x was fitted independently using a χ^2 minimisation routine.

The fitting procedure is summarised in figure 8.3. Each iteration of the fit consisted of running the event generator MC with a trial set of polarised quark distributions and then calculating the total χ^2 differences between data and MC in each x bin,

$$\chi^2(x) = \sum_j \frac{(A^j_{MC}(x) - A^j_{DATA}(x))^2}{\sigma^{j2}_{MC}(x) + \sigma^{j2}_{DATA}(x)}, \tag{8.9}$$

where the index j represents the six asymmetries which were fitted, i.e.

$$A^j = A^{h^+}_{^3He}, A^{h^-}_{^3He}, A^{e^+}_{^3He}, A^{h^+}_p, A^{h^-}_p, A^{e^+}_p.$$

$\sigma^j(x)$ are the associated statistical errors on the asymmetries. The fitting algorithm would then choose a different set of trial parameters, $c_u(x), c_d(x), c_{\overline{q}}(x)$, which gave rise to a new set of polarised quark distributions used as input to the MC. The event generator would then be run again. This whole procedure was iterated until a χ^2 minimum for each x bin was found.

8.2.2 Configuration of the MC

The PEPSI event generator was used with the same configuration to that described in section 4.1.2. As well as a proton target, a “real” ^{3}He target was simulated (see section 4.3).

For each fit iteration, 2M events were generated in each spin state and for each target. Using a Pentium-Pro 200 PC, the event generation rate is about 17k

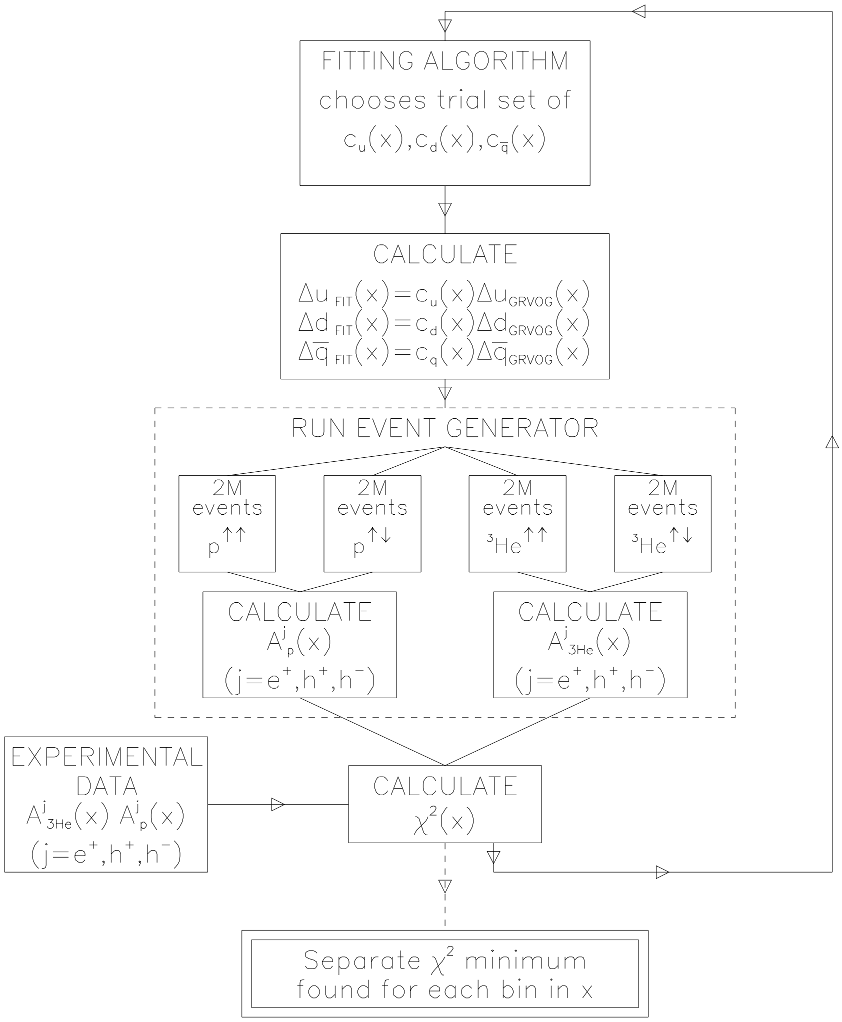

Figure 8.3: Schematic of the MC fitting procedure used to extract the polarised quark distributions.

events per minute. A large amount of cpu time was therefore required for each iteration of the fit, and thus an efficient fitting algorithm was chosen [65]. To minimise cpu time further, the results of each iteration were stored as a database for use in the error determination, as is described below.

8.2.3 Fit Results

The improvement in the agreement between data and MC before and after fitting can be seen by considering the error weighted differences between MC and data for each asymmetry, defined as

$$\chi^j(x) = \frac{A^j_{MC}(x) - A^j_{DATA}(x)}{(\sigma^{j2}_{MC}(x) + \sigma^{j2}_{DATA}(x))^{\frac{1}{2}}}.$$

These are shown for a MC produced with the GRVOG parameterisation and with the fitted parameterisation in figure 8.4. As can be seen, the fit has reduced $\chi^j(x)$ for nearly all the bins. The overall improvement of the χ^2 values (as defined in equation 8.9) is shown in figure 8.5.

8.2.4 Statistical Error Evaluation

Assumption of Uncorrelated Variables

The statistical errors on the fitted polarised distributions were first estimated assuming that the fitted parameters are uncorrelated.

Each of the correction factors $c_u(x), c_d(x), c_{\overline{q}}(x)$ were considered in turn. For each bin in x, with the other two correction factors fixed at their best fit values, the correction factor under consideration was varied from slightly below its minimum χ^2 point to slightly above in 6 equal steps. The MC was run after each step. A parabola was fitted to the resulting χ^2 values. From this parabola, the statistical error on the correction factor was taken to be its value at $\chi^2_{min} + 1$, where χ^2_{min} is the minimum of the parabola. This was then propagated to the error on the polarised distributions. As an example, the scan for $c_u(x)$ is shown in figure 8.6.

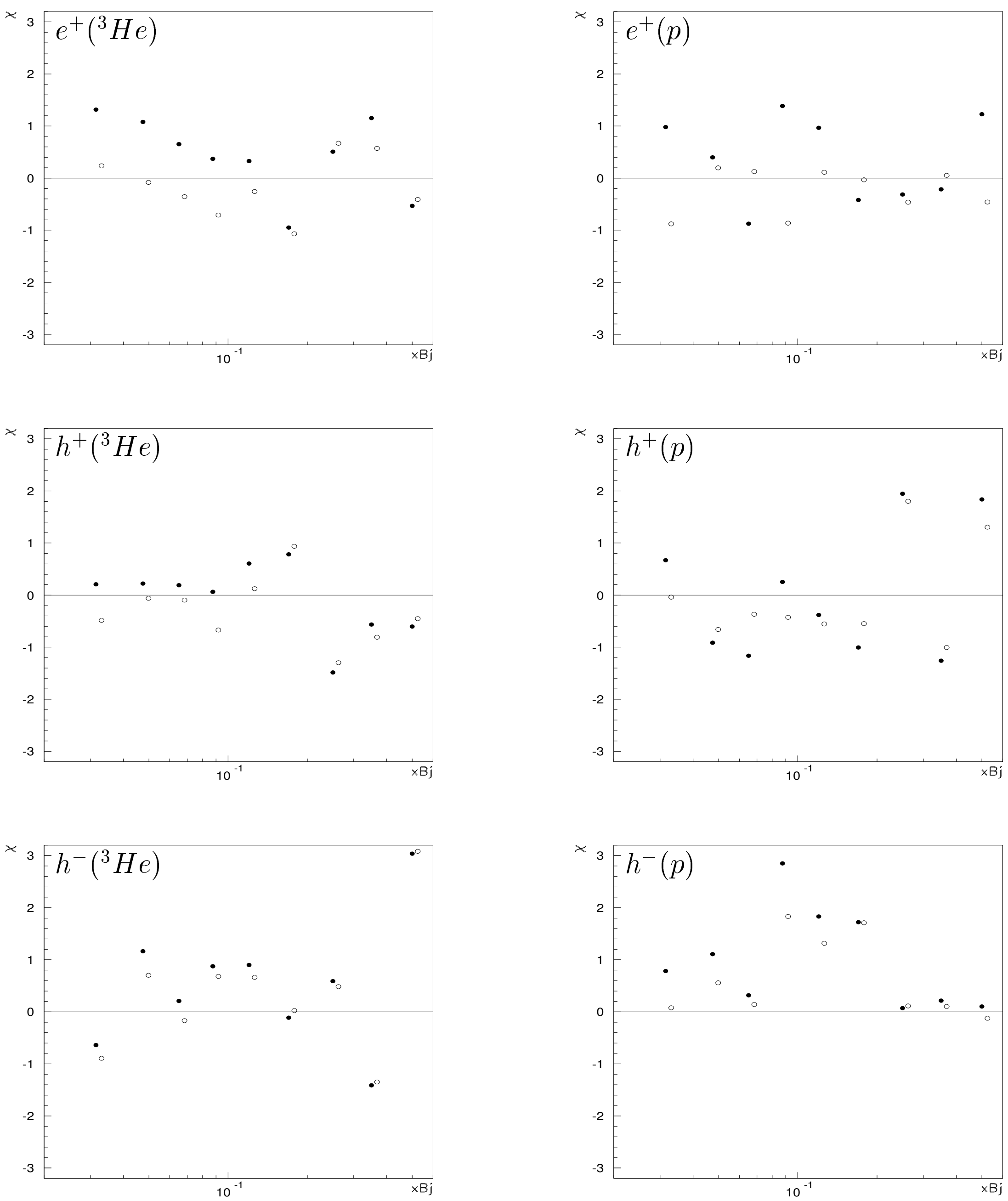

Figure 8.4: The error weighted differences between MC and data, $\chi(x)$, for each asymmetry used in the fit. This is shown for a MC produced using the GRVOG parameterisation (closed circles) and using the distributions obtained from the fit (open circles).

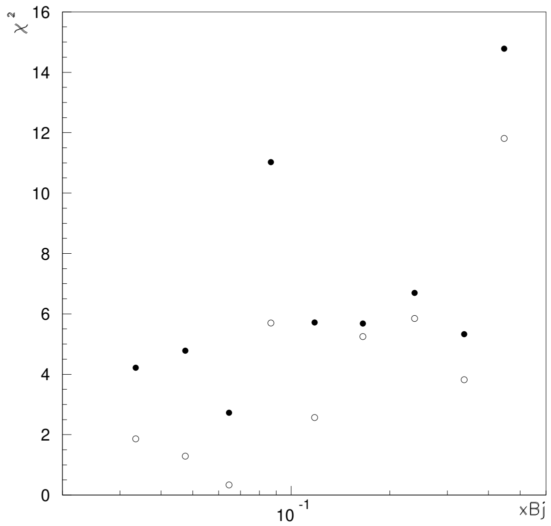

Figure 8.5: The χ^2 difference between MC and data summed for all fitted asymmetries. This is shown for a MC produced using polarised quark distributions from the GRVOG parameterisation (closed circles) and using the distributions obtained from the fit (open circles). After fitting the total χ^2 value summed over all x bins is 38 for the six degrees of freedom.

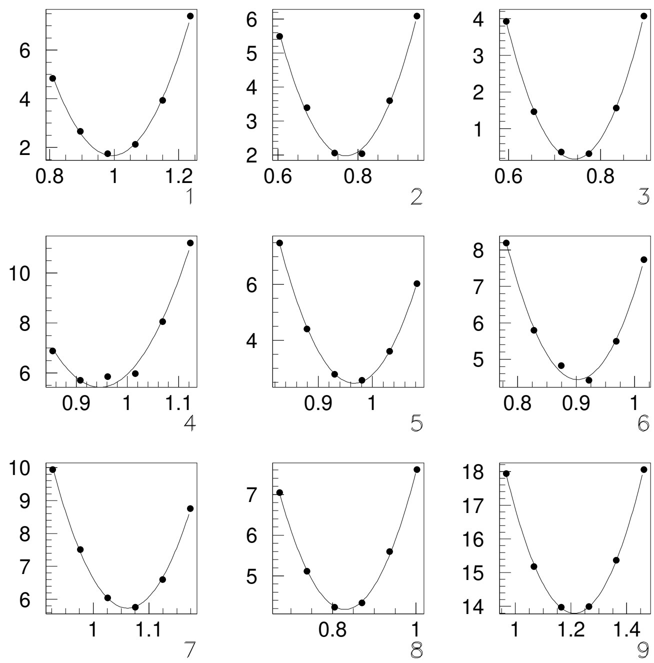

Figure 8.6: The scan of $c_u(x)$. Each plot represents a bin in x. The horizontal axis of each plot is the value of c_u, and the vertical axis is the resulting value of χ^2, with $c_d(x)$ and $c_{\overline{q}}(x)$ at their best fit values. The error was taken to be the value of $c_u(x)$ at $\chi^2_m in + 1$.

Accounting for Correlated Variables

To take into account the correlation between the fitted parameters, the error ellipsoid was calculated. The χ^2 ellipsoid equation was solved separately for each bin in x by minimising S where,

$$\begin{aligned} S = \sum_{i=1}^{n}[(a_{11}\Delta d_i^2 + a_{22}\Delta u_i^2 + a_{33}\Delta \overline{q}_i^2 \quad &+ \\ +a_{12}\Delta d_i \Delta u_i + a_{13}\Delta d_i \Delta \overline{q}_i + a_{23}\Delta u_i \Delta \overline{q}_i \quad &+ \\ +a_1 \Delta d_i + a_2 \Delta u_i + a_3 \Delta \overline{q}_i) \quad &- \quad (\chi_i^2 - \chi_{min}^2)]^2 \end{aligned} \tag{8.10}$$

where i runs over the n data points, $(\Delta u_i \Delta d_i, \Delta \overline{q}_i, \chi_i^2)$ which were taken from the data base of MC iterations calculated when the original fit was performed ($n \approx 80$). In the fit of this ellipsoid the free parameters of the ellipse, $a_{11}, ..., a_{33}$, were determined as well as a new value for χ_{min}^2. The results of this fit are shown in appendix B. The correlated errors were then determined by evaluating the parameters at $\chi_{min}^2 + 1$. New best fit values for Δu,Δd and $\Delta \overline{q}$ were taken for the new χ_{min}^2 found. These new minima differed only slightly from the original fit values, but are more stable as the whole distribution of points has been used in determining the minimum value.

The results obtained using both the uncorrelated and correlated error calculations are shown in figure 8.7. Significant correlation exists between the fitted parameters, as is evidenced by the the large increase in the size of the error bars when the correlated errors are calculated compared to the uncorrelated errors.

8.3 Comparison of Extraction Methods

The Δu and Δd valence distributions were calculated for the fit method, using the fitted $\Delta \overline{q}$ values, and are compared with the results from the charge difference pion analysis in figure 8.8. For the Δu results, which have the lowest statistical uncertainties, the low x bins of the charge difference results are systematically lower than the results from the fit. As was shown in section 8.1.2, the charge difference MC result for Δu requires a positive correction to it in order to recover the correct Δu MC input distribution. The positive difference between the fit results and the charge difference results can therefore be qualitatively understood in terms of this correction.

(a)

(b)

(c)

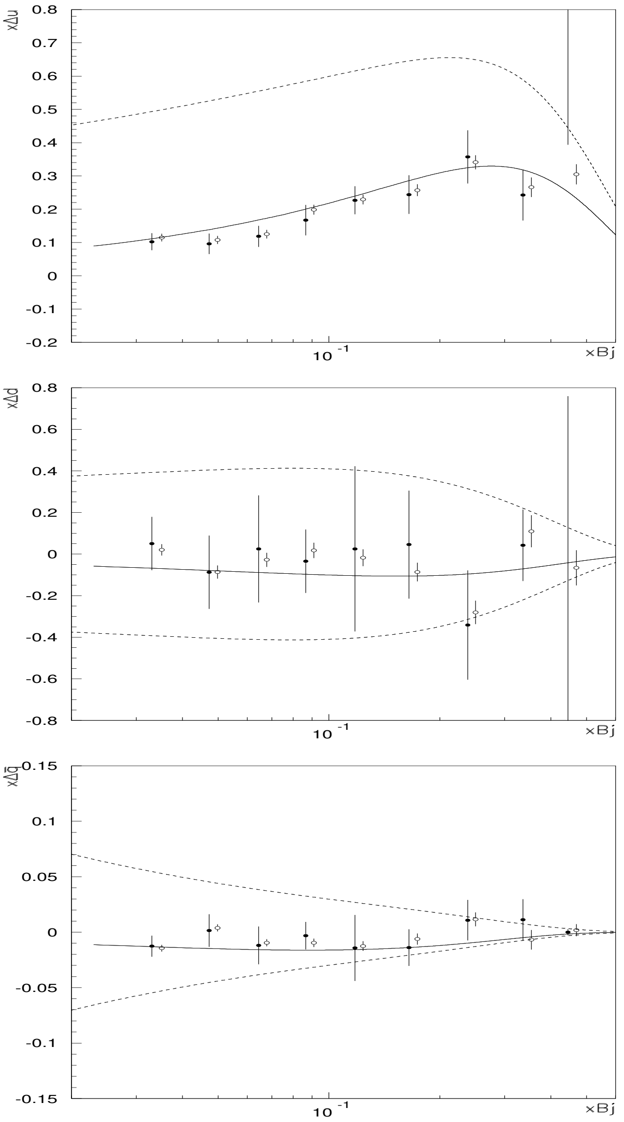

Figure 8.7: The fitted polarised distributions, (a) $x\Delta u(x)$ (b) $x\Delta d(x)$ (c) $x\Delta\overline{q}(x)$. The results are shown with the parameters assumed to be uncorrelated (open circles) and correlated (closed circles). The best fit values of the latter were taken from the fit of the χ^2 ellipsoid and thus are slightly different from the best fit values found by the fitting routine (shown for the open circles). The dotted lines show the maximum physically allowed boundary due to the positivity requirement for the quark distributions (equation 8.4). The solid line shows the GRVOG parameterisation.

(a)

(b)

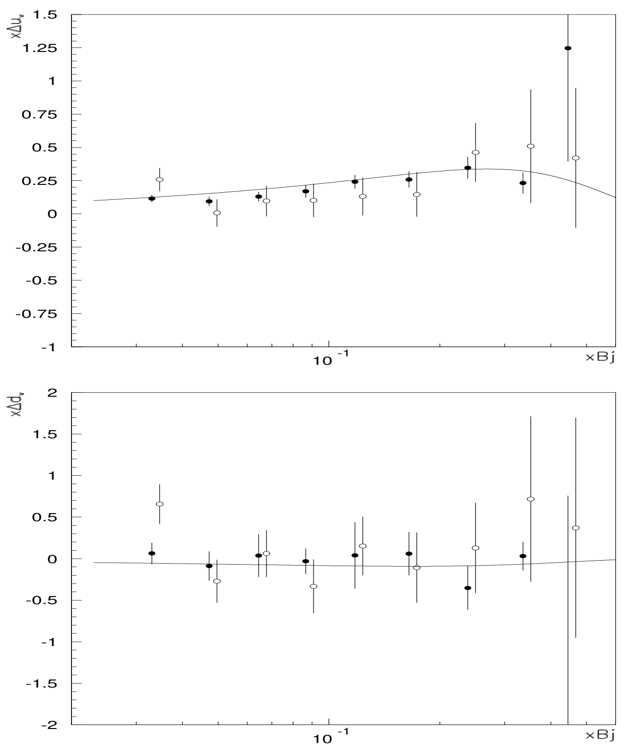

Figure 8.8: (a) the $x\Delta u$ and (b) the $x\Delta d$ valence distributions extracted using the charge difference pion asymmetry method (open circles) and from the fit method (closed circles). For comparison, the line shows the parameterisation of GRVOG.

8.4 Systematic Error Evaluation

The possible sources of systematic uncertainty can be divided into two main areas, systematic uncertainty associated with the measured asymmetries and systematic uncertainty associated with the MC fitting procedure.

8.4.1 Uncertainty in the Measurement of the Asymmetries

Uncertainty in the Beam and Target Polarisations

The effect of uncertainty in the target and beam polarisations is an offset to the normalisation of each asymmetry. The systematic uncertainty for the beam polarimeter measurement has been determined to be 5.4% for 1995 and 5% for 1996. The systematic uncertainty for the target polarisation measurement for 1995 has been determined to be 5%. The systematic error for the 1996 target polarisation is still being studied (see section 3.2.2). For this analysis, a conservative estimate of 10% uncertainty has been used.

Yield Fluctuations

To account for the yield fluctuations described in section 7.5, a systematic error equal to the size of the calculated false asymmetry was added for each of the 1995 asymmetries, namely 46%, 40% and 32% of the statistical errors for the inclusive, h^+ and h^- asymmetries respectively.

Uncertainty due to Radiative Corrections

The event generator simulation uses only the single photon exchange approximation (the Born approximation) and all higher order QED contributions, which exist in the measured asymmetries, are neglected. These radiative corrections have been calculated for the asymmetries by the POLRAD program [66]. The corrections are small, and therefore rather than correcting the actual asymmetries, they have been added as a systematic error.

Propagation of Error to Final Result

The separate contributions to the uncertainty in the measured asymmetries are shown in tables 8.1 – 8.6. The dominant error for the 1995 asymmetries is due to the yield fluctuations and for 1996 the target polarisation uncertainty.

An estimate was made of the effect of these uncertainties on the extracted values of the polarised quark distributions. Each contribution was added together in quadrature and, for each bin in x, the result added to the value of the asymmetry. This was done for each asymmetry. The complete fitting procedure was then performed using these modified asymmetries and a new set of polarised quark distributions was determined. Half the difference between the results from this fit and from the normal fit was taken as an estimate of the systematic error.

The results are summarised in tables 8.7 – 8.9. The fit procedure itself is subject to statistical fluctuations, and hence the estimate of the systematic error is also subject to statistical fluctuations. However, as a first approximation, it can be seen that the systematic error is much smaller than the statistical error for each of the distributions.

8.4.2 Uncertainty in the MC Fitting Procedure

Possible sources of systematic error due to the MC fitting procedure are

- Dependence of result on fragmentation model used.
- Dependence of result on unpolarised quark distributions used as input to the MC.
- Dependence of result on detector effects not modelled by event generator MC (such as precise acceptance modelling and detector smearing of asymmetry measurements)

The unpolarised quark distributions have been relatively well measured compared to the polarised quark distributions and therefore contribute a very small uncertainty to the final result. The acceptance and smearing corrections have been studied and found to be negligible for the inclusive asymmetry [53]. The largest uncertainty is therefore expected to come from the fragmentation model dependence, and this uncertainty is dealt with here.

To get an estimate of the fragmentation model dependence, it would be preferable to run the fit with a different fragmentation model to the Lund string model. Unfortunately however, additional models have not yet been implemented in the software. Instead, as a first estimate of the model dependency, the whole fitting procedure was carried out with the Lund model using the default fragmentation parameters rather than the tuned fragmentation parameters (see section 4.2). The results are a worst case scenario, as the MC is known not to describe the experimental data well with the default fragmentation parameters. Half the difference between the two fit results was taken as an estimate of the fragmentation model dependent error.

The results are summarised in tables 8.7 – 8.9. Again, the results of the fit itself are subject to statistical fluctuations and hence the estimate of the model

x bin	$\delta(p_B)_{syst}$	$\delta(p_T)_{syst}$	$\delta(Yields)$	$\delta(RC)$	$\delta(total)_{syst}$
1	0.001802	0.001675	0.006167	0.000079	0.006640
2	0.000593	0.000551	0.006677	0.000074	0.006726
3	0.001731	0.001609	0.007151	0.000075	0.007532
4	0.001679	0.001560	0.008314	0.000080	0.008624
5	0.002211	0.002055	0.008973	0.000082	0.009468
6	0.002544	0.002364	0.010822	0.000094	0.011366
7	0.001099	0.001021	0.013812	0.000120	0.013893
8	0.002933	0.002726	0.023760	0.000207	0.024096
9	0.003131	0.002911	0.034046	0.000289	0.034315

Table 8.1: The systematic error contributions to the 1995 inclusive asymmetry measurement.

x bin	$\delta(p_B)_{syst}$	$\delta(p_T)_{syst}$	$\delta(Yields)$	$\delta(RC)$	$\delta(total)_{syst}$
1	0.002661	0.002473	0.012811	0.000080	0.013316
2	0.001249	0.001161	0.013108	0.000102	0.013219
3	0.001780	0.001655	0.013635	0.000150	0.013851
4	0.002362	0.002195	0.015517	0.000171	0.015849
5	0.002090	0.001942	0.016432	0.000160	0.016679
6	0.000020	0.000019	0.019782	0.000129	0.019783
7	0.008077	0.007507	0.026780	0.000100	0.028961
8	0.004406	0.004095	0.055462	0.000055	0.055788
9	0.010694	0.009940	0.108760	0.000027	0.109735

Table 8.2: The systematic error contributions to the 1995 h^+ asymmetry measurement.

x bin	$\delta(p_B)_{syst}$	$\delta(p_T)_{syst}$	$\delta(Yields)$	$\delta(RC)$	$\delta(total)_{syst}$
1	0.004250	0.003950	0.011644	0.000451	0.013017
2	0.001172	0.001089	0.012242	0.000490	0.012356
3	0.001812	0.001684	0.012974	0.000532	0.013218
4	0.000511	0.000475	0.015071	0.000579	0.015098
5	0.000134	0.000124	0.016464	0.000659	0.016479
6	0.000686	0.000638	0.020407	0.000810	0.020444
7	0.003234	0.003006	0.028669	0.000971	0.029023
8	0.013296	0.012358	0.061836	0.001057	0.064454
9	0.067901	0.063111	0.125475	0.001214	0.156010

Table 8.3: The systematic error contributions to the 1995 h^- asymmetry measurement.

x bin	$\delta(p_B)_{syst}$	$\delta(p_T)_{syst}$	$\delta(RC)$	$\delta(total)_{syst}$
1	0.004450	0.008495	0.002120	0.009822
2	0.005024	0.009591	0.000500	0.010839
3	0.005379	0.010270	0.000250	0.011596
4	0.009242	0.017644	0.000690	0.019930
5	0.011247	0.021471	0.001100	0.024263
6	0.012756	0.024353	0.001750	0.027548
7	0.017109	0.032663	0.002040	0.036929
8	0.020732	0.039580	0.001840	0.044719
9	0.028060	0.053568	0.000760	0.060477

Table 8.4: The systematic error contributions to the 1996 inclusive asymmetry measurement.

x bin	$\delta(p_B)_{syst}$	$\delta(p_T)_{syst}$	$\delta(RC)$	$\delta(total)_{syst}$
1	0.006344	0.012112	0.001598	0.013766
2	0.004700	0.008973	0.000343	0.010136
3	0.005803	0.011078	0.000251	0.012508
4	0.010456	0.019962	0.000648	0.022544
5	0.012389	0.023651	0.000988	0.026718
6	0.013430	0.025639	0.001390	0.028977
7	0.026354	0.050313	0.001670	0.056822
8	0.014513	0.027706	0.001440	0.031310
9	0.046467	0.088710	0.000087	0.100143

Table 8.5: The systematic error contributions to the 1996 h^+ asymmetry measurement.

x bin	$\delta(p_B)_{syst}$	$\delta(p_T)_{syst}$	$\delta(RC)$	$\delta(total)_{syst}$
1	0.003887	0.007421	0.001400	0.008494
2	0.004479	0.008551	0.001642	0.009791
3	0.003825	0.007302	0.001794	0.008436
4	0.012432	0.023735	0.001901	0.026861
5	0.012397	0.023668	0.002019	0.026794
6	0.015976	0.030500	0.002200	0.034501
7	0.013785	0.026317	0.002362	0.029802
8	0.019750	0.037705	0.002265	0.042625
9	0.025064	0.047850	0.001385	0.054035

Table 8.6: The systematic error contributions to the 1996 h^- asymmetry measurement.

dependency is also subject to fluctuations. However, it can be seen that the error is small compared to the statistical error.

The contributions from the systematic error from the asymmetry measurement and from the model dependency were added in quadrature to give the total systematic error. This is shown in the summary tables 8.7 – 8.9.

8.4.3 The Final Result

The final polarised quark distributions are shown in figure 8.9 and are seen to be consistent with the GRVOG parameterisation (with χ^2 of 8.2 for Δu, 3.5 for Δd and 4.8 for $\Delta \overline{q}$ for nine degrees of freedom).

The results agree well with the SMC results, compared in figure 8.10.

The systematic error shown is expected to decrease in the future. This is because for the 1995 data set the dominant systematic uncertainty is due to yield fluctuations. This effect is not evident in the 1996 data set and was due to detector instabilities during the first year of running. In 1996 the uncertainty is dominated by the uncertainty in the target polarisation. With studies ongoing, it is expected that this uncertainty will be reduced in the future. The fragmentation model uncertainty will be better estimated in the future with the use of additional fragmentation models and event generators.

The uncertainty in the results is dominated by the statistical uncertainty. Scattering takes place predominantly off u quarks. A proton target therefore predominantly gives information on u quark distributions, whereas a neutron target, by isospin symmetry, gives information on d quark distributions. The large statistical uncertainty in the Δd distribution is a result of the relatively small amount of neutron data so far taken. This will improve when more neutron data is taken using a deuterium target, planned to start running in 1998, which will additionally have a similarly high polarisation to the proton target. The statistical uncertainty of the Δu distribution will also improve when the proton data taken in 1997 is analysed. Approximately 50% more data was taken during the long running period of 1997 compared to 1996.

The sensitivity to the sea quark polarisation could be greatly increased by

x bin	$x\Delta u$	$\delta(\Delta u)$ (Statistical)	$\delta(\Delta u)_{syst1}$ (Meas.)	$\delta(\Delta u)_{syst2}$ (Frag. Model)	$\delta(\Delta u)_{syst(1\oplus 2)}$ (Total)
1	0.10236	0.02557	0.00584	0.00829	0.01014
2	0.09611	0.03074	0.00083	0.00627	0.00632
3	0.11856	0.03180	0.00252	0.00201	0.00323
4	0.16729	0.04583	0.00293	0.00500	0.00579
5	0.22690	0.04228	0.00620	0.00050	0.00622
6	0.24400	0.05819	0.00617	0.01259	0.01402
7	0.35740	0.07999	0.00477	0.00697	0.00845
8	0.24265	0.07632	0.00512	0.01475	0.01561
9	1.24602	0.85250	0.01087	0.02591	0.02810

Table 8.7: The results for the Δu measurement. The systematic error is broken down into its two components, the error on the asymmetry measurement and the fragmentation model dependent error.

x bin	$x\Delta d$	$\delta(\Delta d)$ (Statistical)	$\delta(\Delta d)_{syst1}$ (Meas.)	$\delta(\Delta d)_{syst2}$ (Frag. Model)	$\delta(\Delta d)_{syst(1\oplus 2)}$ (Total)
1	0.05042	0.12823	0.00032	0.00122	0.00126
2	-0.08698	0.17633	0.00592	0.00690	0.00909
3	0.02460	0.25735	0.02448	0.00001	0.02448
4	-0.03474	0.15262	0.01260	0.00426	0.01330
5	0.02498	0.39753	0.01293	0.04040	0.04242
6	0.04551	0.25969	0.00607	0.08474	0.08496
7	-0.34158	0.26289	0.04497	0.00965	0.04599
8	0.04233	0.17159	0.00125	0.02737	0.02740
9	-2.10000	2.85940	0.00144	0.00713	0.00727

Table 8.8: The results for the Δd measurement. The systematic error is broken down into its two components, the error on the asymmetry measurement and the fragmentation model dependent error.

x bin	$x\Delta\overline{q}$	$\delta(\Delta\overline{q})$ (Statistical)	$\delta(\Delta\overline{q})_{syst1}$ (Meas.)	$\delta(\Delta\overline{q})_{syst2}$ (Frag. Model)	$\delta(\Delta\overline{q})_{syst(1\oplus 2)}$ (Total)
1	-0.01257	0.00951	0.00022	0.00008	0.00023
2	0.00152	0.01468	0.00094	0.00008	0.00095
3	-0.01194	0.01701	0.00020	0.00020	0.00028
4	-0.00313	0.01237	0.00126	0.00047	0.00135
5	-0.01416	0.02974	0.00442	0.00428	0.00615
6	-0.01389	0.01647	0.00368	0.00534	0.00648
7	0.01080	0.01823	0.00122	0.00011	0.00123
8	0.01121	0.01848	0.00169	0.00105	0.00200
9	0.00182	0.00277	0.00087	0.00049	0.00100

Table 8.9: The results for the $\Delta\overline{q}$ measurement. The systematic error is broken down into its two components, the error on the asymmetry measurement and the fragmentation model dependent error.

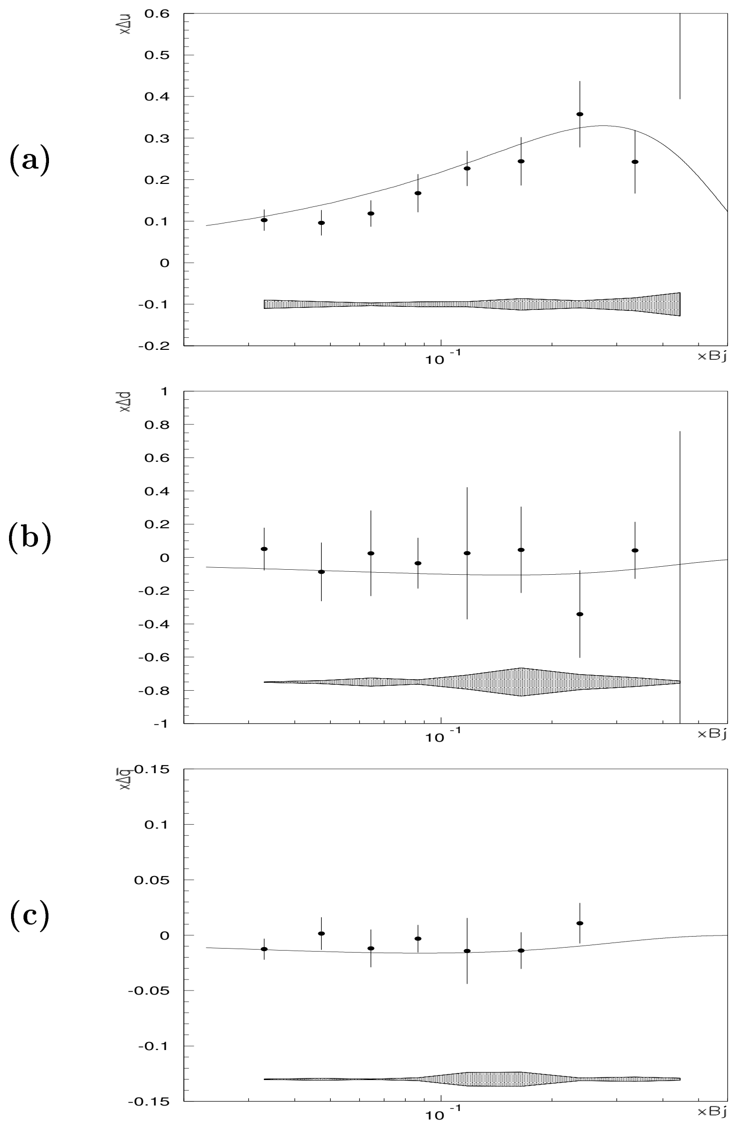

Figure 8.9: The extracted polarised quark distributions, (a) $x\Delta u(x)$ (b) $x\Delta d(x)$ (c) $x\Delta \overline{q}(x)$. The shaded band shows the estimated systematic uncertainty. The solid line shows the GRVOG parameterisation.

(a)

(b)

(c)

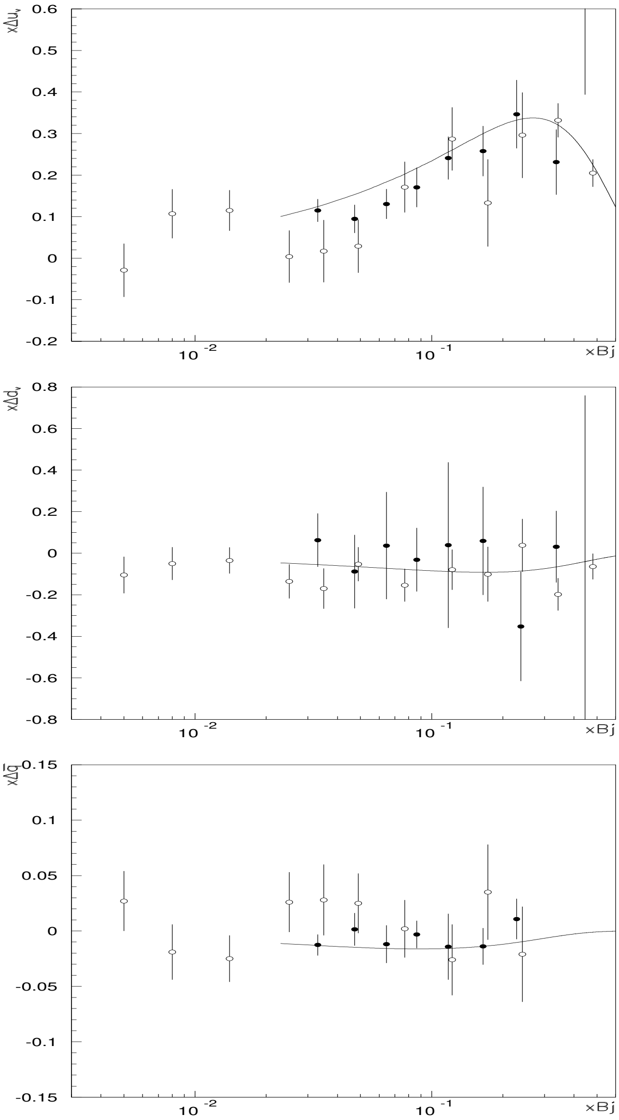

Figure 8.10: The extracted polarised quark distributions (closed circles), (a) $x\Delta u_v(x)$ (b) $x\Delta d_v(x)$ (c) $x\Delta\overline{q}(x)$, compared to the SMC results (open cirlces) [24]. The SMC results are for their complete data set. The solid line shows the GRVOG parameterisation evaluated for the HERMES Q^2 range.

introducing kaon asymmetries into the fit. With the current data, this has not been worthwhile as the Čerenkov momentum threshold for a clean kaon sample was 13.5 GeV for 1995 and 21.0 GeV for 1996 data, too high to produce significant yields. However in 1998 the Čerenkov detector is being upgraded to a Ring Imaging Čerenkov detector (RICH) [67] which will provide identification of pions and kaons over the complete momentum range.

Chapter 9

Conclusions

Data has been analysed from the first two years of HERMES data taking when both polarised ^{3}He and proton gas targets were operated. The semi-inclusive hadron and pion spin asymmetries have been extracted from the 1995 data set for a ^{3}He target. Systematic studies have been carried out on these asymmetries. By combining these results with the preliminary asymmetries for a proton target, and inclusive positron asymmetries for both targets, an extraction of the polarised quark distributions has been performed. This extraction method has made use of a Monte Carlo to connect the hadron level asymmetry measurements to the parton level quark distributions. Two different methods of extraction have been investigated, the charge difference pion method and the Monte Carlo fit method. While both methods gave results which were consistent with each other, the Monte Carlo fit method was chosen for the final result because it gives lower statistical and systematic uncertainties and additionally has sensitivity to the sea quark polarisation.

Within the overlapping range in x, the extracted distributions agree well with the results from SMC, the only other experiment to have performed this measurement. This is an important cross check as SMC used a very different experimental technique, using solid polarised targets and a muon beam at 90 GeV and 200 GeV. Using data from only the first two years of running, these preliminary results demonstrate comparable statistical uncertainties to those for the complete SMC data set.

The uncertainty in the Δu distribution will be improved when the 1997 proton data is analysed, this data set will enlarge the total proton data set by about 150%. The Δd distribution has large statistical uncertainty due to the relatively small amount of neutron data available. This will be improved when the deuterium target starts operating in 1998. The introduction of a RICH detector from 1998, and hence the identification of hadrons over the complete momentum range, will not only provide improved identified pion yields, but also a clean kaon sample. These kaons can provide an accurate direct measurement of the sea quark polarisation which is both theoretically and experimentally loosely constrained.

In conclusion, a method for extracting the polarised quark distributions from semi-inclusive spin asymmetries has been described. All three polarised quark distributions are consistent with the GRVOG parameterisation, derived using inclusive data and the axial matrix elements F and D, though with only the first two years of HERMES data analysed, the results are severely limited by statistical uncertainty.

Appendix A

Error Analysis for the Asymmetries

The nomenclature used in this section has been defined in section 6.1.

A.1 Charge Difference Asymmetry

The charge difference asymmetry can be written as

$$\begin{aligned} A^{N^{h^+}-N^{h^-}} &= \frac{N_-^{h^+}L_+ - N_-^{h^-}L_+ - N_+^{h^+}L_- + N_+^{h^-}L_-}{N_-^{h^+}D_+^{h^+}P_+L_+ - N_-^{h^-}D_+^{h^-}P_+L_+ + N_+^{h^+}D_-^{h^+}P_-L_- - N_+^{h^-}D_-^{h^-}P_-L_-} \\ &\equiv \frac{X}{Y} \end{aligned} \tag{A.1}$$

The statistical error on the asymmetry is then

$$\begin{aligned} (\delta A)^2 = (\delta N_-^{h^+}\frac{(YL_+ - XD_+^{h^+}P_+L_+)}{Y^2})^2 + (\delta N_-^{h^-}\frac{(-YL_+ + XD_+^{h^-}P_+L_+)}{Y^2})^2 \\ + (\delta N_+^{h^+}\frac{(-YL_- - XD_-^{h^+}P_-L_-)}{Y^2})^2 + (\delta N_+^{h^-}\frac{(YL_- + XD_-^{h^-}P_-L_-)}{Y^2})^2 \end{aligned} \tag{A.2}$$

where $\delta N_\pm^{h^\pm}$ is the statistical error on each count rate taken to be $\sqrt{N_\pm^{h^\pm}}$.

A.2 Single Particle Asymmetries

Taking the h^+ asymmetry as an example, one can write the asymmetry as

$$\begin{aligned} A^{N^{h^+}} &= \frac{N_-^{h^+} L_+ - N_+^{h^+} L_-}{N_-^{h^+} D_+^{h^+} P_+ L_+ + N_+^{h^+} D_-^{h^+} P_- L_-} \\ &\equiv \frac{X}{Y} \end{aligned} \tag{A.3}$$

The statistical error on the asymmetry is then

$$(\delta A)^2 = (\delta N_-^{h^+} \frac{(Y L_+ - X D_+^{h^+} P_+ L_+)}{Y^2})^2 + (\delta N_+^{h^+} \frac{(-Y L_- - X D_-^{h^+} P_- L_-)}{Y^2})^2 \tag{A.4}$$

where $\delta N_\pm^{h^+}$ is the statistical error on each count rate taken to be $\sqrt{N_\pm^{h^+}}$.

Appendix B

χ^2 ellipsoid fitting

To reduce the parameters used to describe the ellipsoid in equation 8.10 to six, the ellipsoid was shifted to the origin. This was done by shifting the Δq values by an amount equal to their original best fit values, namely Δu_{min}, Δd_{min} and $\Delta\overline{q}_{min}$. The ellipsoid equation then becomes

$$\begin{aligned}S = \sum_{i=1}^{n}[(a'_{11}(\Delta d_i - \Delta d_{min})^2 + a'_{22}(\Delta u_i - \Delta u_{min})^2 + a'_{33}(\Delta\overline{q}_i - \Delta\overline{q}_{min})^2 \quad + \\ a'_{12}(\Delta d_i - \Delta d_{min})(\Delta u_i - \Delta u_{min}) + a'_{13}(\Delta d_i - \Delta d_{min})(\Delta\overline{q}_i - \Delta\overline{q}_{min}) \quad + \\ a'_{23}(\Delta u_i - \Delta u_{min})(\Delta\overline{q}_i - \Delta\overline{q}_{min}) - (\chi_i^2 - \chi_{min}^2)]^2 \end{aligned} \tag{B.1}$$

The fitted parameters are shown in table B.1 for each x bin.

x bin	a'_{11}	a'_{22}	a'_{33}	a'_{12}	a'_{13}	a'_{23}
1	643.69	36802.	563090.	7675.6	34507.	276360.
2	187.70	4402.5	52865.	650.48	5201.2	22696.
3	111.62	7284.0	67109.	1263.6	4917.0	39704.
4	277.75	745.76	48727.	119.81	6554.4	4627.9
5	43.802	799.11	9017.2	131.29	1154.0	2624.3
6	101.94	334.18	26530.	53.959	3025.4	1520.4
7	14.861	161.66	3030.9	15.911	5.8562	119.00
8	35.980	183.08	2948.7	38.423	12.871	122.65
9	0.1419	1.6071	131470.	0.3550	8.8670	80.279

Table B.1: The six fitted χ^2 ellipsoid parameters of equation B.1 for each bin in x.

References

[1] J. Ashman *et al.*, Phys. Lett., **B206** (1988) 364 ; Nucl. Phys., **B333** (1990) 1.

[2] H.A.McL. Tallini, Proc. of Workshop on DIS off Polarised Targets, Zeuthen, **DESY 97-200** (1997) 41.

[3] J.D. Bjorken, Phys. Rev., **179** (1969) 1547.

[4] R.P. Feynman, Photon Hadron Interactions, W.A. Benjamin, New York (1972).

[5] W. Greiner, A. Schäfer, "Quantum Chromodynamics", Springer (1995).

[6] J.D. Bjorken, Phys. Rev., **148** (1966) 1467 ; Phys. Rev. **D1** (1970) 1376.

[7] J. Kodaira *et al.*, Phys. Rev., **D20** (1979) 627 ; Nucl. Phys., **B159** (1979) 99.

[8] J. Kodaira, Nucl. Phys., **B165** (1980) 129.

[9] J. Ellis and R.L. Jaffe, Phys. Rev., **D9** (1974) 1444 ; *ibid.* **D10** (1974) 1669.

[10] M.J. Algaurd *et al.*, Phys. Rev. Lett., **37** (1976) 1258 ; Phys. Rev. Lett., **37** (1976) 1261.

[11] G. Baum *et al.*, Phys. Rev. Lett., **51** (1983) 1135.

[12] D. Adams *et al.*, Phys. Lett., **B412** (1997) 414 ; Phys. Lett., **B396** (1997) 338 ; Phys. Lett., **B336** (1994) 125.

[13] D.L. Anthony *et al.*, Phys. Rev. Lett., **71** (1993) 959.

[14] K.Abe *et al.*, Phys. Rev. Lett., **74** (1995) 346 ; SLAC-PUB-95-6982 (1995).

[15] J. Ellis and M. Karliner, Phys. Lett., **B341** (1995) 397.

[16] M. Gourdin, Nucl. Phys., **B38** (1972) 418.

[17] J. Dai *et al.*, Phys. Rev., **D53** (1996) 273.

[18] M. Glück, E. Reya, W. Vogelsang, Phys.Lett., **B359** (1995) 201.

[19] T.Gehrmann, W.J. Stirling, Phys. Rev. **D53**, 6100-6109 (1996).

[20] M. Althoff *et al*, Z. Phys., **C22** (1984) 307.

[21] M. Arneodo *et al*, Z. Phys., **C36** (1987) 527.

[22] J.J. Aubert *et al*, Phys. Lett., **B160** (1985) 417.

[23] Frankfurt *et al.*, Phys. Lett., **B 230** (1989) 141.

[24] B. Adeva *et al.*, Phys. Lett., **B369** (1996) 93.

[25] A.A. Sokolov and I.M. Ternov, Sov. Phys. Dokl. 8 (1964) 1203.

[26] D.P. Barber *et al*, Phys. Lett., **B343** (1995) 436.

[27] D.P. Barber *et al*, Nucl. Instr. and Meth., **A329** (1993) 79.

[28] D.P. Barber *et al*, Nucl. Instr. and Meth., **A338** (1994) 166.

[29] K. Zapfe *et al*, Rev. Sci. Instr., **66(1)** (1995) 28.

[30] H. Wiedemann, "Particle Accelerator Physics", Springer Verlag (1993).

[31] J. Stewart, Seventh Int. Work. on Pol. Gas Targets and Pol. Beams, Univ. of Illinois at Urbana-Champaign, August 18–22 1997 (to be published).

[32] E. Kinney, Proc. of Work. on Pol. Ion Sources and Pol. Gas Targets, Madison (1993) ; AIP Conf. Proc. 293 (1994) 278.

[33] H. Kolster, Seventh Int. Work. on Pol. Gas Targets and Pol. Beams, Univ. of Illinois at Urbana-Champaign, August 18–22 1997 (to be published).

[34] D. DeSchepper *et al*, Submitted to Nucl. Instr. and Meth. (1998).

[35] D. DeSchepper, D.Phil. thesis (partial fulfillment), MIT (1997).

[36] F. Stock *et al*, Nucl. Instr. and Meth., **A343** (1994) 334.

[37] F. Stock *et al*, Int. Workshop on Pol. Beams and Pol. Gas Targets, Cologne (1996) 260.

[38] B. Braun, Doktorarbeit, Univ. Munich (1995).

[39] B. Braun, Seventh Int. Work. on Pol. Gas Targets and Pol. Beams, Univ. of Illinois at Urbana-Champaign, August 18–22 1997 (to be published).

[40] A. Brüll, private communication.

[41] K. Ackerstaff *et al*, to be submitted to Nucl. Instr. and Meth. (1998).

[42] K. Coulter *et al*, HERMES Technical Design Report, **DESY PRC90/01** (1990).

[43] K. Ackerstaff, Doktorarbeit, Univ. Hamburg (1996).

[44] W. Wander, Doktorarbeit, Friedrich-Alexander-Univ. Erlangen-Nurenberg (1996).

[45] M. Veltri, Doktorarbeit, Max-Planck institut für Kernphysik (MPIH-V18-1992).

[46] L. Mankiewicz, A. Schäfer, M. Veltri, Comp. Phys. Commun., **71** (1992) 305.

[47] The PEPSI homepage, http://th.physik.uni-frankfurt.de/ maul/pepsi.html.

[48] G. Ingelman, A. Edin, J. Rathsman, Comp. Phys. Comm., **101** (1997) 108.

[49] X. Artru, G. Mennessier, **70** (1974) 93 ; B. Andersson, G. Gustafson, G. Ingelman, T. Sjöstrand, **97** (1983) 31.

[50] T. Sjöstrand, Computer Physics Commun. **39** (1986) 347 ; T. Sjöstrand, M. Bengtsson Computer Physics Commun. **43** (1987) 367.

[51] The HMC homepage, http://dxnhd1.mpi-hd.mpg.de/ herprod/

[52] CERN Program Library Long Writeup W5013, CERN (1993).

[53] M. Ferstl, Doktorarbeit, Friedrich-Alexander-Univ. Erl.-Nuernbergs (1997).

[54] N. Akopov *et al*, `HERMES report 97-007`.

[55] M. Glück, E. Reya and A. Vogt, Z. Phys. **C67** (1995) 433.

[56] B.Andersson, G. Gustafson and B. Söderberg, Z. Phys. **C20** (1983) 317.

[57] P. Geiger, Doktorarbeit, Univ. Heidelberg (1998).

[58] J.L. Friar *et al.*, Phys. Rev. Lett. **C42** (1990) 193.

[59] EMC (Arneodo *et al.*), Z.Phys. C **31** (1986) 1.

[60] R. Kaiser, D.Phil. thesis (partial fulfillment), Simon Fraser Univ. (1997).

[61] F.Menden, Diploma thesis, TRIUMF (1997).

[62] H. Ihssen, private communication.

[63] K. Ackerstaff *et al*, Phys. Lett., **B404** (1997) 383.

[64] B. Bains *et al*, `HERMES report 97-048`.

[65] H. Ihssen, Diplomarbeit, Univ. Heidelberg (1990).

[66] I.V. Akushevich and N.M. Shumeiko, J. Phys. G:Nucl. Part. Phys., **20** (1994) 513.

[67] M. Amarian *et al.*, `HERMES (public) report 97-003`.